申 报	系列：教学科研型
	专业：机械工程
	职称：副教授

业绩成果材料

（申报人的业绩成果材料包括论文、科研项目、获奖以及其他成果等）

单　位（二级单位）___工程学院_______

姓　名___曹亚超_______

材料核对人：　　　　　　　　　　　　单位盖章：

核对时间：

华南农业大学制

目　录

一、教学研究业绩

1.教学研究项目：

二、科研项目

1.主持：

2.主参：

三、论文、著作等

2.以通讯作者发表本专业论文情况

四、科研成果

1.知识产权

五、其他业绩

1.指导学生学科竞赛

2.个人荣誉

一、教学研究业绩

关于公示2025年度校级本科教学质量与教学改革工程项目拟立项名单的通知

来源单位及审核人：　编辑：　审核发布：本科生院（招生办公室）　发布时间：2025-09-25

各学院、部处、各单位：

根据《关于开展2025年度校级本科教学质量与教学改革工程项目申报工作的通知》精神,经项目负责人申报、所在单位推荐和学校组织专家评审或本科生院审核等程序，拟立项“基于OBE理念的‘数字赋能、思政融合、产教协同’的《制药设备与工艺设计》课程育人模式研究与实践”等127个项目为2025年度校级本科教学改革项目；拟立项“农林院校‘智能建造’人才特色班”等52个项目为2025年度校级本科质量工程项目。现予以公示，具体名单见附件。

公示期自2025年9月25日至9月29日。如有异议，请在公示期内以书面方式提交至行政楼329房（附必要的证据材料，并署真实姓名），未署真实姓名或逾期者不予受理。

附件：1. 2025年度校级本科教学改革拟立项名单.xlsx
2. 2025年度校级本科质量工程拟立项名单.xls

本科生院（招生办公室）
2025年9月25日

（联系人：孙齐胜；电话：85288020）

分享至:

最新动态

2025-09-28
关于转发《举办第十二届中国现代农业发展论坛暨2025中国农学会年...

2025-09-28
关于开展广东长隆集团野生动物科研科普项目申报工作的通知

2025-09-27
华南农业大学2024-2025学年袁隆平追梦奖学金拟推荐名单公示

2025-09-27
关于举办华南农业大学首届大学生讲思政课比赛的通知

2025-09-27
关于推荐第二批中小学生研学实践教育优质课程名单的公示

48	教学改革项目	新农科背景下技术赋能与能力导向融合的实验教学改革——以《药用植物生态学实验》为例	自筹	林学与风景园林学院	龙凤玲
49	教学改革项目	基于“docker+WSL”轻量化构架的混合教学模式在《基因组学与生物信息学实验》中的应用	自筹	园艺学院	曾灶海
50	教学改革项目	AI音乐赋能园艺疗法与大学生心理健康教育的融合研究	自筹	园艺学院	李伟
51	教学改革项目	新农科背景下基于三茶融合视角的思政教学课程融合与路径探索——以《茶艺与茶文化学》为例	自筹	园艺学院	李丹
52	教学改革项目	《智慧树平台与影像病例库协同驱动的影像学教学创新与实践 ——— 基于兴趣激发与学习效果双维度优化》	自筹	兽医学院	陈孱蕾
53	教学改革项目	通过临床案例学习解剖学消化系统下消化道章节	自筹	兽医学院	许丹
54	教学改革项目	人工智能赋能的家畜行为学课程教学改革与实践	自筹	动物科学学院	张玲娜
55	教学改革项目	安全心理学视域下高校科研实验室安全管理的干预机制与路径研究	自筹	资源环境学院	谢洁芬
56	教学改革项目	面向全栈化与智慧化的《网络GIS》课程教学体系优化研究与实践	自筹	资源环境学院	谢健文
57	教学改革项目	基于实景三维中国建设背景下测绘综合应用实习教学改革	自筹	资源环境学院	陈俊林
58	教学改革项目	基于创新能力培养的《水产动物营养与饲料》课程教学改革与实践	自筹	海洋学院	陈世俊
59	教学改革项目	数智化背景下《海洋环境化学》的教学改革探索与实践	自筹	海洋学院	黄玉妹
60	教学改革项目	人工智能赋能基因工程智慧教学模式改革	自筹	生命科学学院	陈亮
61	教学改革项目	AI赋能“新农科”背景下植物生理学课程改革的探索与应用	自筹	生命科学学院	刘宇婷
62	教学改革项目	学科交叉融合助推卓越农林人才培养--以传感器与检测技术课程为例	自筹	工程学院	黄培奎
63	教学改革项目	基于AI赋能的《机械制造基础》课程“三位一体”贯通式教学改革与实践	自筹	工程学院	曹亚超
64	教学改革项目	“AI+教学”模式下控制理论课程思政教学体系构建与实践	自筹	工程学院	邢航
65	教学改革项目	基于OBE理念的混合AI智慧教学模式在机械制造工艺学和夹具设计课程中的应用与实践探索	自筹	工程学院	黄光文
66	教学改革项目	科研反哺教学在《食品包装学》课程中的探索与实践	自筹	食品学院	葛文娇
67	教学改革项目	虚拟仿真实验技术在“食品微生物检验实验”教学中的应用探索	自筹	食品学院	邹苑
68	教学改革项目	城市更新导向的智能数字化城市设计课程教学体系改革研究	自筹	水利与土木工程学院	屈寒飞
69	教学改革项目	基础工程学生可以带手机的课程考核改革实践探索	自筹	水利与土木工程学院	黄金林
70	教学改革项目	以智能建造为目标的土木工程专业升级转型及实践研究	自筹	水利与土木工程学院	杨雨冰
71	教学改革项目	AIGC赋能的《造型设计基础》课程教学改革研究	自筹	材料与能源学院	鲁群霞
72	教学改革项目	“AI赋能-产教融合-思政贯通”导向的《胶合材料学（双语）》新工科教学改革与实践	自筹	材料与能源学院	樊奇

华南农业大学文件

华南农教〔2024〕7号

关于公布华南农业大学2023年度课程思政示范项目建设名单的通知

各学院、部处、各单位:

根据《华南农业大学课程思政实施方案》(华农党发〔2022〕26号)精神和《关于开展2023年度校级课程思政示范建设项目申报工作的通知》要求，学校组织开展了2023年度课程思政示范项目评选工作。

经项目负责人申请、所在单位遴选推荐、学校组织专家评审、校内公示等程序，决定立项建设华南农业大学2023年度课程思政示范项目125项，其中包括工程学院等课程思政试点学院3个、农学专业课程思政教学示范团队等课程思政示范团队7个、《电机学》等课程思政示范课程24门、《“数值分析”第四章第一节拉格朗日插值法》等课程思政示范课堂31个、《现实主义电影:

从意大利“新现实主义”到当下华语电影中的“温暖现实主义”》等课程思政典型案例 60 个（名单详见附件），现予以公布。

本次立项的示范项目建设期至 2025 年 12 月，建设期内示范项目原则上不允许更换负责人或变更项目团队成员。各项目团队要严格按照项目建设任务及要求及时开展工作，加快推进课程思政改革，确保高质量完成建设目标。

请各学院充分认识课程思政改革的重要意义，认真贯彻《华南农业大学课程思政实施方案》，加强对教师的相关培训、指导、引领和支持，带动教师全员积极参与课程思政教学改革，持续深入抓典型、树标杆、推经验，全面提升本科人才培养质量。

附件：华南农业大学 2023 年度课程思政示范项目建设名单

华南农业大学
2024 年 1 月 21 日

公开方式：主动公开

华南农业大学党政办公室　　2024 年 1 月 23 日印发

kcsz2023068	典型案例	《工程热力学与传热学》第四章第二节：热能利用率和㶲效率	工程学院	张 烨	
kcsz2023069	典型案例	《半导体照明技术》“课程思政”教学案例	电子工程学院（人工智能学院）	胡旭波	
kcsz2023070	典型案例	大学英语口语 I《中国饮食文化：为何能走向世界》	国际教育学院（广州都柏林国际生命科学与技术学院）	邱 倩	
kcsz2023071	典型案例	《林业经济管理学》“课程思政”教学案例	经济管理学院	周 伟	
kcsz2023072	典型案例	《林木育种学》课程思政教学典型案例	林学与风景园林学院	周 玮	
kcsz2023073	典型案例	国际民事诉讼：海外流失文物的“回家”之路	人文与法学学院	官隆清	
kcsz2023074	典型案例	《机械制造工艺学》第一章第四节：定位原理（定位的分类及应用）	工程学院	曹亚超	
kcsz2023075	典型案例	水工建筑物——4.1 拱坝概述	水利与土木工程学院	刘 远	周浩澜
kcsz2023076	典型案例	《高等数学》课程思政教学案例—第一章第二节数列极限	数学与信息学院、软件学院	王雪琴	
kcsz2023077	典型案例	《机电一体化与过程控制》第五章第 4 节：串行数据通信	工程学院	马锐军	

奖 状

曹亚超 同志：

在 2025 年工程学院青年教师教学大赛暨智慧教学大赛中，表现突出，成绩显著，荣获

二 等 奖

特发此证，以资鼓励！

工程学院

2025 年 11 月 13

二、科研项目

受理编号：c252025040250100007　　项目编号：2025B0202100002

项目下达文号：粤科资字〔2025〕222号

广东省重点领域研发计划项目

课题任务书

项目名称：丘陵山区荔枝智能采收装备创制与应用

项目承担单位（甲方）：华南农业大学

项目负责人：李君

课题名称：荔枝机械化采收装备与多机协同作业技术研发

课题承担单位（乙方）：华南农业大学

课题负责人：曹亚超

起止时间：2025-11-01 至 2029-10-31

填写说明

一、课题任务书甲方即项目承担单位，乙方即课题承担单位。

二、任务书中的单位名称，请按规范全称填写，并与单位公章一致。

三、课题任务书中的单位名称，请按规范全称填写，并与单位公章一致。

四、任务书的起点时间不得早于项目申报时间（以申报书提交业务系统之日为准），不得迟于项目立项文件下达之日。

五、课题任务书内容须按照项目任务书据实填写，要遵循实事求是原则，无需凑够字数。

六、课题任务书填报不得降低双方约定好的考核指标，不得自行对主要研究内容作大的调整。任务书将作为项目与课题过程管理、综合绩效评价（验收）和监督评估的重要依据。

七、凡不填写内容的栏目，请用“无”表示。

八、乙方填写的任务书经甲方审核确认后，用A4纸打印、装订、签章。任务书一式六份，报课题承担单位和子课题承担单位的管理部门审核盖章后，分别由项目主持单位、课题承担单位和子课题负责人各保留2份。

九、本课题任务书自签字并加盖公章之日起生效，各方均应负本任务书的法律责任，不应受机构、人事变动的影响。

项目基本信息表

项目名称	丘陵山区荔枝智能采收装备创制与应用			
项目编号	2025B0202100002			
专项名称	精准农业及生态绿色技术（荔枝品质维持）			
专题名称	20250210--专题二：荔枝采收及质量安全监测关键技术、装备研发与应用		单位总数	5
经费预算	总投入 840.00 万元，其中省级财政科技资金投入 400 万元			
项目周期节点	起始时间	2025年 11月 01日	结束时间	2029年10月31日
	实施周期	共 47 个月	预计中期时间点	2027-10-31
项目牵头承担单位	单位名称	华南农业大学	单位性质	高等院校
	单位所在地	广东省-广州市-天河区	统一社会信用代码	124400004554165634
	通信地址	广东省-广州市-天河区五山路483号	邮政编码	510642
	银行账号	3602002609000310520	法定代表人姓名	薛红卫
	单位开户名称	华南农业大学		
	开户银行（全称）	广东广州工行五山支行		

课题负责人	姓名	曹亚超	性别	男	出生日期	[redacted]
	证件类型	身份证	证件号码	[redacted]		
	所在单位	华南农业大学				
	最高学位	博士				
	职称	讲师	职务	无		
	电子邮箱	yccaoryan@scau.edu.cn	移动电话	[redacted]		
课题联系人	姓名	施琳琳	电子邮箱	lynnshi@scau.edu.cn		
	固定电话	/	移动电话	[redacted]		
	证件类型	身份证	证件号码	[redacted]		
课题财务负责人	姓名	科研财务科	电子邮箱	176095023@qq.com		
	固定电话	020-85288032	移动电话	[redacted]		
	证件类型	身份证	证件号码	[redacted]		

一、任务书条款

第一条	甲乙两方根据《广东省人民政府关于印发广东省重点领域研发计划实施方案的通知 》（粤府〔2018〕84号）《广东省科学技术厅关于印发广东省重点领域研发计划“十四五”行动方案的通知》（粤科资字〔2022〕37号）《广东省人民政府办公厅关于改革完善省级财政科研经费使用管理的实施意见》（粤府办〔2022〕14号）《广东省财政厅广东省审计厅关于印发〈省级财政科研项目资金管理监督办法（2023年修订）〉的通知》（粤财规〔2023〕3号）等文件规定，以及有关法律、政策和管理要求，依据项目立项通知，为顺利完成（2025）年丘陵山区荔枝智能采收装备创制与应用专项项目（文件编号：粤科资字〔2025〕222号），特签署本任务书。
第二条	本项目以攻克关键核心技术、研发关键零部件和重大装备为目标，力争突破前沿性、引领性的技术，取得产业带动性强、技术自主可控的重大原创科技成果和自主知识产权。《项目申报书》和申报指南是本任务书填报的重要依据，任务书填报时不得降低考核指标，不得自行对主要研究任务作出调整。《项目申报书》、申报指南和本任务书将共同作为项目过程管理、验收结题和监督评估的重要依据。
第三条	甲方有权按照《广东省重点领域研发计划实施方案》进行资源整合，以目标为导向，合理优化课题承担单位、参与单位布局。甲方实行科技计划“放管服”改革，建立基于信任的管理制度,但有权按照有关规定采取日常监管、随机抽查、专项检查、中期评估、财务审计等方式对项目实施监督，并严格以本任务书中约定的任务、期限、目标和验收指标等具体内容作为监督依据。项目到期后，甲方依据本任务书对项目实施结果进行验收。甲方可根据《广东省科学技术厅科技计划项目科研诚信管理办法》（粤科规范字〔2024〕2号）对乙方进行科技计划信用管理。
第四条	乙方要建立以诚信为原则的自主管理制度，按如下要求执行项目：1.承担项目的核心研究任务。2.统筹协调做好资源分配和任务分工工作，履行项目组织实施和资金使用等方面的主体责任，对项目实施目标和财政资金绩效负责。3.完善单位内部控制制度和单位间监督制约机制。4.乙方负责协调落实项目自筹经费及有关保障条件，按照任务分工、任务量和时间进度合理分配和拨付财政资金，确保财政资金使用的安全有效,并签订单位间的合作协议。5.乙方及相关参与单位均应对财政资金实行专款专用，单独列账，并积极配合甲方（或委托专业机构等）进行的监督检查。6.乙方须积极配合甲方组织的评估检查；项目完成后，应主动申请验收结题。7.乙方应按照国家和省有关规定，提交科技报告及其他材料。8.项目负责人及主要研究开发成员应实质性参与项目组织实施，不得出现挂名现象。
第五条	项目经费可按单位性质、项目进展及评估情况分阶段拨付。
第六条	在履行本任务过程中，乙方及参与单位必须恪守科研道德准则、科研活动规范和科研诚信规定，严格遵守有关法律法规。涉及医学、生物技术和人工智能等敏感领域研究 ，应当按照国家有关规定设立伦理委员会，开展研究项目的伦理审查，遵循国际公认的科研伦理规范和生命伦理准则。
第七条	本项目主要研发活动应在广东省内开展，项目成果应优先在广东省内实施转化应用。项目形成的知识产权归属、使用和转移，按照国家和广东省有关法律、法规和政策执行。
第八条	按照《广东省科学技术厅关于科技成果登记与信息公开的实施办法》（粤科管字〔20 13〕127号）的规定，本项目产生的科技成果必须登记；登记完成后，科技管理部门根据文件要求，可在有关科技成果信息综合平台将登记信息（内容包括成果名称、成果完成单位、成果简介、成果完成人等）进行公开。
第九条	为促进职务科技成果转化，本项目形成的职务科技成果在项目验收完成后，自动纳入省职务科技成果“先用后转预备库”（经主管部门同意不纳入的除外）。成果完成方同意以“先用后转”方式转化的，成果自动从“先用后转预备库”进入“先用后转库 ”，予以公开发布；成果完成方不采取“先用后转”方式转化的，该成果3年内未完成转化，自动进入“先用后转库”予以公开发布。成果纳入“先用后转预备库”后完成转化的，成果完成人应及时提交佐证材料申请出库。对采取“先用后转”方式转化的，具体事宜由使用方与成果所有方另行约定。

第十条	各方应充分理解本任务书的内容并自愿签署本任务书。未尽事宜，协商解决或签订补充协议进一步明确，甲方拥有最终解释权。

二、项目验收指标

（一）技术及成果指标

1.核心考核指标

序号	成果名称	成果类型	验收指标	评测方式/方法
1	自适应仿形荔枝机械化采收装备	新产品	研制自适应仿形荔枝机械化采收装备1台，最大采收高度≥4m，采收作业效率相比人工提升200%以上，果实损伤率≤8%，并达到用人成本降低80%以上。硬件技术创新就绪度达到8级。	专家论证、用户评价、第三方评测等

2.高水平知识产权指标

序号	内容	类型	结题时状态	拟解决关键问题
1	荔枝自适应仿形围蔽采摘机	国内发明专利	授权	填补国内技术空白
2	荔枝机械化采收除杂协同作业方法	国内发明专利	授权	填补国内技术空白

对以上项目成果属于高质量知识产权的相关说明

发明专利1：创新性设计一种具有自适应仿形围蔽功能的荔枝机械化采摘装备。通过设计基于冠层仿形作业的两段式梳刷振动采摘机构和配套的一体化仿形围蔽装置，结合视觉感知算法获取果树冠层点云数据并对果实分布进行目标分割，突破传统机械式荔枝采收作业幅宽小、果实收集损失率高的关键痛点。部分结构及算法已在团队自研采摘原型机上完成部署，测试采收效率高。

发明专利2：创新提出一种荔枝机械化采收除杂协同作业方法。通过构建由采收装备与收集除杂装备组成的多机协同作业系统，设计分布式任务调度与协同控制算法，实现基于多机作业预测功能的一体化协同。该知识产权的落地将率先为行业低损高效采收除杂协同作业提供技术参考。

上述知识产权所用技术路径拥有高原创性，未构成与现有公开专利的重合；创新点集中、技术路线清晰完整，具有成为高质量知识产权的潜力。

3.技术创新就绪水平

当前技术创新就绪水平	中期评估时技术创新就绪水平	项目完成时技术创新就绪水平
5级	6级	8级

对项目实施后技术创新就绪水平提升情况的相关说明

项目实施后，总体技术就绪度从5级提升至8级，关键技术水平均有显著提升，达到应用或产业化水平，具体如下：自适应仿形荔枝机械化采收装备可实现荔枝的柔性采摘和围蔽收集功能。项目实施前研制了柔性梳刷采摘装置与配套仿形围蔽装置样机，开展了基于离散元的荔枝梳刷振动采摘果实损伤模拟，对荔

枝梳刷振动采摘试验验证和演示示范，达到了TRL5级；中期预计通过多源传感器对冠层轮廓与果实分布信息进行精准感知并优化采摘部件结构，提高采收作业幅宽，实现最大采收高度≥4m，采收作业效率相比人工提升200%以上，达到TRL6级；后期项目完成时，将进行基于采摘部件与自主作业性能优化的试验与推广示范，并在实际环境下充分使用，确保荔枝采净率≥90%，果实损伤率≤8%，达到TRL8级。

4.科技报告考核指标

序号	报告类型	提交时间	公开类别及时限
1	2026年度课题技术进展报告	2026-12	延期公开4年
2	2027年度课题技术进展报告	2027-12	延期公开4年
3	2028年度课题技术进展报告	2028-12	延期公开4年
4	2029年度课题技术进展报告	2029-10	延期公开4年

5.参考指标

（1）申请发明专利2件，授权发明专利2件，总计4件；（2）申请软件著作权3件；（3）发表学术论文4篇；（4）培养研究生12-14名。

（二）项目经济指标及社会效益

累计新增销售收入（万元，截至项目验收结题）	无
累计新增利税（万元，截至项目验收结题）	无

（三）项目其他经济指标说明

经济效益：相比现有机械采收技术，项目研究成果可减少果实损失20%以上，含杂率降低后节约保鲜分选人工成本50%，并有效延长商品货架期，间接经济效益可观。

（四）阶段性成果评价

序号	指标名称	立项时已有指标值/状态	中期指标值/状态	完成时指标值/状态	评估方式（方法）及评价手段
1	采收装备	爬坡度≥15°，荔枝采净率≥80%，含杂率≤10%，最大采收高度≥2.6m，采收作业效率相比人工提升80%以上，果实损伤率≤10%	爬坡度≥15°，荔枝采净率≥85%，含杂率≤5%，最大采收高度≥3.5m，采收作业效率相比人工提升150%以上，果实损伤率≤10%	爬坡度≥20°，荔枝采净率≥90%，含杂率≤5%，最大采收高度≥4m，采收作业效率相比人工提升200%以上，果实损伤率≤8%	专家论证意见、用户评价证明、第三方评测报告
2	发明专利	/	2件	4件	专利授权证书或受理通知书
3	论文	/	2篇	4篇	已发表论文全文或录用通知

4	软件著作权	/	1件	3件	软件著作权登记证书或受理通知书

三、项目研究内容、研究方法及技术路线、主要创新点

（一）项目拟解决的关键问题

（1）冠层接触式荔枝机械化采收的高效采收与围蔽减损问题

荔枝果树冠层结构复杂、果实分布均一化程度低，传统冠层接触式机械化采收装备多在开放空间作业，无法对果实的弹跳轨迹进行有效约束，导致漏果损失率较高。此外，采摘执行机构与冠层果实的空间包络度差、作业幅宽小，严重影响采摘效率。本项研究针对上述瓶颈，旨在研发可对目标树冠进行自适应仿形的荔枝机械化柔性采收与配套围蔽装置。如何根据冠层的三维形态特征与果实分布特性，结合振动采收装置的有效包络空间，实时决策仿形采收装置的空间位姿，同步实现采收区域冠层围蔽，是本项研究亟需解决的关键问题。

（二）项目的主要研究内容

（1）丘陵山地荔枝高效低损智能采收装备技术研发

① 荔枝冠层果实自适应仿形机械化采收装备创制

针对丘陵山地荔枝机械化采收装备作业幅宽小、冠层适应性差、果实收集损失率高等问题，开展自适应仿形围蔽的智能采收装备创制研究。基于果树冠层特征及果实分布特性，轻量化设计智能采收装备本体，创制具有冠层果实自适应仿形功能的两段式柔性梳刷振动采收装置和与之配套的一体化仿形围蔽装置；结合传感器实时获取的果实空间聚类信息，研究采摘部件空间位姿自适应仿形调控技术；构建基于冠层特征的仿形梳刷装置与围蔽收集装置的协同作业机制，限制采收过程中果实运动空间区域。集成并试制仿形围蔽式荔枝智能采收装备，以采净时间和损伤率为指标优化仿形结构与作业参数，开展整机可靠性及环境适应性等采收作业试验验证。

② 荔枝机械化采摘-收集-除杂多机协同作业技术研究

针对多机作业路径干扰大、协同效率低等问题，开展采摘-收集-除杂多机协同作业技术研究。构建由采收装备与收集除杂装备组成的多机协同作业系统，建立多机间状态感知与信息交互机制；融合果园环境高精度建图，研究多机作业路径规划与动态避让策略，设计分布式任务调度与协同控制算法，实现基于多机作业预测功能的一体化协同。以整机作业一致性、任务完成效率为评价指标，开展多机协同作业系统的可靠性与适应性试验验证。

（三）项目采取的研究方法及技术路线

（1）丘陵山地荔枝高效低损智能采收装备技术研发

设计具有冠层围蔽功能的可仿形两段式柔性梳刷振动采收装置，通过雷达和视觉传感器实时获取果树冠层点云数据以及果实分布图像，采用语义/实例分割算法对果实区域与果树冠层进行目标分割，拟合确定冠层轮廓特征，并基于果实空间聚类信息解算出振动采收机构空间姿态位置，进行采收围蔽装置的自适应仿形调整，根据试验结果优化结构与作业参数。

搭建半实物仿真平台，模拟采摘-收集-除杂作业场景，验证装置协同性。基于局部通信网络的信息交互机制，建立统一的多机状态描述协议与行为预测模型。结合作业任务与动态环境，设计分布式任务调度算法 。融合局部感知与全局环境，进行协同路径规划与避障作业试验验证。

（四）主要创新点

（1）基于冠层轮廓特征与果实分布特性的自适应仿形围蔽式荔枝机械化采收技术

突破现有荔枝振动采收机作业幅宽、冠形适应性的局限性，设计具有树冠自适应仿形功能的两段式宽幅柔性梳刷采收装置。通过雷达和视觉传感器实时获取果树冠层点云数据以及果实分布图像，确定冠层轮廓特征以及果实振动采收空间位置，基于采净时间和损伤率指标优化仿形作业参数，进行采收装置的姿态自适应调整，进一步提高采收作业效率；针对荔枝机械化采收过程中果实收集损失率高的问题，创制与采收装置配套的一体化仿形围蔽装置。通过感知围蔽部件与树冠的接触判断，自动对树冠结果区域进行采收围蔽 ,限制采收过程中果实运动方向，减少果实收集损失。该创新点革新了现有的水果振动式收获技术形态，形成具有自主知识产权的方法可引领簇状水果机械化采收技术的创新发展。

（2）丘陵山地荔枝机械采摘-折展收集-气力除杂的协同作业系统

为克服现有振动采摘机功能单一、多功能采收机结构复杂且体积大的局限性，采用仿形围蔽式荔枝采摘机与收集除杂一体化机的协同作业方案。通过路径规划与作业优化，实现丘陵山地荔枝园机械化采摘、收集、除杂环节的高效协同。该创新点形成的协同作业系统具有显著的原创性，针对荔枝树结果特性提出的机械采摘-折展收集-气力除杂的工作模式，作业效率高、集成度强、适应性好，有望解决荔枝产业机械化采收短板问题。

四、项目进度和阶段目标

（一）项目起止时间：2025年 11月 01日 至 2029年 10月 31日

（二）项目实施进度及阶段主要目标

开始日期	结束日期	主要工作内容	预期目标	成果形式
2025年 11月 01日	2026年 04月 30日	开展可仿形柔性梳刷振动采收装置的结构方案设计。	完成整体方案设计、可行性分析论证。	实施方案
2026年 05月 01日	2026年 10月 31日	开展仿形围蔽式振动执行机构关键部件的设计。	1）形成柔性梳刷振动采收装置和仿形围蔽装置。 2）申请专利1件。	专利，年度技术进展报告。
2026年 11月 01日	2027年 04月 30日	开展基于果实空间聚类信息的采收围蔽装置的自适应仿形调整研究。	1）形成采摘部件空间位姿自适应仿形调控技术。 2）申请专利1件，发表论文1篇。	论文、专利。
2027年 05月 01日	2027年 10月 31日	构建基于冠层特征的仿形梳刷装置与围蔽收集装置的协同作业机制研究，完成采收装备对果园信息的“感知-理解-决策”闭环系统集成测试。	1）形成仿形梳刷装置与围蔽收集装置的协同作业控制算法。 2）申请软件著作权1件，专利1件，发表论文1篇。	论文，软件著作权，年度技术进展报告。
2027年 11月 01日	2028年 04月 30日	开展仿形围蔽式荔枝智能采收装备技术模块与高适应性履带底盘的集成工作。	1）形成仿形围蔽式荔枝智能采收装备系统。 2）申请专利1件，发表论文1篇。	论文，专利

2028年 05月 01日	2028年 10月 31日	1）开展仿形围蔽式荔枝智能采收装备的果园环境功能试验，完成采收作业参数的优化工作。 2）开展采收装备与收集除杂装备的协同作业策略研究。开展丘陵山地荔枝机械化采收装备可靠性及环境适应性等采收作业试验验证。	1）形成荔枝机械化采摘-收集-除杂多机分布式任务调度与协同控制算法。 2）软件著作权1件，发表论文1篇。	论文，软件著作权，年度技术进展报告。
2028年 11月 01日	2029年 04月 30日	1）开展多机协同采收系统综合验证。 2）在基地生产应用，举办相关示范推广活动。	软件著作权1件。	软件著作权
2029年 05月 01日	2029年 10月 31日	1）环境适应性测试、动态避障试验等标准化流程。 2）整理项目成果资料，形成文档报告，准备项目验收。	完成项目的验收报告和项目成果资料的整理工作。	年度技术进展报告，验收报告。

五、知识产权对策、成果管理及合作权益分配

根据《中华人民共和国合同法》、《中华人民共和国专利法》、《中华人民共和国著作权法》等相关法律法规，以及科技部《关于加强与科技有关的知识产品保护和管理工作的若干意见》的规定，本项目各参与单位将遵循合作精神，针对项目申请和执行过程中涉及的知识产权、成果及合作权益分配，按照以下要求进行管理：

1.项目各方在申请项目之前所拥有的知识产权及相关权益归各自所有，不因共同申请项目而发生任何变更。

2.为项目申请所需，各方提供的未公开或已明确说明不得向第三方透露的与项目相关的技术资料、数据等信息，包括但不限于各自所有或合法持有的公式、流程、设计、产品、样品、发明、技术资料、版权、商标、研发计划等内容，未经提供方书面同意，禁止向第三方披露或使用。本条款在无论项目是否获得资助的情况下，均长期有效。

3.各方为项目申请提供的信息不应视为授予对方任何专利、著作权、商标等知识产权的许可。

4.在项目执行过程中，各方应及时对项目产生的科技成果采取以下知识产权保护措施：

对各方根据任务分工独立完成的科技成果及相应知识产权，归该方单独所有。

由多方共同完成的科技成果及其形成的知识产权则由各方共同所有。未经其他方同意，任何一方不得擅自向第三方转让共同科技成果的知识产权或技术资料。共同成果的精神权利，如身份权、荣誉称号、奖励证书及奖金等，由共同完成方共享。

5.对于共有科技成果，若实施许可或转让专利、非专利技术所产生的经济收益，将由各方共同分享。具体的收益分配方式应在相关行为实施前另行商定。

六、参与人员信息

课题负责人：							
姓名	性别	年龄	职务	职称	学位	在项目中承担的任务	所在单位
曹亚超	男	[redacted]	无	讲师	博士	荔枝机械化采收装备与多机协同作业技术研发	华南农业大学

主要研究开发人员：							
姓名	性别	年龄	职务	职称	学位	在项目中承担的任务	所在单位
施琳琳	女	31	院长助理	讲师	博士	分布式任务调度与协同控制算法设计	华南农业大学
黄成杰	男	[redacted]	无	副教授	博士	采收装备结构设计	华南农业大学
李钊	男	[redacted]	无	未取得	硕士	仿形围蔽装置结构设计	华南农业大学
李俞浩	男	[redacted]	无	未取得	硕士	机械化采收装备整机测试	华南农业大学
曾晔	男	[redacted]	无	未取得	硕士	多机作业路径规划算法设计	华南农业大学
罗明达	男	[redacted]	无	未取得	硕士	多机协同控制研究	华南农业大学
柯森蓝	男	[redacted]	无	未取得	学士	多机械臂路径规划研究	华南农业大学
刘盛龙	男	[redacted]	无	未取得	学士	多臂多机路径规划研究	华南农业大学
蔡佳敏	男	[redacted]	无	未取得	学士	多采收机器人路径规划与控制	华南农业大学
翁清林	男	[redacted]	无	未取得	学士	采摘部件空间位姿自适应仿形调控技术	华南农业大学
朱仲艺	男	[redacted]	无	未取得	学士	机械化采收装备试验验证	华南农业大学
韦标	男	[redacted]	无	未取得	学士	多机械化采收机器人协同控制研究	华南农业大学
黄明杰	男	[redacted]	无	未取得	学士	多采收机器人状态感知	华南农业大学
邓善鹏	男	[redacted]	无	未取得	学士	梳刷与围蔽收集装置协同作业	华南农业大学
麦煜炬	男	[redacted]	无	未取得	学士	自适应仿形调控技术	华南农业大学
王浩	男	[redacted]	无	未取得	学士	多机任务调度算法	华南农业大学
林晓婷	女	[redacted]	无	未取得	学士	轻量化采收装备	华南农业大学

詹茗杰	男	[redacted]	无	未取得	学士	整机可靠性及环境适应性测试	华南农业大学
钟柏洲	男	[redacted]	无	未取得	学士	整机可靠性及环境适应性测试	华南农业大学
马俊涛	男	[redacted]	无	未取得	学士	整机可靠性及环境适应性测试	华南农业大学

七、经费预算

课题承担单位基本情况表

填表说明：1.组织机构代码指企事业单位国家标准代码，单位若已三证合一请填写单位社会信用代码无组织机构代码的单位填写“000000000”；

2.单位公章名称必须与单位名称一致。

课题承担单位	单位名称	华南农业大学			
	组织机构代码	10564			
	单位法定代表人姓名	薛红卫			
	单位所属地区	省、直辖市、自治区等	地市（市、自治州、盟）	县市（区、旗）	
		广东省	广州市	天河区	
	电子邮箱	50002546@scau.com			
	通信地址	广东省广州市天河区五山路483号			
	邮政编码	510642			
	银行账号	3602-0026-0900-0310-520			
	单位开户名称	华南农业大学			
	开户银行（全称）	中国工商银行广州五山支行			
相关责任人	课题负责人	姓名	曹亚超		
		身份证号码	[redacted]		
		工作单位	华南农业大学		
		电话号码	[redacted]	手机号码	[redacted]
		电子邮箱	yccaoryan@scau.edu.cn	邮政编码	510642
		通信地址	广州市天河区五山路 483 号		
	财务部门负责人	姓名	科研财务科		
		身份证号码	[redacted]		
		电话号码	020-85288032	手机号码	[redacted]
		电子邮箱	176095023@qq.com		

课题预算表

金额单位：万元

	项目总经费		省级财政科技资金	
支出经费	经费额	用途说明	经费额	用途说明
1、直接费用	82.00	用于项目设备费、业务费和直接人力资源成本支出	82.00	用于项目设备费、业务费和直接人力资源成本支出
（1）设备费	0.00	无设备费支出	0.00	无设备费支出
（2）业务费	68.86	用于材料、测试化验加工、燃料动力、出版文献/信息传播/知识产权事务、会议/差旅/国际合作与交流等支出	68.86	用于材料、测试化验加工、燃料动力、出版文献/信息传播/知识产权事务、会议/差旅/国际合作与交流等支出
（3）直接人力资源成本	13.14	用于参与项目的研究生及临聘科研辅助人员劳务费、专家咨询费、人员费以及项目聘用的研究人员劳务费等支出	13.14	用于参与项目的研究生及临聘科研辅助人员劳务费以及专家咨询费等支出
2、间接费用	18.00	用于绩效支出、管理费用和其他间接成本等费用支出	18.00	用于绩效支出、管理费用和其他间接成本等费用支出
（1）绩效支出	2.60	项目组绩效支出	2.60	项目组绩效支出
（2）管理费用	6.00	单位管理费用支出	6.00	单位管理费用支出
（3）其他间接费用	9.40	项目其他间接成本支出	9.40	项目其他间接成本支出
合计	100.00		100.00	

其他需说明的情况

1.设备费、燃料动力费、人员费由自筹经费支出；

2.专家咨询费由省级财政科技资金支出；

3.材料费、测试化验加工费、出版文献/信息传播/知识产权事务费、会议/差旅/国际合作与交流费、劳务费由省级财政科技资金和自筹经费共同支出；

4.省级财政科技资金中的间接经费按（直接费用-设备费）*20%预算，其中设备费为0.00万元。

自筹资金投入情况说明：

无。

八、签约各方

项目承担单位：　华南农业大学　　（盖章，单位法人章或单位法人授权章） 项目负责人：李君 签字：李君 2025 年 12 月 23 日
课题承担单位：　华南农业大学　　（盖章，单位法人章或单位法人授权章） 课题负责人：曹亚超 签字：曹亚超 2025 年 12 月 23 日

任务书编号：2024A04J4131

广州市科技计划项目
任务书

项目名称：	恒定可调雅可比矩阵并联机构的型综合及“构型-性能”一体化设计方法研究
承担单位：	华南农业大学
项目负责人：	曹亚超
计划类别：	基础研究计划
专题名称：	2024年度基础与应用基础研究专题
支持方向：	青年博士“启航”项目
组织单位：	华南农业大学
起止时间：	2024-01-01 至 2025-12-31
主管处室：	基础研究处

广州市科学技术局制

二〇二四年

填写说明

1.任务书甲方为广州市科学技术局；乙方为项目承担单位；丙方为项目组织单位。

2.任务书基于项目申报书转换而成，请按照“广州科技大脑”提示在线填写核实，若存在不填写内容的栏目，请用“无”表示；任务书中的单位名称应为规范全称，并与单位公章一致。

3.乙方与合作单位的合作协议自动从项目申报书中读取，如需变化调整，须待任务书签订后，按要求及时办理重大变更。

4.乙方完成项目任务书在线填写，依次提交丙方和甲方审核确认后，按要求登录“穗好办”APP完成电子签章。不具备电子签章条件的单位，经与业务主管处室沟通对接后，可下载电子版项目任务书用A4纸双面打印装订签章；一式六份报甲方和丙方签章，其中甲方两份丙方两份，项目承担单位和项目负责人各一份。

5.涉密项目请在“广州科技大脑”下载项目任务书模板，按保密要求离线填写报送。

6.项目申报书是项目任务书填报的重要依据，未经甲方许可，乙方不得修改考核指标，调整主要研究内容。项目任务书将作为项目实施管理、验收结题和监督评估的重要依据。

7.项目任务书中的“备注”，包括重要的必须补充的内容。

8.“广州科技大脑”是项目管理过程中重要通知和文书的电子送达平台。为确保电子送达渠道畅通，乙方和项目负责人应及时更新维护“广州科技大脑”的单位和个人信息。

9.根据相关要求，项目涉及人体临床研究的，项目需经医学伦理委员会审查通过并在任务书附件栏上传相关佐证材料。

一、项目基本信息

项目基本信息	项目名称	恒定可调雅可比矩阵并联机构的型综合及“构型-性能”一体化设计方法研究
	申请市财政科技经费	5(万元)
	研究期限	2（年）
项目摘要	寻找机构拓扑结构学与运动学之间的映射规律是创建“构型-性能-尺度”一体化设计方法亟待解决的关键问题。对并联机构雅可比矩阵“恒定可调”的构型设计为建立构型和性能的关联提供新的思路。本项目通过探究雅可比矩阵、拓扑构型及性能之间的映射机理，提出机构雅可比“全恒可调”和“欠恒可调”的型综合理论和“构型-性能”一体化设计方法。研究成果可为创建高品质并联机构装备“构型-性能-尺度”一体化设计方法开拓新的视角。	

二、项目单位情况

项目承担单位	单位名称	华南农业大学	统一社会信用代码	124400004554165634
	注册时间	1952-01-01	单位类型	高等院校
	注册地址	广东省广州市天河区五山路483号		
	办公地址	广东省广州市天河区五山路483号		
	联系人	姓名	倪慧群	
		手机号码		
		电子邮箱	kjcgxk@scau.edu.cn	
	开户银行	广东广州工行五山支行		
	开户户名	华南农业大学		
	银行账号	3602002609000310520		

三、项目负责人信息

姓名	曹亚超	证件类型	身份证
证件号码		性别	男
出生日期		民族	汉族
国籍	中国	学历	博士研究生
学位	博士	学位授予国家（或地区）	中国
职务	无	职称	中级
所学专业	机械工程	手机号码	
办公电话		电子邮箱	yccaoryan@scau.ed

四、项目经费信息

本项目总投入：¥（5）万元，其中，市财政科技经费：¥（5）万元，自筹经费：¥（0）万元。

经费下达计划			
资金来源	小计	市财政科技经费	自筹经费
2024	5	5	0
总计	5	5	0

（单位：万元）

注：本专题纳入“包干制”，市财政科技经费按市科技计划项目经费“包干制”相关规定执行。

五、预期代表性成果

项目负责人在项目实施期内，以该项目作为资助项目获得以下5种情形之一且经费使用符合规定的，由组织单位审核后通过验收。

（一）项目实施期内，以第一作者/通讯作者发表论文1篇或以上（须标注资助项目编号）；

（二）项目实施期内，以第一完成人申请或授权专利、软件著作1项或以上；

（三）项目实施期内，获省级以上科技计划项目或人才项目支持1项或以上；

（四）项目实施期内，获省级以上科技奖励（含列入获奖团队成员名单）1项或以上；

（五）项目实施期内，获得职称晋升。

六、备注

专题补充约定条款：

甲方对未履行勤勉尽责义务的相关责任主体，自作出处理结论之日起，依照法律法规规定或任务书约定实施惩戒5年，取消相关责任主体申报市科技计划项目、申领市科技计划项目经费的资格。

预期代表性成果需在实施期内获得。

项目承担单位（乙方）及项目负责人承诺书

承诺书

本单位/本人作为广州市科技计划项目承担单位/项目负责人，将严格遵守广州市科技计划管理相关规定，严格履行自身责任，加强对项目组人员及合作单位的管理，在此郑重承诺：

（一）确保与本项目有关的全部材料真实、合法、有效，未侵犯其他方知识产权等权利，不存在多头申报、重复申报行为；

（二）严格遵守《广州市科技创新条例》《广州市科技计划项目管理办法》《广州市科技计划项目经费管理办法》《广州市科技计划科技报告管理办法》等相关规定，实施项目和经费管理；

（三）严格遵守国家、省、市关于科研诚信和科技伦理的有关法律、法规，相关政策以及各项规定，加强项目实施过程中的科研诚信及科技伦理管理，恪守科研道德准则。

如有违反，本单位/本人愿意接受相关部门做出的各项处理决定，包括但不限于终止项目、停拨经费、核减经费、追回经费，取消一定期限广州市科技计划项目申报资格，记入科研失信行为数据库，将不良行为向社会公开等。

项目承担单位：华南农业大学
日期：2023年12月16日

项目负责人：曹亚超
日期：2023年12月15日

任务书签署

甲乙丙三方根据《广州市科技计划项目管理办法》《广州市科技计划项目经费管理办法》《广州市科技计划科技报告管理办法》等有关文件规定，以及有关法律、政策和管理要求，签署本任务书。

签订地点：广州市越秀区

广州市科学技术局（甲方）：广州市科学技术局
局项目经办人：蒋韬略　　　　　　联系电话：83124150
责任处室负责人：麦胜文

2024年01月17日

项目承担单位（乙方）：华南农业大学
二级部门：华南农业大学工程学院
项目负责人：曹亚超
项目经费汇入账号
账户名：华南农业大学　　账号：3602002609000310520
开户银行：广东广州工行五山支行
财务负责人：肖斐

2023年12月16日

组织单位（丙方）：华南农业大学
项目经办人：倪慧群

2023年12月18日

申请代码	E0503
接收部门	
收件日期	
接收编号	5237053103

5237053103

国家自然科学基金

申 请 书

（2023版）

资助类别： 面上项目

亚类说明：

附注说明：

项目名称： 簇状水果采摘无人机结构减振机理与复杂场景下自主作业研究

申 请 人： 李君　**办公电话：** 020-85280523

依托单位： 华南农业大学

通讯地址： 广州市天河区五山路483号华南农业大学工程学院

邮政编码： 510642　**单位电话：** 020-85280070

电子邮箱： autojunli@scau.edu.cn

国家自然科学基金委员会

主要参与者（注：主要参与者不包括项目申请人）

编号	姓名	出生年月	性别	职 称	学 位	工作单位	项目分工	办公电话	证件号码
1	李继宇		男	教授	博士	华南农业大学	无人机动力学分析	02085281443	4**************9
2	曹亚超		男	讲师	博士	华南农业大学	执行器振动力学分析	020-85280632	1**************9
3	施琳琳		女	讲师	博士	华南农业大学	避障采摘规划与跟踪	020-85280783	3**************9

总人数统计（注：包括项目申请人、主要参与者及其他参与人员；勿重复计数）

总人数	高级职称	中级职称	初级职称	博士后	博士生	硕士生	本科生及其他学生	其他
10	2	2	0	0	2	4	0	0

国家自然科学基金资助项目批准通知

（预算制项目）

李君　先生/女士：

根据《国家自然科学基金条例》、相关项目管理办法规定和专家评审意见，国家自然科学基金委员会（以下简称自然科学基金委）决定资助您申请的项目。项目批准号：52375094，项目名称：簇状水果采摘无人机结构减振机理与复杂场景下自主作业研究，直接费用：50.00万元，项目起止年月：2024年01月至2027年12月，有关项目的评审意见及修改意见附后。

请您尽快登录科学基金网络信息系统（https://grants.nsfc.gov.cn），**认真阅读《国家自然科学基金资助项目计划书填报说明》并按要求填写《国家自然科学基金资助项目计划书》（以下简称计划书）**。对于有修改意见的项目，请您按修改意见及时调整计划书相关内容；如您对修改意见有异议，须在电子版计划书报送截止日期前向相关科学处提出。

请您将电子版计划书通过科学基金网络信息系统（https://grants.nsfc.gov.cn）提交，由依托单位审核后提交至自然科学基金委。自然科学基金委审核未通过者，将退回的电子版计划书修改后再行提交；审核通过者，打印纸质版计划书（一式两份，双面打印）并在项目负责人承诺栏签字，由依托单位科研、财务管理等部门审核、签章并在承诺栏加盖依托单位公章，且将申请书纸质签字盖章页订在其中一份计划书之后，一并报送至自然科学基金委项目材料接收工作组。纸质版计划书应当保证与审核通过的电子版计划书内容一致。**自然科学基金委将对申请书纸质签字盖章页进行审核，对存在问题的，允许依托单位进行一次修改或补齐。**

向自然科学基金委提交电子版计划书、报送纸质版计划书并补交申请书纸质签字盖章页截止时间节点如下：

1. **2023年9月7日16点：**提交电子版计划书的截止时间；
2. **2023年9月14日16点：**提交修改后电子版计划书的截止时间；
3. **2023年9月21日：**报送纸质版计划书（一式两份，其中一份包含申请书纸质签字盖章页）的截止时间。
4. **2023年10月7日：**报送修改后的申请书纸质签字盖章页的截止时间。

请按照以上规定及时提交电子版计划书，并报送纸质版计划书和申请书纸质签字盖章页，逾期不报计划书或申请书纸质签字盖章页且未说明理由的，视为自动放弃接受资助；未按要求修改或逾期提交申请书纸质签字盖章页者，将视情况给予暂缓拨付经费等处理。

附件：项目评审意见及修改意见表

国家自然科学基金委员会
2023年8月24日

2022年省级农业科技创新推广及农业资源与生态环境保护建设项目

以农产品为单元的广东省现代农业产业技术体系创新团队建设项目（龙眼）

任务合同书

创新团队名称：龙眼产业技术体系创新团队

岗位/基地名称：机械与信息化

专家/基地负责人姓名：李君

依托单位（公章）：华南农业大学

依托单位法定代表人：刘雅红

编制日期：二〇二二年七月

一、基本情况

填表说明:	1.组织机构代码指企事业单位国家标准代码，无组织机构代码的单位填写“000000000”；2.单位名称、单位公章名称及单位开户名称必须一致，如有特殊情况，需说明理由。				
承担单位	单位名称	华南农业大学			
	单位性质	□科研机构 ■高等院校 □推广机构 □企业 □其他			
	单位主管部门	广东省教育厅			
	单位组织机构代码	124400004554165634			
	单位法人代表姓名	刘雅红			
	单位开户名称	华南农业大学			
	开户银行（全称）	广东广州工行五山支行			
	银行账号	3602002609000310520			
	单位所属地区	广州市	（州、市、县等）	天河区	
	电子邮箱	kjcgxk@scau.edu.cn			
	通信地址	广东省广州市五山华南农业大学		联系电话	02085283435
	邮政编码	510642		传真号码	02085281885
相关责任人	岗位/基地负责人	姓名	李君		
		身份证号码	420111197810167318		
		工作单位	华南农业大学		
		电话号码	02085280868	手机号码	[redacted]
		电子邮箱	autojunli@scau.edu.cn	邮政编码	510642
		通信地址	广州市天河区五山路483号华南农业大学工程学院		
	联系人	姓名	曹亚超		
		电话号码	02085280873	手机号码	[redacted]
		传真号码	02085288201		
		电子邮箱	yccaoryan@scau.edu.cn		

二、团队人员基本情况表

填表说明：	1.职称分类：A、正高级 B、副高级 C、中级 D、初级 E、其他；
	2.人员分类代码：A、首席专家 B、岗位专家 C、站长 D、团队成员
	3.是否有工资性收入：是（否）

序号	姓名	身份证号码	工作单位	功能研究室/试验站/推广站	技术职称	是否有工资性收入	人员分类	承担任务
1	李　君	[redacted]	华南农业大学	功能研究室	A	是	B	全面负责
2	曹亚超	[redacted]	华南农业大学	功能研究室	C	是	D	驱动设计
3	施琳琳	[redacted]	华南农业大学	功能研究室	C	是	D	自动控制
4	黄光文	[redacted]	华南农业大学	功能研究室	C	是	D	施药机械
5	王慰祖	[redacted]	华南农业大学	功能研究室	B	是	D	修剪机械
6	李灯辉	[redacted]	华南农业大学	功能研究室	E	否	D	无人机
7	林嘉铨	[redacted]	华南农业大学	功能研究室	E	否	D	花量识别
8	林佩怡	[redacted]	华南农业大学	功能研究室	E	否	D	果实监测
9	凌广鑫	[redacted]	华南农业大学	功能研究室	E	否	D	疏花技术
10	伍源水	[redacted]	华南农业大学	功能研究室	E	否	D	数据传输
11	陈　渊	[redacted]	华南农业大学	功能研究室	E	否	D	信息采集
12	吴鹏飞	[redacted]	华南农业大学	功能研究室	E	否	D	管控平台

一、目的及意义

主要说明项目的建设目的、研究价值和意义。

广东省龙眼园以山地栽培为主，适用机械不足、信息化管控水平滞后，用工量大且集中。随着劳动力的严重匮乏，对产业生产机械化的发展需求日益加大。近年来国家和地方一系列政策文件的出台，为龙眼产业机械化与信息化应用创造了良好的政策环境。

项目围绕龙眼园生产机械化、信息化管控的关键技术问题，立足于装备与系统的实用性和可靠性，采用机构设计、控制开发、仿真模拟与样机试验相结合的研究方法，进行信息传感、控制决策、机械作业和信息管控的相关技术与装备研发，通过样机试制与果园实地试验，改进与定型技术与装备。协同创新团队的其他岗位专家与试验站开展科技服务、技术培训与示范等工作，对于推进广东省龙眼产业现代化发展具有重要的意义。

二、项目建设内容

1. 结合多传感器融合技术，获取龙眼花穗果实特征信息，完成调试与田间试验；
2. 开发自走式疏花机的自动化作业控制功能，完成调试与田间试验；
3. 对示范点进行信息化功能完善，初步具备部分系统参数采集功能；
4. 开展技术培训与机械示范推广，举办相关技术培训 1-2 次，培训人员 20-30 人；
5. 整理形成国内外相关生产机械化与信息化技术的年度研究进展报告。

三、项目绩效目标 主要说明项目实施后，预期达到的目标和产生的效果，相关表述应尽可能量化。 项目实施后，预期突破龙眼花穗果实特征识别技术 1 种，研制改进果园自走式疏花机 1 种，作业机具的改进有利于进一步降低劳动强度、减少人工成本和提高作业效率；建成信息化初步管控果园 1 个，有利于提高示范果园的信息管控水平；开展机械作业观摩会或现场培训会 1 次，培训合作社、种植户代表、基层农业科技人员等共 20 人以上，通过培养地方农机化技术与管理人才带动主产区的龙眼产业转型升级发展。

四、项目工作进度安排（2022年8月1日-2023年7月31日）

详细说明各阶段的工作内容和时间安排情况。

2022年8月1日-2022年11月30日：拓展自走式疏花机的自动化功能，完成1种自走式疏花机械的自控优化，试验测试样机功能。

2022年12月1日-2023年03月30日：开发龙眼花穗果实特征识别技术，完成试验与功能验证；进行技术培训与推广，举办技术培训1-2次，培训人员20-30人。

2023年4月1日-2022年07月31日：进行示范点信息化功能初步完善，优化信息化示范点的数据监测平台。

七、资金使用预算

主要说明资金使用的范围或方向及资金使用进度安排。

序号	预算科目名称	合计	省级财政专项资金	其他来源资金
	（1）	（2）	（3）	（4）
1	**一、资金支出**	7.0	7.0	/
2	（一）直接费用	6.3	6.3	/
3	1.设备费	0	0	/
4	2.材料费	1.0	1.0	/
5	3.测试化验加工费	1.8	1.8	/
6	4.燃料动力费	0	0	/
7	5.出版/文献/信息传播/知识产权事务费	0.5	0.5	/
8	6.会议/差旅/国际合作交流费	1.0	1.0	/
9	7.培训费	0	0	/
10	8.劳务费	2.0	2.0	/
11	9.专家咨询费	0	0	/
12	10.其他支出	0	0	/
13	（二）间接费用	0.7	0.7	/
14	**二、项目资金来源**			
15	（一）省级财政专项资金	7.0	7.0	/
16	（二）其他来源资金	/	/	0
17	1.单位自筹资金	/	/	0
18	2.其他资金	/	/	0

在2022年12月完成 50%以上资金使用， 2023年7月完成 100%资金使用。

八、保障措施

说明围绕完成项目任务、目标所要采取的具体措施。

1 首席与各岗、综合基地负责人签订任务书，明确各单位任务分工和考核指标，推进技术研发、试验示范，培训推广。完成任务指标和质量纳入年度或中期考评。

2 专项经费纳入首席专家及各专题岗位专家所在单位财务统一管理，单独核算，确保专款专用，严格按照财务制度使用经费，合理推进经费使用进度。需从首席单位外拨到各岗、基地依托单位时，在签订任务书 1 周内，按照财政资金支付管理的有关规定及时下拨。各专题岗位专家所在单位严格按照任务书的经费预算执行，并编制经费年度财务决算报告。团队经费决算报告由首席专家所在单位财务部门会同首席专家编制。资金使用情况将纳入年度考评。

3 建立岗站对接制度，要求岗位专家至少每年对接高州产业园区和综合示范基地 3 次，通过中国农技推广平台打卡，为园区全产业链提供全方位技术支持。对接产业园区和区域示范基地的次数和工作内容将纳入年度考评。

4 实行年度总结与考评，对标任务指标进行考评，成立团队自评小组，聘请国家体系专家和有关领导为考评专家，进行年度考评，接受专家对体系建设的建议。施行激励和退出机制，对考评落后的岗、站实施经费减额，对完成任务质量优秀者经费增额，不合格者将退出团队。

具体实施办法和程序参照《广东省现代农业产业技术体系创新团队建设实施方案（2019-2023 年）实施。

九、合同条款

第一条 合同签约各方根据《中华人民共和国合同法》及国家有关法规和规定，经协商一致，特订立本合同，作为甲乙丙三方在项目实施管理过程中共同遵守的依据。

第二条 甲方的权利义务：1.按合同书规定进行经费核拨及有关工作协调。2.按照合同约定，对乙方项目的实施情况和经费到位、使用情况进行监督、检查。3.根据有关规定，对乙方进行信用管理。

第三条 乙方的权利义务：1.为项目实施提供技术与条件保障。2.按合同书规定，对甲方核拨的经费做到专款专用，单独列账，并随时配合甲方进行监督检查。3.按照合同要求准时完成项目内容，项目验收后，提交验收报告和审计报告。

第四条 丙方的权利义务：负责对项目承担单位的实施条件、能力以及财务管理规范进行审查，对推荐项目的实施场地、申报资料等进行真实性审核，并监督项目实施、经费预算执行情况，受委托或协助甲方完成项目验收等工作，并及时向甲方报告情况。

第五条 在履行本合同的过程中，如出现相关政策法规重大改变等不可抗力情况，甲方有权对所核拨经费的数量和时间进行相应调整。因非不可抗力因素导致的项目未履行或未履行完毕，或因乙方责任造成项目终止的，甲方有权终止项目合同，收回尚未使用和使用不符合规定的财政经费。

第六条 在履行本合同的过程中，当事人一方发现可能导致项目整体或部分失败的情形时，应及时通知另一方，并采取适当措施减少损失，没有及时通知并采取适当措施，致使损失扩大的，应当就扩大的损失承担责任。

第七条 实施项目所获得的科技成果（知识产权）归属、成果转让和实施技术成果所产生的经济利益的分享，除双方另有约定外，按照国家和广东省有关规定执行。

第八条 有关合同的未尽事宜，按照国家、省有关专项项目和经费管理的规定执行。

第九条 本合同经甲乙丙三方签字盖章后生效，甲、乙、丙三方各执一份，均具有同等法律效力。

六、补充内容及相关说明
无。

七、单位签章

岗位依托单位	承担单位（公章）	华南农业大学
	负责人（签章）	刘雅红 刘雅红
	岗位专家/基地负责人（签章）	李君 李君
	签订日期	2022 年 7 月 18 日
	地址及邮编	广州市天河区五山路 483 号华南农业大学工程学院，510642
	电话及传真	020-85280686，020-85288201
	单位名称	华南农业大学
团队依托单位	首席专家所在单位（公章）	华南农业大学
	首席专家（签章）	黄旭明
	签订日期	2022 年 7 月 18 日
	项目联系人	黄旭明
	地址和邮编	广州天河区华南农业大学园艺学院 510642
	电话及传真	020-85288273

三、论文、著作等

SCAULIB202625972

检索证明

根据委托人提供的论文材料，委托人**华南农业大学工程学院 曹亚超(学科类型:自然科学)** 2 篇论文收录情况如下表。

序号	论文名称	发表刊物及发表的年月卷期/页码等	作者排名	论文等级	作者文中单位	收录情况	影响因子	中科院大类分区
1	Research on gas-liquid coupled flow field dynamics and atomization characteristics of multi-duct sprayers based on CFD	FRONTIERS IN PLANT SCIENCE 出版年：2025 出版日期：NOV 20 卷期：16 页码：- 文献号：1616371 文献类型：Article	通讯作者	A 类	华南农业大学 工程学院	SCI	IF2-year=4.8 IF5-year=5.7 （2024）	生物学 2 区 Top 期刊：否 OA 期刊：是 标注：Mega-Journal （2025）
2	Research on Path Tracking for an Orchard Mowing Robot Based on Cascaded Model Predictive Control and Anti-Slip Drive Control	AGRONOMY-BASEL 出版年：2023 出版日期：MAY 18 卷期：13 5 页码：- 文献号：1395 文献类型：Article	通讯作者	A 类	华南农业大学 工程学院	SCI	IF2-year=3.3 IF5-year=3.7 （2023）	农林科学 2 区 Top 期刊：否 OA 期刊：是 （2023）

说明：论文等级和中科院大类分区按《华南农业大学学术论文评价方案（试行）》划分。

报告免责声明：如未盖章，报告无效

检索员：田成
华南农业大学图书馆
2026-03-12

agronomy

MDPI

Article

Research on Path Tracking for an Orchard Mowing Robot Based on Cascaded Model Predictive Control and Anti-Slip Drive Control

Jun Li [1,2], Sifan Wang [1], Wenyu Zhang [1], Haomin Li [1], Ye Zeng [1], Tao Wang [1], Ke Fei [1], Xinrui Qiu [1], Runpeng Jiang [1], Chaodong Mai [1] and Yachao Cao [1,*]

[1] College of Engineering, South China Agricultural University, Guangzhou 510642, China; autojunli@scau.edu.cn (J.L.)
[2] Guangdong Laboratory for Lingnan Modern Agriculture, Guangzhou 510642, China
* Correspondence: yccaoryan@scau.edu.cn; Tel.: +86-020-8528-0632

Abstract: In complex orchard environments, orchard mowing robots are prone to longitudinal slippage because of the characteristics of tires and the adhesion conditions of the road surface, which makes it difficult for the robots to maintain high-precision path tracking and autonomous navigation positioning. This not only affects the accuracy of path tracking but also leads to unstable motion for the mowing robots. To solve the above problems, we take an orchard mowing robot as the control object and establish a cascaded path-tracking controller and an adaptive time domain model based on a kinematics model. By designing a linear error model, an objective function, and constraint conditions for the mowing robot, the optimal linear velocity and angular velocity of the mower are obtained and converted into the speed of the driving wheel. Then, an anti-slip driving controller is designed based on fuzzy control of the slip rate. The slip-rate-based fuzzy controller is constructed according to the real-time speed of the mower and the reference speed of the driving wheel solved by the model predictive controller, and anti-slip driving control is implemented through a combination of a PID controller and a tire dynamics model. To verify the effectiveness of the proposed method, simulation and field experiments are conducted. The experimental results show that the slip rate of the driving wheel of the mower remains within the target slip rate range in the orchard working environment, avoiding excessive driving wheel sliding. Furthermore, the average lateral error of the path-tracking controller is controlled within 0.05 m, and the average value of the longitudinal error is kept within 0.04 m, which satisfies the control accuracy requirements of lawn mower operations. The proposed method provides a reference optimization scheme for improving the path-tracking and motion stability of a mowing robot.

Keywords: mowing robot; path tracking; model predictive control; fuzzy control; slip rate

Citation: Li, J.; Wang, S.; Zhang, W.; Li, H.; Zeng, Y.; Wang, T.; Fei, K.; Qiu, X.; Jiang, R.; Mai, C.; et al. Research on Path Tracking for an Orchard Mowing Robot Based on Cascaded Model Predictive Control and Anti-Slip Drive Control. *Agronomy* **2023**, *13*, 1395. https://doi.org/10.3390/agronomy13051395

Academic Editors: Xiaoli Zhang, Dengsheng Lu, Xiujuan Chai, Guijun Yang and Langning Huo

Received: 15 April 2023
Revised: 13 May 2023
Accepted: 14 May 2023
Published: 18 May 2023

1. Introduction

Weeds pose a significant threat to the growth of fruit trees and affect the growth of fruit in orchards. Orchard weeding is an important part of fruit production, and mowing machinery can be used to effectively remove weeds and promote fruit tree production. Traditional weeding machinery has a large manual workload and high labor intensity and requires large amounts of manpower, funds, and time, seriously affecting the large-scale development of orchards [1]. In recent years, unmanned lawn-mowing robots have emerged and have become widely used. With their flexible motion modes and precise navigation and positioning systems, they have been widely used in work environments with simple terrain, effectively reducing labor costs and labor intensity [2]. However, the robot is affected by the complex orchard environment, which makes it easy for it to slip and pitch, as well as making it prone to other difficulties. During orchard operations, the posture of the mowing robot fluctuates greatly because of many interference factors.

Therefore, it is necessary to solve the problem of mowing robots having difficulty carrying out autonomous operations and maintaining path tracking smoothly.

Safe operations and path tracking are the core research issues related to unmanned lawn-mowing robots. Among them, control algorithms directly affect the stable operation of lawn-mowing robots and the accuracy of automatic navigation and positioning systems, thereby affecting the efficiency of lawn-mowing and fruit tree production. In recent years, scholars have conducted extensive research on the work efficiency, continuous and stable operation, and path-tracking control of unmanned agricultural machinery in complex operating environments, mainly using model predictive control (MPC), fuzzy control, pure tracking control, PID control, and linear quadratic regulator (LQR) control [3–10]. Yangyang [11] proposed an agricultural machine path-tracking algorithm based on optimal target points. Compared with the Pure Pursuit algorithm, the tracking error is reduced by more than 20%, and the tracking accuracy is significantly improved. Chenyuan Sun [12] proposed a distributed-drive agricultural vehicle based on multi-information fusion, in which the torque required by the wheels is distributed through a sliding mode control and incremental proportional integral control so that the total traction coefficient of each wheel is consistent, and the vehicle runs in a straight line to solve the problem of excessive wheel sliding, but the accuracy of path tracking is not solved.

However, these algorithms generally ignore the kinematics of agricultural machinery during driving and the dynamic constraints of the vehicle body. Model predictive control can establish corresponding models for special problems, consider multiple system constraints, predict future times, and conduct rolling optimization online in real time. Numerous studies have shown that the MPC algorithm is well suited for path-tracking problems with high real-time requirements, high accuracy requirements, and multi-input/output system constraints [13,14]. Guohai Liu [15] built a path-tracking controller and a self-tuning controller based on the kinematic model of a four-wheel independent-drive high-clearance spray. The model predictive controller was used as the main controller to achieve path-tracking control so that the lateral deviation of the spray could be controlled within 0.0141 m. Jiahong Xu [16] focused on the operational efficiency of agricultural machinery and proposed a new efficiency-oriented model predictive control (EfiMPC)-based path-tracking control algorithm to achieve optimal control and further improve the operational efficiency of agricultural machinery. Manikandan Sundaram [17] proposed an improved curve perception MPC (C-MPC) algorithm for navigating curved paths; their approach can effectively eliminate path noise on terrain such as farmland and has low horizontal and vertical errors. Jie He [18] established a kinematic model based on modifying the position and pose of agricultural machinery to obtain a linear error model, an objective function, and constraint conditions for agricultural machinery to perform path tracking, aiming at the sideration and skidding of agricultural machinery in a complex paddy field environment. The agricultural machinery body was taken as the control object, and the agricultural machinery position and pose were taken as the observation values. The average root-mean-square error of the three-line path-tracking result was 0.043 m, and the average absolute error was 0.033 m. Huang [19] proposed an integrated kinematics and dynamics model for unmanned vehicles, proposed a path-tracking controller based on MPC, and conducted a VE-DYNA-Simmink cosimulation under different speeds and road friction coefficients. The results showed that the algorithm has good tracking performance. Linhe Ge [20] designed an offset-free MPC solver that uses MPC to directly solve longitudinal and transverse coupling problems. Simulation results showed that the algorithm could attain better tracking accuracy and high-speed stability by considering longitudinal and transverse coupling constraints. The average time required to complete all computations was only 5 ms.

In summary, a path-tracking algorithm based on MPC can effectively solve the problems of agricultural machinery in navigation and path tracking, but it does not solve the problem of the driving wheel skidding in the orchard environment. In this paper, a cascade path-tracking control method for orchard mowing robots is designed, which is based on the linear time-varying kinematic model of a four-wheel mower. The fixed time domain is difficult to adapt to the complex orchard environment, and to solve that problem, an adaptive time domain model predictive controller is designed. Aiming at the complex and varied road conditions of the orchard, a driving anti-skid controller was constructed using fuzzy control and the PID algorithm to realize driving anti-skid control. The proposed method improved the stability and the path-tracking accuracy of an orchard mowing robot.

2. Materials and Methods

2.1. Test Materials

To test the proposed path-tracking control method for an orchard mowing robot based on cascaded MPC and anti-skid drive control, the four-wheel differential mowing robot developed by the National Lychee and Longan Industrial Technology System Team of South China Agricultural University, which is mainly composed of a driving system, mowing system, and control system, is used as the experimental platform. The mowing system is connected to the body through an electric push rod, and the stubble-height CAN is adjusted through the electric push rod. The MPC controller is connected to the lower machine controller through the CAN port, which coordinates with the rotary coding sensor to control the motion of the mower. Figure 1 shows the mowing robot prototype. Table 1 shows the main technical parameters of the mowing robot.

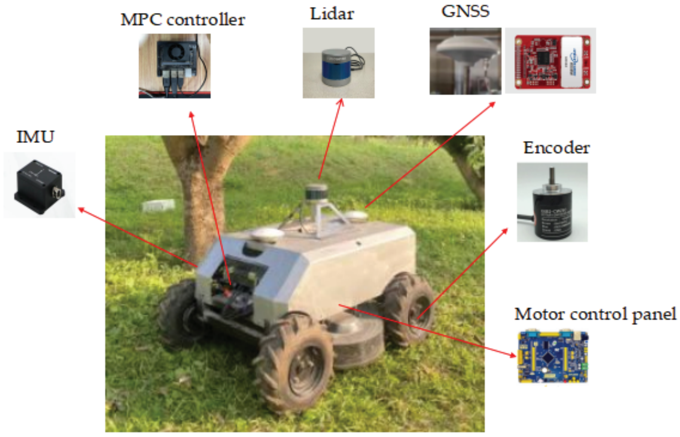

Figure 1. Lawn mower and sensors.

Table 1. Main technical parameters of the lawn mower.

Technical Parameters	Parameters
Length × width × height	1051 × 831 × 460 (mm)
Wheel track (*B*)	593 (mm)
Wheelbase (*L*)	715 (mm)
Working speed	0–1.5 (m/s)
Drive form	Four-wheel independent drive
Communication interface	CAN
Mowing robot quality	70 ± 1 (kg)
Wheel radius	165 (mm)
Rated motor power	350 (W)
Maximum motor speed	1500 (rad/min)

The position, attitude (heading angle, pitch angle, and roll angle), angular velocity, acceleration, and traveling speed of the mowing robot are measured using GPS, an IMU, and a wheeled odometer, as shown in Figure 1. The IMU sensor is installed horizontally forward inside the body shell, GPS antennas are installed in pairs on the roof, and the encoder is installed coaxially with the motor. The static measurement accuracy of the IMU sensor is 0.05°, the dynamic measurement accuracy is 0.1°, and the maximum output frequency is 400 Hz. During testing, the update frequency of the IMU is set to 50 Hz, and that of the GPS is set to 10 Hz.

The speed of the four wheels of the mowing robot is measured by an OMRON photoelectric encoder, as shown in Figure 1. The resolution of the adopted encoder is 2000 pulse/rotation (P/R), and the sampling period of the wheel speed is set to 20 ms for testing.

2.2. Experimental Methods

2.2.1. Method Design for Measuring the Slip Rate of a Mowing Robot

In the orchard environment, the running speed of the mowing robot and the motion path are set as shown in Figure 2. Through autonomous navigation, the starting point and ending point of the mowing robot are set, its real-time speed and the real-time speed of the four wheels in the motion path are recorded, and the real-time slip rate of the mowing robot is obtained under the working state according to the real-time speed of the mowing robot and the motor speed.

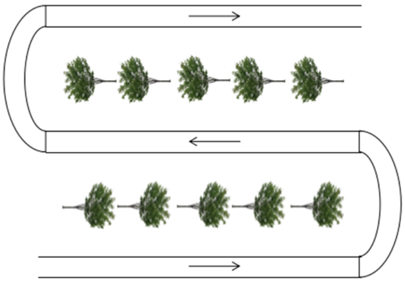

Figure 2. Schematic diagram of the reference path.

2.2.2. Path-Tracking Parameter Definition

To verify the effectiveness of the control method proposed in the following section, a four-wheel differential lawn mower platform is used to perform a path-tracking experiment and a slide rate control experiment in a standard orchard at South China Agricultural University. According to the actual situation of the orchard, the operation route of the lawn mower adopts a full coverage path. At the same time, to ensure that the simulation path is consistent with the actual working path of the lawn mower, the standard orchard is measured. The distance of each straight path is approximately 25 m, and the turning path is approximately 10 m.

Path tracking requires not only the state quantity of the lawn mower itself but also the corresponding reference path, which consists of information such as the position and attitude tracked by the lawn mower. Before building the control system, the reference path needs to be defined, as shown in Figure 2. Navigation equipment can provide effective positioning data, mainly using the longitude, L; latitude, B; and heading angle, φ. The reference path is generally composed of discrete reference waypoints, whose coordinates are longitudes and latitudes (L,B,φ) in the WGS-84 coordinate system. It is necessary to first convert these coordinates to the geodetic coordinate system (the Gauss–Kruger projection method is adopted) [21] and then to the body plane coordinate system [13], and the reference path obtained after transformation is used as the simulation reference path in MATLAB.

3. Mower Path-Tracking Controller Design Based on Adaptive MPC and Slip-Rate-Based Fuzzy Control

3.1. Four-Wheel Differential Kinematic Model of the Lawn Mower

Regarding the wheeled lawn mower platform, the motor can drive the wheels and change the wheel speeds independently. Therefore, the essence of path tracking for the lawn mower is to adjust the torque of each wheel in real time. The torque outputs of different wheels control the motor, allowing the speeds of the lawn mower in different directions to be generated to realize straight running and steering for the lawn mower. Because the mower uses differential steering, in which the left and right wheels of the mower run at different speeds, the mower is able to turn. Therefore, the geometric center of the robot is taken as the origin of the coordinate system of the lawn mower, and c denotes the instantaneous center of the lawn mower's steering. A kinematic model of the lawn mower is developed in Figure 3.

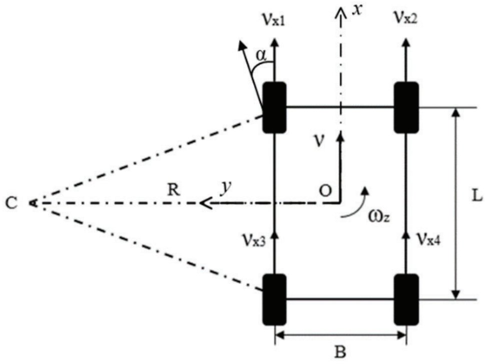

Figure 3. Kinematic model of a four-wheel differential-speed lawn mower.

Taking the forward direction of the lawn mower body as the x-axis, the rotation axis is perpendicular to the vehicle and upward, and the counterclockwise direction is specified as forward rotation without considering the lateral motion of the body, ω (i = 1, 2, 3, 4), or the rotational speeds of the four wheels, namely, the motor speed; v is the translational speed of the mower along the x-axis, and v is the angular velocity of the geometric center of the mower. The angle between the actual velocity of the tire and the orientation of the tire is the tire sideslip angle.

After completing the corresponding matrix transformation, the state equation of a four-wheel independent-drive lawn mower can be derived, as shown in Equation (1):

$$\begin{aligned}\begin{pmatrix}\dot{x}\\ \dot{y}\\ \dot{\theta}\end{pmatrix}=\begin{pmatrix}cos\theta & 0\\ sin\theta & 0\\ 0 & 1\end{pmatrix}\begin{pmatrix}v\\ \omega\end{pmatrix}&=\begin{pmatrix}\frac{r}{4}cos\theta & \frac{r}{4}cos\theta & \frac{r}{4}cos\theta & \frac{r}{4}cos\theta\\ \frac{r}{4}sin\theta & \frac{r}{4}sin\theta & \frac{r}{4}sin\theta & \frac{r}{4}sin\theta\\ -\frac{r}{2B} & -\frac{r}{2B} & -\frac{r}{2B} & -\frac{r}{2B}\end{pmatrix}\begin{pmatrix}\omega_1\\ \omega_2\\ \omega_3\\ \omega_4\end{pmatrix}\\ &=\begin{pmatrix}\frac{1}{4}cos\theta & \frac{1}{4}cos\theta & \frac{1}{4}cos\theta & \frac{1}{4}cos\theta\\ \frac{1}{4}sin\theta & \frac{1}{4}sin\theta & \frac{1}{4}sin\theta & \frac{1}{4}sin\theta\\ -\frac{1}{2B} & -\frac{1}{2B} & -\frac{1}{2B} & -\frac{1}{2B}\end{pmatrix}\begin{pmatrix}v_1\\ v_2\\ v_3\\ v_4\end{pmatrix}\end{aligned} \tag{1}$$

where ω_i (i = 1, 2, 3, 4) refers to the wheel angular velocity, r is the wheel radius of the lawn mower, v_i (i = 1, 2, 3, 4) is the wheel edge line velocity, B is the track width, and ω and v are the angular velocity and linear velocity of the geometric center of the lawn mower, respectively.

As shown in Equation (1), the motion state of a four-wheel independent-drive lawn mower in the x- and y-axis directions is described, and the components, angular velocity, and wheel rotation angular velocity of the lawn mower travel speed along the x and y coordinate axes are determined, ω_i (i = 1, 2, 3, 4), producing the relationship between the wheel edge velocities, v_i (i = 1, 2, 3, 4).

3.2. Design of an Adaptive Time Domain Model of a Predictive Controller

3.2.1. Linear Error Discretization of the Kinematic Lawn Mower Model

According to the state equation shown in Equation (1), the system can be regarded as an input with $u = (v, \omega)^T$, and the state variables are $\chi = (x, y, \theta)^T$. The general form of the linear control system of T is shown in Equation (2) [14]. The heading angle of the lawn mower, θ, is equal to the angle between the geometric center of the lawn mower and the x-axis.

$$\dot{\chi} = f(\chi, u) \tag{2}$$

If the working path of the mower acquired based on GPS is taken as the reference path and each path point on the reference path satisfies the established kinematic equation, then a kinematic model that satisfies the preset conditions is shown in Equation (3):

$$\dot{\chi}_r = f(\chi_r, u_r) \tag{3}$$

where $\chi_r = (x_r, y_r, \theta_r)^T, u_r = (v_r, \omega_r)^T$.

By expanding the above equation using Taylor's formula at the first reference point of the reference path [20] and ignoring higher-order terms, the linear error model of the lawn mower is obtained, as shown in Equation (4):

$$\dot{\chi} = f(\chi_r, u_r) + \frac{\partial f(\chi, u)}{\partial \chi} \Big|_{\substack{\chi = \chi_r \\ u = u_r}} (\chi - \chi_r) + \frac{\partial f(\chi, u)}{\partial u} \Big|_{\substack{\chi = \chi_r \\ u = u_r}} (u - u_r) \tag{4}$$

The linearized error model of the lawn mower can be calculated by combining the above two equations:

$$\dot{\tilde{\chi}} = \begin{pmatrix} \dot{x} - \dot{x}_r \\ \dot{y} - \dot{y}_r \\ \dot{\theta} - \dot{\theta}_r \end{pmatrix} = \mathrm{A} \begin{pmatrix} x - x_r \\ y - y_r \\ \theta - \theta_r \end{pmatrix} = \mathrm{A} + \mathrm{B} \begin{pmatrix} v - v_r \\ \omega - \omega_r \end{pmatrix} \tag{5}$$

In the equation, A and B are the Jacobian matrices of f with respect to x and u, respectively; A = $\begin{pmatrix} 0 & 0 & -v_r sin\theta_r \\ 0 & 0 & v_r cos\theta_r \\ 0 & 0 & 0 \end{pmatrix}$, and B = $\begin{pmatrix} cos\theta_r & 0 \\ sin\theta_r & 0 \\ 0 & 1 \end{pmatrix}$.

To apply the linearization error model to the MPC controller, discretization processing is performed by the forward Euler method [22] to obtain the linear error discretization model of the system, as shown in the following equation:

$$\begin{cases} \tilde{\chi}(k+1) = A_{k,t}\tilde{\chi}(k) + B_{k,t}\tilde{u}(k) \\ y(k) = C_{k,t}\tilde{\chi}(k) \end{cases} \tag{6}$$

where $A_{k,t} = \begin{pmatrix} 1 & 0 & -v_r \sin\theta_r \cdot T \\ 0 & 1 & v_r \cos\theta_r \cdot T \\ 0 & 0 & 1 \end{pmatrix}$, $B_{k,t} = \begin{pmatrix} \cos\theta_r \cdot T & 0 \\ \sin\theta_r \cdot T & 0 \\ 0 & T \end{pmatrix}$, $C_{k,t} = \begin{pmatrix} 1 & 0 & 0 \\ 0 & 1 & 0 \\ 0 & 0 & 1 \end{pmatrix}$, and T is the sampling time.

3.2.2. Design of the Objective Function and Constraint Conditions

To prevent the control variables in the system from experiencing sudden changes, which may lead to decreases in the path-tracking accuracy and system stability of the lawn mower, control increments are used to replace the control variables. The modified state equation is as follows:

$$\xi(k|t) = \begin{pmatrix} \tilde{\chi}(k|t) \\ \tilde{u}(k-1|t) \end{pmatrix} \tag{7}$$

Therefore, the output state quantity of the system can be expressed as follows:

$$\eta(k) = \tilde{c}_{k,t}\xi(k|t) \tag{8}$$

where $\eta(x, y, \theta)^T$ represents the output of the discrete MPC system, x represents the horizontal axis position of the lawn mower, y represents the vertical axis position (m) of the lawn mower, and θ represents the heading angle of the lawn mower in degrees.

After modification, the state equation used for the MPC controller is represented as follows:

$$\begin{cases} \xi(k+1) = \tilde{A}\xi(k) + \tilde{B}\Delta u(k) \\ \eta(k) = \tilde{c}_{k,t}\xi(k|t) \end{cases} \tag{9}$$

where $\Delta u(k) = \tilde{u}(k) - \tilde{u}(k-1)$, $\tilde{A}_{k,t} = \begin{pmatrix} A_{k,t} & B_{k,t} \\ 0_{m\times n} & I_m \end{pmatrix}$, $\tilde{B}_{k,t} = \begin{pmatrix} B_{k,t} \\ I_m \end{pmatrix}$, $\tilde{c}_{k,t} = \begin{bmatrix} k_1 & 0 & 0 & 0 & 0 \\ 0 & k_2 & 0 & 0 & 0 \\ 0 & 0 & k_3 & 0 & 0 \end{bmatrix}$, and n represents the dimensionality of the system state variable. In this article, n is equal to 3, m is the dimensionality of the control variable, and m is 2. $k_1, k_2,$ and k_3 are the weight ratios of the three state variables' errors.

The modified state prediction equation is iteratively derived, and the system's prediction output is set as follows:

$$Y(k+1|k) = f_{\xi}\xi(k) + f_u\Delta U(k) \tag{10}$$

where Y is the output matrix of the system, ΔU is the control increment matrix, f_{ξ} and f_u are the iterative matrices of the equation, $Y(k+1|k) = \begin{bmatrix} \eta(k+1|k) \\ \eta(k+2|k) \\ \cdots \\ \eta(k+N_p|k) \end{bmatrix}$, $f_{\xi} = \begin{bmatrix} \tilde{C}_k\tilde{A}_k \\ \tilde{C}_k\tilde{A}_k^2 \\ \cdots \\ \tilde{C}_k\tilde{A}_k^{N_p} \end{bmatrix}$, $\Delta U(k) = \begin{bmatrix} \Delta u(k|k) \\ \Delta u(k+1|k) \\ \cdots \\ \Delta u(k+N_c|k) \end{bmatrix}$, and $f_u = \begin{bmatrix} \tilde{C}_k\tilde{B}_k & 0 & \cdots & 0 \\ \tilde{C}_k\tilde{A}_k\tilde{B}_k & \tilde{C}_k\tilde{B}_k & \cdots & 0 \\ \vdots & \vdots & \ddots & \vdots \\ \tilde{C}_k\tilde{A}_k^{N_p-1}\tilde{B}_k & \tilde{C}_k\tilde{A}_k^{N_p-2}\tilde{B}_k & \cdots & \tilde{C}_k\tilde{A}_k^{N_p-N_c-1}\tilde{B}_k \end{bmatrix}$.

Considering the actual working situation of the lawn mower, when designing the MPC controller, the control quantity and control increment constraints are considered, which is beneficial for improving the path-tracking accuracy of the lawn mower. The design of the objective function mainly revolves around the deviation of the system state variables and the constraints of the control variables during the operation of the lawn mower. A multi-objective optimization function is designed with constraints based on the control objective proposed earlier, and the objective function for the control is predicted using the following model form:

$$J(k) = \sum_{i=1}^{N_p} ||\ \eta(k+i\mid k) - \eta_{ref}(k+i\mid k)||_{Q}^{2} + \sum_{i=1}^{N_c-1} ||\ \Delta U(k+i\mid k)\ ||_{R}^{2} + \rho\varepsilon^2 \tag{11}$$

where N_p is the predictive time domain; N_c is the control time domain; ΔU is the control increment in the control time domain; ε is the relaxation factor; Q is the weight matrix of the output quantity; R is the weight matrix of the control increment; ρ is the weight matrix of the relaxation factor; $\eta_{\text{ref}}(X_{\text{ref}}, Y_{\text{ref}}, \theta_{\text{ref}})$ is the reference output variable; and η_{ref} is the global reference path for the working environment of the lawn mower.

To prevent the problem of variables being unsolvable during the solving process, a relaxation factor, ε, and a weight matrix representing the relaxation factor, ρ, need to be added. In the objective function, it is necessary to calculate the output of the system in the predicted time domain.

In the optimization objective function, the solution is the control time domain. The control increment within N_c can only appear in the form of a control increment or its multiplication with the transformation matrix with the constraint conditions applied. Therefore, it is necessary to transform the control increment constraint inequality and obtain the corresponding transformation matrix.

$$U_{\min} \leq U_t + A\Delta U_t \leq U_{\max} \tag{12}$$

$$A = \begin{bmatrix} 1 & 0 & \cdots & \cdots & 0 \\ 1 & 1 & 0 & \cdots & 0 \\ 1 & 1 & 1 & \ddots & 0 \\ \vdots & \vdots & \ddots & \ddots & \vdots \\ 1 & 1 & \cdots & 1 & 1 \end{bmatrix} \tag{13}$$

In the formula, $U_{\max}$ and $U_{\min}$ refer to the control time domain. The sum of the maximum and minimum values of the control variables is within N_c; A is the coefficient matrix, and $A \otimes I_m$. Here, $\otimes$ is the Kronecker product, and I_m is the m-dimensional identity matrix.

In the model predictive control system proposed in this article, constraints can be set to better reflect physical facts, and MPC has the advantage of allowing its constraints to be modified online, whereas other optimization methods do not. According to the principles of control algorithms and the physical structure of the chassis, the constraints in this article mainly include the control limit constraints and control increment constraints during the control process. The constraint conditions are as follows [3]:

$$u_i(k+j) \leq u(k+j) \leq u_a(k+j), j = 0, 1., N_c - 1 \tag{14}$$

$$\Delta u_i(k+j) \leq \Delta u(k+j) \leq \Delta u_a(k+j), j = 0, 1., N_c - 1 \tag{15}$$

where u_i and u_a represent the minimum and maximum values of the control variables, respectively, and Δu_i and Δu_a represent the minimum and maximum values of the control increment, respectively.

3.2.3. Optimization Problem-Solving

To solve the above optimization problem by using quadratic programming, it is necessary to convert the objective function into the following standard form:

$$minJ = \frac{1}{2} Z^T Q Z + C^T Z \tag{16}$$

After integrating the objective function and constraints, the controller needs to output control sequences to the system during each control cycle, convert the objective function into a standard quadratic form, and incorporate the constraints to solve the following optimization problems:

$$J(\xi(k), u(k-1), \Delta U(k)) = \left[\Delta Uk\right]^T, \varepsilon^T H_k \left[\Delta U(k)^T, \varepsilon\right] + G_k [\Delta U(k)^t, \varepsilon\right] \tag{17}$$

$$s.t. \Delta U_{\min} \leq \Delta U(k) \leq \Delta U_{\max} \tag{18}$$

$$U_{\min} \leq U_t + A \Delta U(k) \leq U_{\max} \tag{19}$$

where $H_k = \begin{pmatrix} f_{uk}^T Q f_{uk}^T & 0 \\ 0 & \rho \end{pmatrix}$, $G_k = \begin{bmatrix} 2E(k)^T Q f_{uk} & 0 \end{bmatrix}$, and $E(k)$ denotes the tracking errors in the predicted time domain.

The system solves the standard quadratic form combined with constraints in each control cycle and obtains the control sequence in the control time domain. According to the basic theory of MPC, the first element, $\Delta u(k)$, in the control sequence is applied to the system as the actual control quantity, as shown in Equation (20):

$$\tilde{u}(k) = \tilde{u}(k-1) + \Delta u(k) \tag{20}$$

When the system repeats the above optimization process after each control cycle until the entire control process is completed, tracking control is achieved for the reference path of the mowing robot.

3.2.4. Adaptive Time Domain Module Design

The time-domain parameters of model predictive control have a significant impact on the control effect, but fixed parameters have poor adaptability to complex operating conditions and cannot adapt to the environment in real time. Among them, the two parameters with the most significant impacts are the control time domain and the prediction time domain.

As shown in Figure 4, when the other control parameters remain unchanged, the larger the prediction time domain is, the larger the range predicted by the controller, which can obtain more lawn mower state information. However, if the prediction time domain is too large, it will increase the error of the lawn mower at a distant position, thereby reducing the tracking accuracy of the lawn mower at a nearby position [23]. In addition, an excessively large prediction time domain will also increase the computational complexity of the MPC algorithm and reduce the real-time performance of the system [24]. When the prediction time domain is too small, the status information of the lawn mower will decrease. In the presence of system control constraints, the lawn mower will be unable to turn in a timely manner, the path-tracking accuracy will be reduced, and stability will not be ensured.

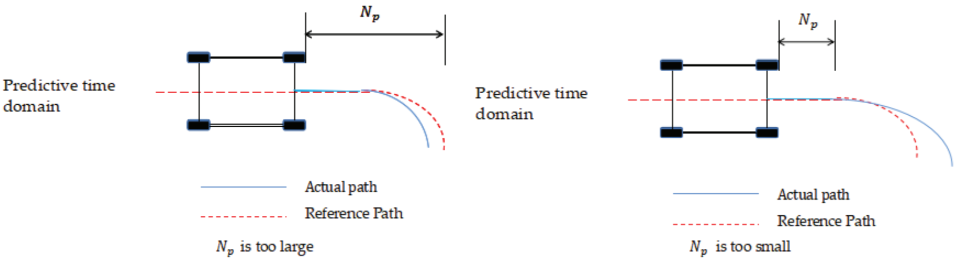

Figure 4. Analysis of the impact under different N_p conditions.

Based on the model predictive controller set above, in this section, a control time domain and prediction time domain optimization module is designed based on the vehicle's speed, as shown in Figure 5, to achieve adaptive parameter adjustment, improve the adaptability of the mower to environmental changes, and improve the path-tracking accuracy of the mower.

As the vehicle speed increases, the distance predicted by the MPC controller also needs to increase accordingly; that is, the predicted time domain, N_p, increases accordingly to ensure the stable tracking of the reference path by the lawn mower and to avoid the untimely turning phenomenon. For the control time domain, N_c, an increase in N_c can reduce the degree of sudden change in the control quantity and prevent the vehicle from slipping or even losing control during high-speed driving [25]. Therefore, the control time domain should also increase appropriately with increasing vehicle speed to ensure the stability of path tracking.

As shown in the Figure 5, a time domain optimization module based on vehicle speed is designed using a fuzzy control algorithm. The design input is the current speed of the lawn mower, and the predicted time domain is the output. Based on the motor performance of the lawn mower, the input walking speed range of the lawn mower is determined to be [0, 0.8 m/s], and the adaptive predicted time domain value range for the reference path combined with the control algorithm is [10, 30].

The speed and prediction time domain of the lawn mower is divided into the following seven fuzzy subsets: NB (very small), NM (small), NS (small), Z (moderate), PS (large), PM (large), and PB (large). The membership function selects the Gaussian and trigonometric functions.

Based on the time domain optimization design and multiple simulation experiments, specific fuzzy rules are formulated, as shown in Table 2. The response relationship between the operating speed of the lawn mower and the predicted time domain is shown in Figure 6. The operating speed of the lawn mower is obtained through fuzzy inference to determine the predicted fuzzy output in the time domain. The centroid method is selected to solve the ambiguity of this problem and obtain an accurate output prediction in the time domain.

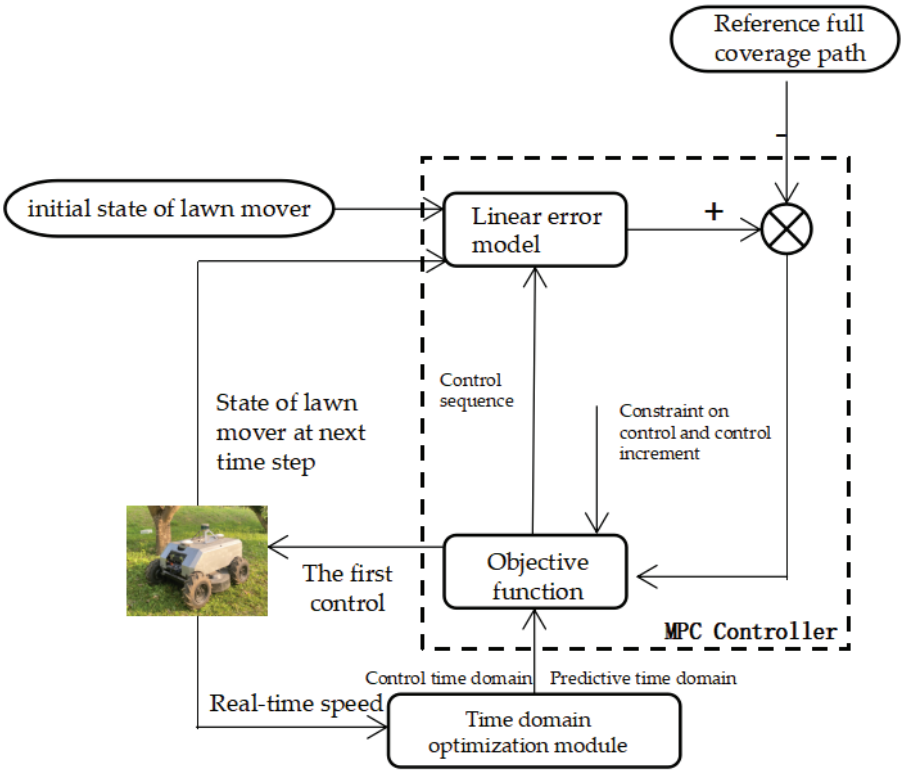

Figure 5. Block diagram of the adaptive time domain MPC path-tracking control process.

Table 2. Fuzzy rule table.

Fuzzy Quantity	Fuzzy Subset
v	NB NM NS Z PS PM PB
Np	NB NM NM Z PM PB PB

where *v* is the speed of the lawn mower, *Np* is the predicted time domain.

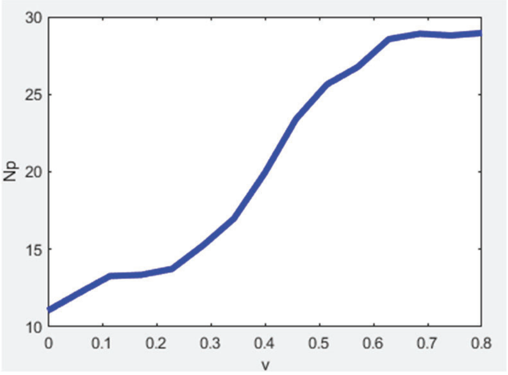

Figure 6. Response graph for the speed and prediction time domain.

The prediction time domain output is smoothed by the fuzzy algorithm to obtain the current optimal prediction time domain, N_{pb}, after fuzzy processing. The current optimal prediction time domain is appropriately adjusted to obtain the current optimal control time domain, N_{cb}. The expressions for N_{pb} and N_{cb} are as follows:

$$N_{pb} = Round(N_p) \tag{21}$$

$$N_{cb} = Round\ (\alpha * N_p) \tag{22}$$

In the above equation, α is a time domain weight parameter, which usually ranges from 0.15 to 0.2. Here, based on the simulation situation, the time domain weight coefficient is selected as 0.2.

3.3. Mower Driving Wheel Anti-Slip Control Based on Fuzzy Slip Rate Control

The driving wheel of a lawn mower may experience significant longitudinal slippage in complex operating environments, which can affect the path-tracking accuracy and stable operation of the mower. Therefore, it is necessary to consider the impact of driving wheel slippage on path-tracking accuracy.

3.3.1. Establishing a Dynamic Model for the Driving Wheel of a Mower

To analyze the state of the driving wheel of a lawn mower, a dynamic model is established; interference such as air resistance is ignored, as shown in Figure 7.

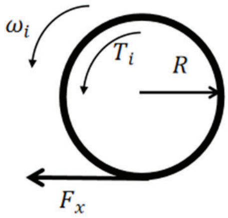

Figure 7. Dynamic model of the driving wheel of a lawn mower.

The dynamic equation for the driving force of the lawn mower is established as shown in Equation (22):

$$J\dot{\omega} = T_i - RF_x - T_x \tag{23}$$

Therefore, the torque of the driving wheel of the lawn mower can be expressed as follows:

$$T_i = J\dot{\omega} + RF_x + T_x \tag{24}$$

The rotational inertia of the driving wheel can be expressed as follows:

$$J = \frac{MR^2}{2} \tag{25}$$

where J is the moment of inertia (kg/m^2), ω is the angular acceleration of the driving wheel (rad/s^2), T_i is the torque of the driving wheel (N·m), R is the radius of the driving wheel (m), F_x is the longitudinal driving force of the tire (N), T_x is the rolling resistance moment (N·m), and M is the mass of the lawn mower (kg).

In this article, the standard Pacejka magic equation is used. The H.B. Pacejka tire model is an empirical model that fits actual test data. Its form is universal and can simultaneously describe the relationships between the longitudinal force of the tire and the longitudinal slip rate, the lateral force and the lateral tire angle, the return torque and the lateral tire angle, and the vertical wheel load. Moreover, its fitting accuracy is high, so it is called the "magic formula". The magic formula includes the longitudinal tire force under single driving or braking conditions, the lateral tire force under single steering conditions, and the longitudinal tire force and the lateral force under combined drive/braking conditions [26,27].

Under a single driving/braking condition, the relationship between the longitudinal tire force, longitudinal slip rate, and vertical tire load can be described as follows:

$$F_{x0} = D_1 sin\{C_1 arctan[B_1\lambda - E_1(B_1\lambda - arctan B_1\lambda)]\} \tag{26}$$

where the curve form factor is C_1 = 1.65, the peak factor is $D_1 = a_1{F_z}^2 + a_2F_z$, $B_1C_1D_1 = \left(a_3{F_z}^2 + a_4F_z\right)e^{-a_5F_z}$, the stiffness factor is $B_1 = \frac{B_1C_1D_1}{C_1D_1}$, the curvature factor of the curve is $E_1 = a_6{F_z}^2 + a_7F_z + a_8$, λ is the longitudinal slip rate, and a_i is the fitting coefficient.

Under pure steering conditions, the relationship between the longitudinal tire force, F_{y0}; the tire side deflection angle, α; and the vertical tire load, F_z, can be described as follows:

$$F_{y0} = D_2sin\{C_2arctan[B_2x - E_2(B_2x - arctanB_2x)]\} \tag{27}$$

$$x = \alpha + S_h \tag{28}$$

where the curve form factor is C_2 = 1.3; the peak factor is $D_2 = a_1{F_z}^2 + a_2F_z$; $B_2C_2D_2 = a_3 sin[a_4arctan(a_5F_z)](1 - a_{12}|\gamma|)$; the stiffness factor is $B_2 = \frac{B_2C_2D_2}{C_2D_2}$; the horizontal drift of the curve is $S_h = a_9\gamma$; the vertical drift of the curve is $S_v = (a_{10}{F_z}^2 + a_{11}F_z)\gamma$; the curvature factor of the curve is $E_2 = a_6{F_z}^2 + a_7F_z + a_8$; α is the tire sideslip angle; and γ is the wheel camber angle [28].

The relationship between the longitudinal tire force, F_x, and lateral force, F_y, under the combined driving/braking and steering conditions, as well as the lateral tire slip angle, α, and longitudinal slip rate, λ, is as follows:

$$F_x = \frac{\sigma_x}{\sigma}F_{x0},\ F_y = \frac{\sigma_y}{\sigma}F_{y0} \tag{29}$$

where $\sigma = \sqrt{{\sigma_x}^2 + {\sigma_y}^2}, \sigma_x = -\frac{\lambda}{1+\lambda}, \sigma_y = -\frac{tan\alpha}{1+\lambda}$.

By referring to the traditional tire model and the attributes of the lawn mower itself, the above values can be assigned to determine the relationship between the longitudinal and lateral forces of the tire and the slip rate, as shown in Figure 8.

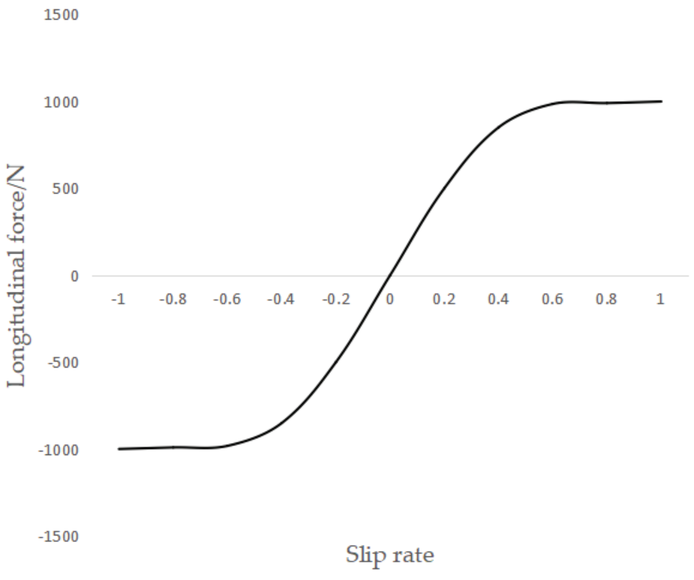

Figure 8. Diagram of the relationship between the longitudinal force and the slip rate.

3.3.2. Target Slip Rate Range of Lawn-Mowing Robots

The slip rate of the driving wheel is defined as the relative error between the wheel speed of the driving wheel and the absolute speed of the vehicle body [29]. In this article, the rotational speed data of the driving wheel are collected under the working condition of the lawn mower through pre-experiments, the real-time slip rate of the lawn mower during a certain working cycle is calculated according to Equation (29), and the target slip rate of the driving wheel is analyzed based on this. In general, whether wheel slippage occurs is measured by the slip rate of the driving wheel. This article uses the following slip rate expression:

$$s = \frac{\omega r - v}{\max(\omega r, v)} \tag{30}$$

where ω is the angular velocity of rotation; v is the moving speed of the lawn mower; and R is the wheel radius. In this article, the radii of all wheels are assumed to be equal.

According to the design of the slip rate measurement experiment in Section 2.2.1, the lawn mower is controlled to perform repeated working experiments on the working path, recording the real-time speed and motor-related parameters of the lawn mower on this working path. The real-time slip rate of the lawn mower is calculated according to Equation (29), and the relationships between the motor parameters and slip rate are analyzed, as shown in the following figures.

Because of the use of a hub motor in the lawn mower in this article, the performance parameters of the motor can better reflect the states of the driving wheels. Based on the real-time speeds of the four driving wheel motors during the experiment, the effective output power and slip rate data of the motor are analyzed. From Figure 9, it can be observed that, when the slip rate is maintained within 0–0.2, the speed of the drive wheel motor is relatively stable, and the observed changes are roughly linear. When the slip rate exceeds 0.4, the speed of the drive wheel motor rapidly increases until the slip rate reaches approximately 0.9, and the motor speed of the drive wheel approaches the maximum speed. At this point, it can be determined that the drive wheel is idling. As shown in Figure 10, when the slip rate of the driving wheel is maintained below 0.2, the effective output power of the driving wheel motor remains in its optimal state. When the slip rate reaches approximately 0.9, the effective power of the driving wheel motor approaches 0, and at this time, the motor is not in operation, and the driving wheel is in an idle state. Based on the above analysis, the target slip rate in this article is not fixed to a certain value. The aim of the value condition is to first ensure that no slip occurs; that is, the target slip rate should be controlled within [−0.2, 0.2]. If it exceeds this range, the slip rate is controlled by a fuzzy controller to force it to lie within this range.

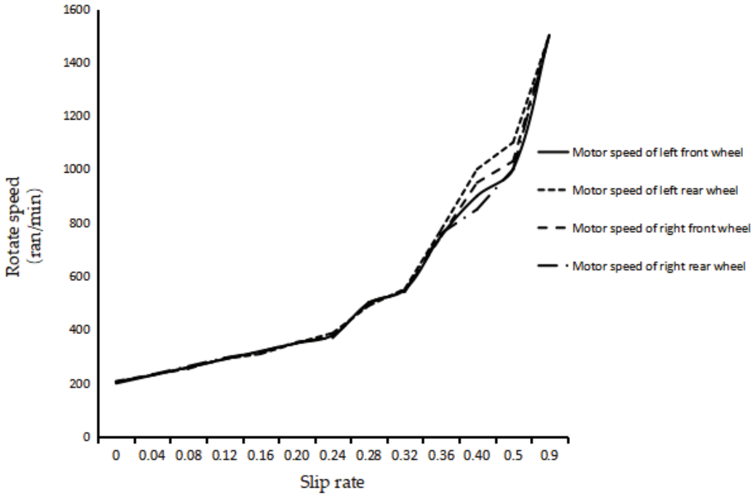

Figure 9. Relationship between the slip rate and real-time speed of the driving wheel.

3.3.3. Fuzzy Controller Design Considering the Slip Rate

This article adopts a dual-input single-output fuzzy control algorithm, where the inputs are the expected speed of the driving wheel obtained by the MPC controller and the real-time speed of the mower, and the output is the expected slip rate of the driving wheel of the mower. Based on the real-time vehicle speed feedback obtained from the lawn mower and the expected wheel speed of the MPC controller; the driving speed range of the lawn mower is set to [−0.8 m/s, 0.8 m/s]; the real-time speed range of the driving wheel is set to [−5 rad/s, 5 rad/s]; and according to the previous analysis, the expected slip rate range is set to [−0.2, 0.2].

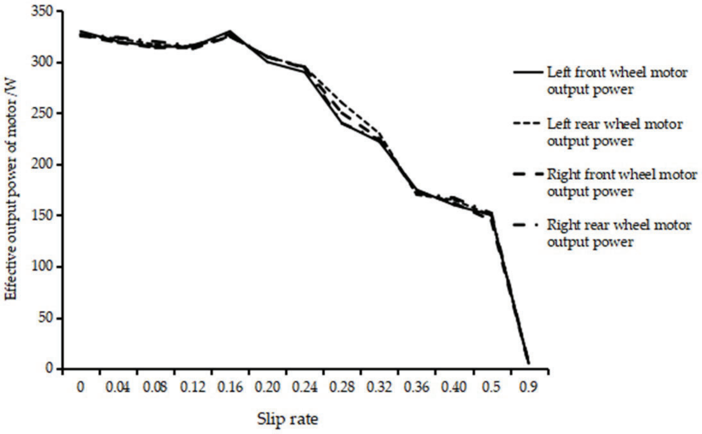

Figure 10. Diagram of the relationship between the slip rate and the effective output power of the drive wheel motor.

The reference speed, real-time drive wheel speed, and expected slip rate of the lawn mower are divided into the following seven fuzzy subsets: NB (very small), NM (small), NS (small), Z (moderate), PS (large), PM (large), and PB (large). In terms of membership function selection, the system adopts the combination of a Gaussian function and a trigonometric function, which not only ensures that the system has high sensitivity but also makes the system more stable.

Based on the relationships between the slip rate, vehicle speed, and driving wheel speed and after conducting many simulation experiments, the most common If–Then rule in fuzzy control is adopted. Specific fuzzy rules are formulated, as shown in Table 3. The response relationship between the reference speed of the lawn mower, the speed of the driving wheel, and the expected slip rate is shown in Figure 11. When one of the indicators of driving wheel speed and real-time speed changes, or both changes, the slip rate will be affected.

Table 3. Table of fuzzy slip rate control rules.

ω	v						
	NB	**NM**	**NS**	**Z**	**PS**	**PM**	**PB**
NB	Z	PB	PM	PM	PS	Z	Z
NM	PM	Z	PM	PS	PS	Z	NS
NS	PM	PM	Z	PS	Z	NS	NS
Z	NS	PM	PS	Z	NS	NM	NM
PS	NM	PS	NM	NS	Z	NM	NM
PM	NM	Z	NM	NM	NM	Z	NB
PB	NB	Z	NB	NM	NM	NB	Z

The reference driving wheel speed of the MPC controller and the speed of the lawn mower are input through fuzzy inference to obtain the fuzzy output. The centroid method is chosen to solve the ambiguity and obtain an accurate expected slip rate output.

This article adopts the classic incremental PID control method [30] for the design of the slip rate PID controller, whose expression is as follows:

$$u_s(k) = K_{ps} * e_s(k-1) + K_{is} * e_s(k) + K_{ds} * (e_s(k) - 2e_s(k-1) + e_s(k-2)) + u_s(k-1) \tag{31}$$

In the equation, $u_s(k)$ is the slip rate output by the lawn mower at this time, and $u_s(k-1)$ is the last output quantity.

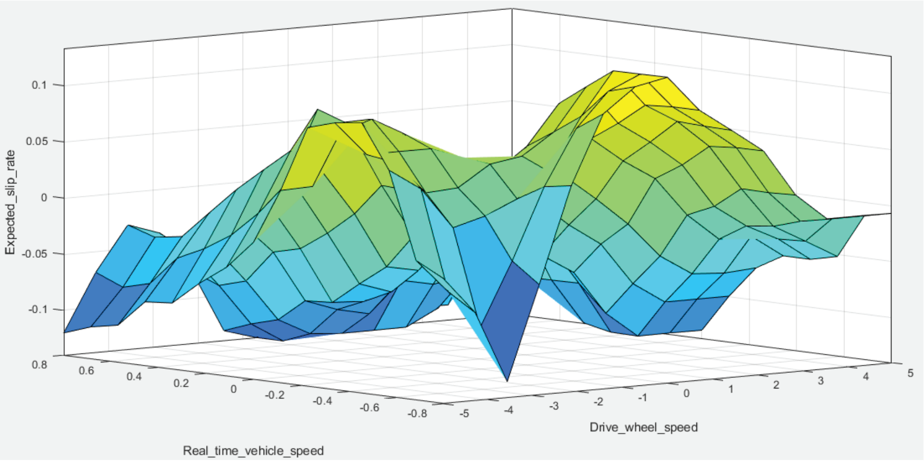

Figure 11. Diagram of the relationship between the driving wheel speed, real-time vehicle speed, and expected slip rate.

For the PID controller applied to the motor torque, incremental PID control is also used, and its expression is as follows:

$$u_v(k) = K_{pv} * e_v(k-1) + K_{iv} * e_v(k) + K_{dv} * (e_v(k) - 2e_v(k-1) + e_v(k-2)) + u_v(k-1) \tag{32}$$

In the equation, $u_v(k)$ is the current torque output by the drive motor of the lawn mower, and $u_v(k-1)$ is the last output quantity. The slip rate and driving wheel torque of the PID controller are shown in Figure 12:

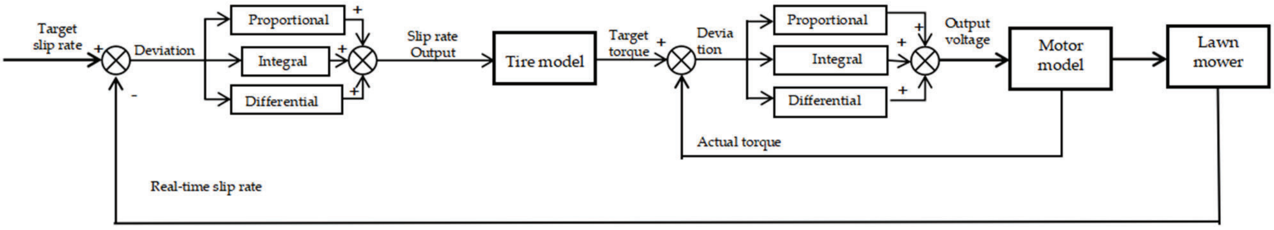

Figure 12. Incremental PID control chart for the slip rate and driving wheel torque.

Based on many simulation experiments and field experiments, the PID controller parameter values are set as shown in Table 4.

Table 4. Table of fuzzy slip rate control rules.

PID Controller Parameters	Value
Dwelling time/s	0.02
Proportional slip rate control	3
Integral slip rate control	1
Differential slip rate control	0.6
Proportional drive wheel motor speed control	5
Integral drive wheel motor speed control	1.6
Differential drive wheel motor speed control	0.8

In summary, the fuzzy control algorithm can obtain the expected slip rate of the driving wheel based on the fuzzy rule table formulated by the fuzzy controller, the target speed of the driving wheel obtained by the MPC controller, and the real-time speed fed back from the lawn mower. The PID controller of the slip rate is designed to control the expected slip rate obtained by the fuzzy controller and the actual measured slip rate and obtain the output slip rate of the driving wheel. By combining the dynamic model of the lawn mower with a torque PID controller, the torque of the motor is controlled to achieve anti-slip control for the lawn mower.

3.4. Path-Tracking Controller for Designing Adaptive MPC and Fuzzy Slip Rate Control Schemes

The path-tracking controller based on MPC and fuzzy control performs anti-slip control for the lawn mower by controlling the slip rate and torque of the driving wheels. The concrete implementation steps are shown in Figure 13. First, a dynamic model for the driving wheel of the lawn mower is established, the relationship between the slip rate and road adhesion coefficient is analyzed through the dynamic model, and the range of slip rates at which the driving wheel does not slip is obtained. Based on the MPC controller output of Section 3.2, the linear speed and angular velocity of the vehicle are obtained, and the expected driving wheel speed is determined through the use of a four-wheel differential steering model. Then, the expected slip rate is calculated by the real-time vehicle speed feedback derived from the actual process. If the observed rate is within the nonslip range, it is considered the target slip rate. If it exceeds the range, it is input into the established fuzzy controller to control the slip rate within a moderate range and output the target slip rate. A slip rate PID controller that outputs the target speed through real-time slip rate feedback obtained from the actual process to control the slip rate of the driving wheel near the target slip rate is designed. The target speed of the driving wheel obtained from the previous step is calculated with the target speed obtained from the MPC; it is converted into the final output slip rate, and the tire dynamics model is used for verification purposes. The real-time steering angle speed feedback from the actual process is used to obtain the lateral wheel angle. The slip rate, lateral angle, and vertical wheel load are substituted into the magic equation under the longitudinal and lateral joint working conditions to obtain the longitudinal force acting on the wheel, thereby obtaining the output torque of the target motor. A torque PID controller that combines real-time torque feedback from the motor with the output voltage is designed to control the torque. Finally, the torque output by the motor is input into the actual process, which can ensure that the wheel slip rate is within the nonslip range, guaranteeing that the driving wheel is in a better working state and achieving anti-slip control of the lawn mower driving wheel. The overall control diagram is as follows.

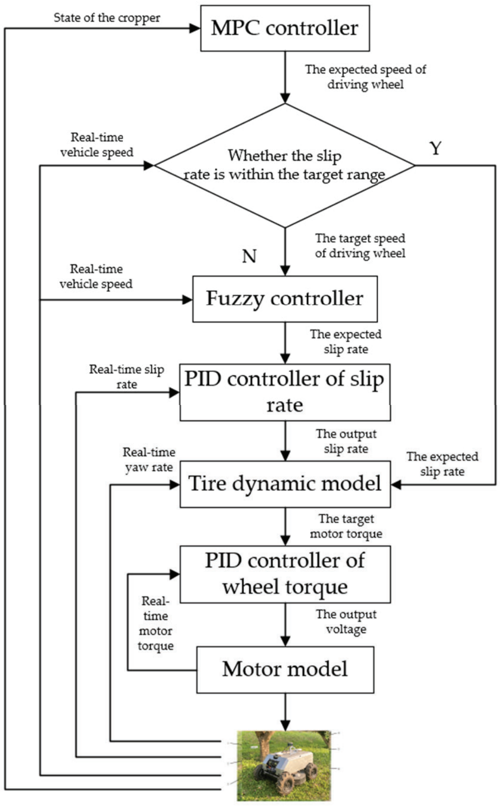

Figure 13. Path-tracking control system diagram for lawn mowers.

4. Results and Discussion

4.1. Path-Tracking Simulation

4.1.1. Adaptive MPC-Based Path-Tracking Simulation

An adaptive path-tracking simulation platform is built for lawn mowers based on MATLAB/Adams, and a flat road with an unchanged road adhesion coefficient is set in Adams. The path is a looping curve, and the MPC controller is implemented through S-FUSION. It can dynamically describe system changes and achieve variable conversion based on real-time system changes. The main simulation control diagram is shown in Figure 14.

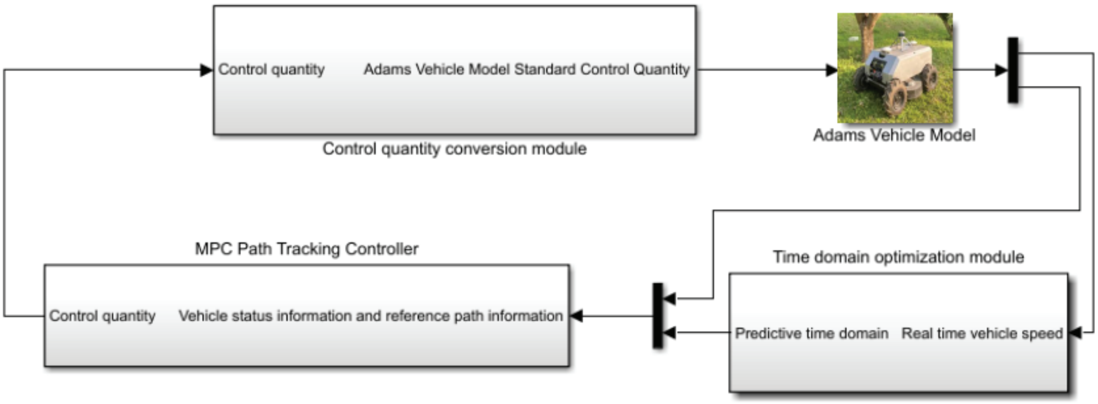

Figure 14. Structure diagram of the adaptive MPC simulation system.

The purpose of the controller is to accurately and quickly track the reference path while minimizing deviations and maintaining tracking stability during the tracking process. According to the controller design mentioned above, path-tracking control is performed by setting a fixed time domain parameter control group and a model predictive controller in the adaptive time domain for double-shift simulation experiments and loop path simulation experiments. The predicted time domain, *Np*, of the fixed time domain parameter control group is 15, and the control time domain, *Nc*, is 3. The constraints of the control quantity and control increment are shown in Equation (32), and the basic parameters of the model predictive controller are shown in Table 5.

$$\begin{cases} -0.8\ \text{m/s} \le v \le 0.8\ \text{m/s} \\ -0.2\ \text{rad/s} \le \omega \le 0.2\ \text{rad/s} \end{cases}, \begin{cases} -0.1\ \text{m/s} \le \Delta v \le 0.1\ \text{m/s} \\ -0.04\ \text{rad/s} \le \Delta\omega \le 0.04\ \text{rad/s} \end{cases} \tag{33}$$

Table 5. MPC controller parameter table.

Basic Parameters of the Model Predictive Controller	Numerical Value
Sampling time (s)	0.2
Reference speed (m/s)	0.6
Relaxation factor weight coefficient	10
Relaxation factor, ε	10
Weight matrix, Q	$\begin{bmatrix} 10 & \cdots & 0 \\ \vdots & \ddots & \vdots \\ 0 & \cdots & 10 \end{bmatrix}_{3N_p}$
Weight matrix, R	$\begin{bmatrix} 1 & \cdots & 0 \\ \vdots & \ddots & \vdots \\ 0 & \cdots & 1 \end{bmatrix}_{2N_c}$

The reference path is set to a looping path, and the simulation results are shown in Figure 15, and the relevant data are shown in Table 6. From the path-tracking effect, it can be seen that the fixed time domain controller does not fit the reference path as well as the adaptive time domain controller at turns. From Figures 16 and 17, it can be concluded that the absolute value of the maximum lateral error in the fixed time domain is 0.13 m, the average value of the lateral error is 0.075 m, the absolute value of the maximum longitudinal error is 0.135 m, and the average value of the longitudinal error is 0.058 m. The absolute value of the maximum horizontal error in the adaptive time domain is 0.115 m, the average horizontal error is 0.043 m, the absolute value of the maximum vertical error is 0.085 m, and the average vertical error is 0.041 m. From the lateral and vertical deviations of the path, it can be observed that whether a fixed time domain or an adaptive time domain is utilized, the error is larger in places with larger turning angles. Overall, the adaptive time domain has a better effect on path tracking, with smaller errors.

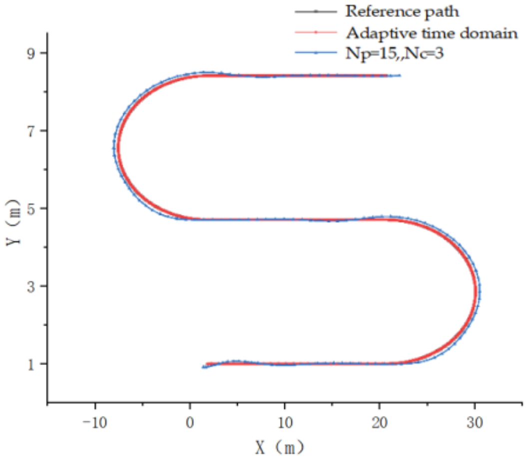

Figure 15. Effect diagram of looping path tracking.

Table 6. Comparison between the controller parameters of the fixed time domain and adaptive time domain.

Time Domain Parameters	$N_p = 15$ $N_c = 3$	Adaptive Time Domain Parameters
Absolute value of the maximum lateral error (m)	0.13	0.115
Average lateral error (m)	0.075	0.043
Absolute value of the maximum longitudinal error (m)	0.135	0.085
Mean value of the longitudinal error (m)	0.058	0.041

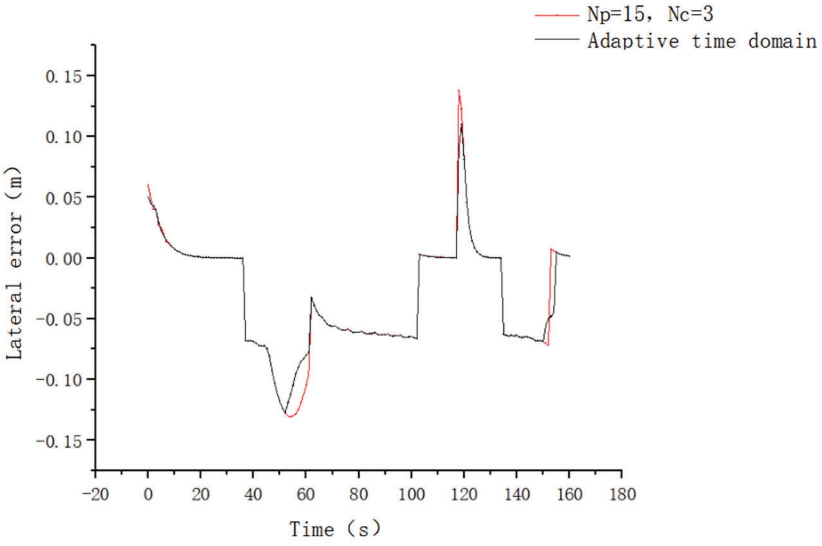

Figure 16. Lateral error results of the path simulation.

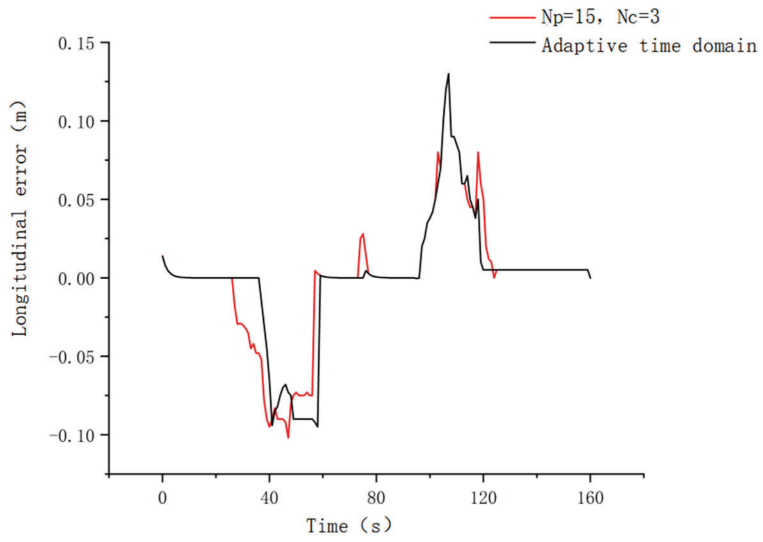

Figure 17. Longitudinal error results of the path simulation.

In summary, the adaptive time domain-based MPC controller performs better in terms of tracking the looping path than the fixed time domain-based MPC controller and can adapt to complex orchard environments.

4.1.2. Simulation Experiment Involving the Path-Tracking Controller Combined with Anti-Slip Drive Control

A predictive controller and a fuzzy controller are built for the slip rate of a lawn mower model based on MATLAB, and a joint simulation is conducted with the wheel mower model built using Adams. The simulation structure is shown in Figure 18.

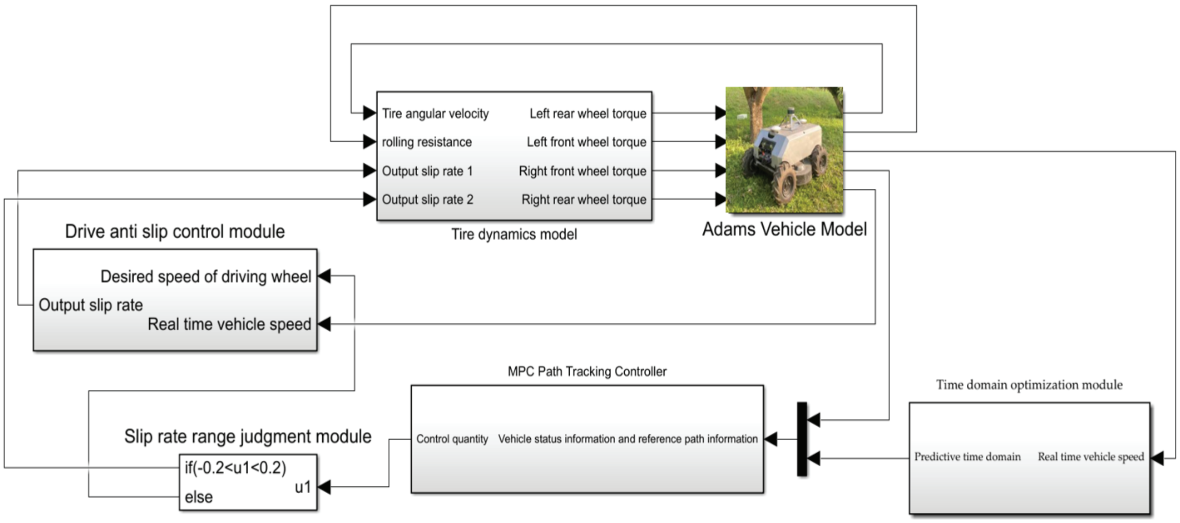

Figure 18. Simulation structure diagram of the combined anti-slip drive control and path-tracking control method.

Based on Adams' random road surface design with varying road coefficients and reference paths, comparative simulation experiments are conducted on the path-tracking controller combined with anti-slip driving control and the MPC path-tracking control approach designed in this paper. Figures 19 and 20 show the slip rate variation curves of the front-left drive wheel and the front-right drive wheel, respectively. Figures 19 and 20 show that, during the operation of the lawn mower, because of changes in the road adhesion coefficient, the longitudinal driving force of the lawn mower is inconsistent, and the driving wheel experiences significant sliding. After adding a fuzzy controller based on the slip rate, the slip rate of the lawn mower can be effectively controlled within the target slip rate range, indicating that, within this reference path and these road conditions, the slip rate of the driving wheel remains in a relatively good state, and the speed variation of the driving wheel is not high, resulting in good working performance. When the MPC controller without added anti-slip driving tracks the reference path, because of the change in the road adhesion coefficient, the slip rate changes significantly, with a maximum value close to 0.6. At this time, the lawn mower seriously slips, which has a significant impact on the resulting path-tracking accuracy. Therefore, the addition of a path-tracking controller with anti-slip driving ability has the effect of suppressing slip, and the path-tracking effect is better.

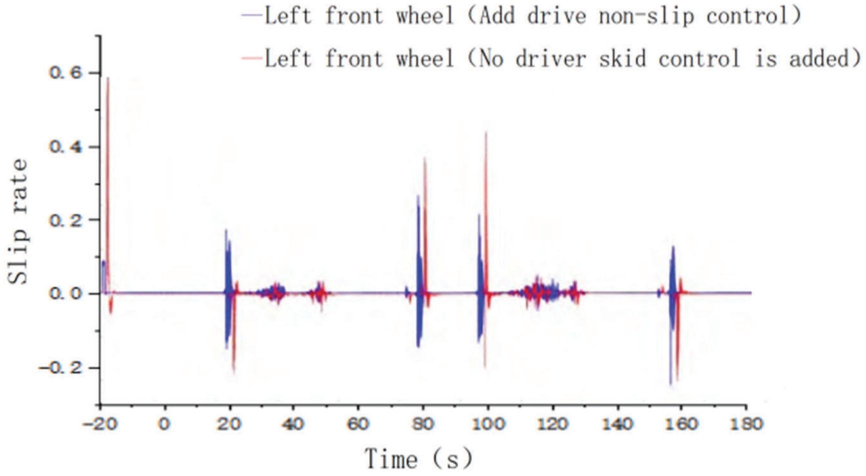

Figure 19. Comparison diagram concerning the slip rate of the left front wheel of the lawn mower.

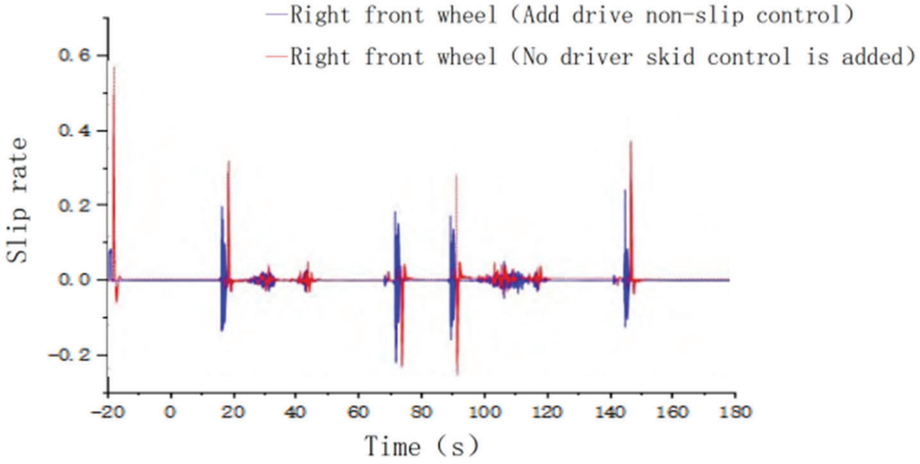

Figure 20. Comparison involving the slip rate of the right front wheel of the lawn mower.

As shown in Figure 21, compared with traditional MPC control, the MPC-based path-tracking controller with added anti-slip drive control fits the reference path better and can also effectively track the reference path in areas with larger turns.

4.2. Field Trial Verification

Utilizing the lawn-mowing robot platform built in Section 2.1, the fixed reference path set in Figure 2 is determined through the pre-experimental collection, and path-tracking control and anti-slip driving control experiments are performed for verification purposes. The upper computer automatically saves the lateral deviation data and the slip rate data of the driving wheels during the lawn mower working process and conducts statistical analyses on the data. The comparative effects of the slip rates of the four driving wheels and the lateral and longitudinal path-tracking deviations are shown in the figure. For the convenience of analysis, the slip rate is taken as an absolute value.

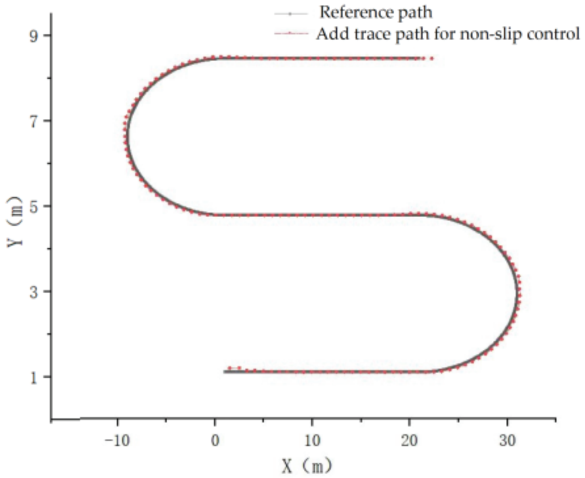

Figure 21. Diagram comparing the actual path and reference path under anti-slip drive control.

As shown in Figures 22–25, without the addition of an anti-slip drive controller, the amplitude of the slip rate change curve of the lawn mower is relatively large when driving on the reference path, with an amplitude of approximately 0.5. At this point, the different driving wheels experience varying degrees of slipping, seriously affecting the path-tracking effect. After adding an anti-slip controller to the driving wheel, the slip rate can be maintained within a range of 0–0.2. According to the pre-experimental results and the slip rate analysis in Section 3.3.2, the working state of each driving wheel is optimal at this slip rate. In summary, with the addition of an anti-slip drive controller, the absolute values of the slip rates of the four drive wheels can be maintained within the target slip rate range. At this time, the longitudinal adhesion coefficient of the road surface remains in a linear upward range, providing a larger and smoother longitudinal driving force, improving the stability of the lawn mower during autonomous operation, and reducing the working energy consumption of the lawn mower.

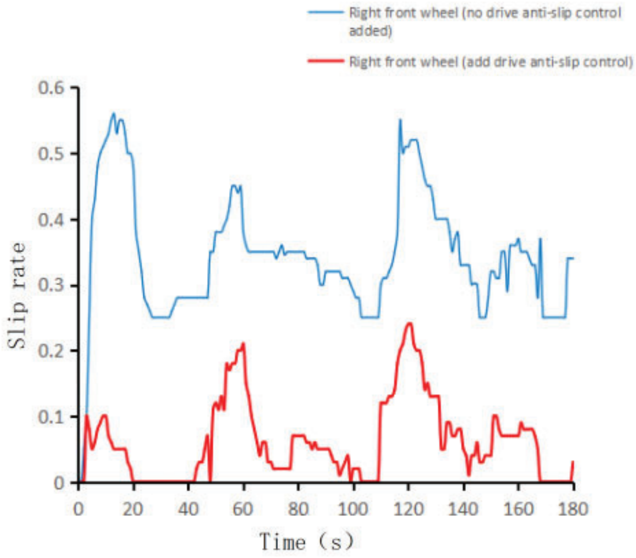

Figure 22. Comparison diagram concerning the slip rate of the front-right wheel.

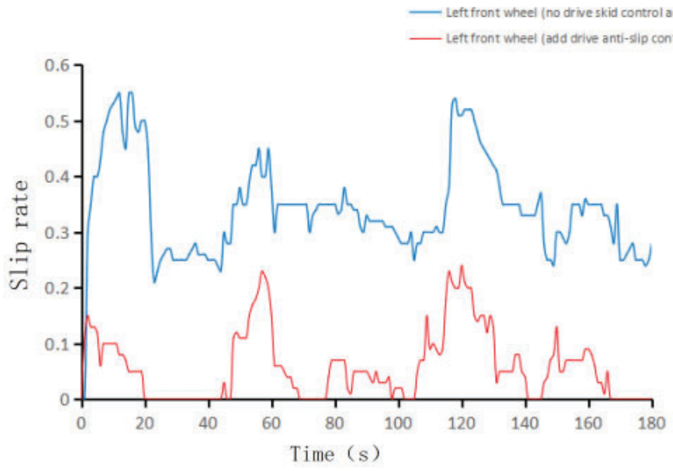

Figure 23. Comparison diagram concerning the slip rate of the front-left wheel.

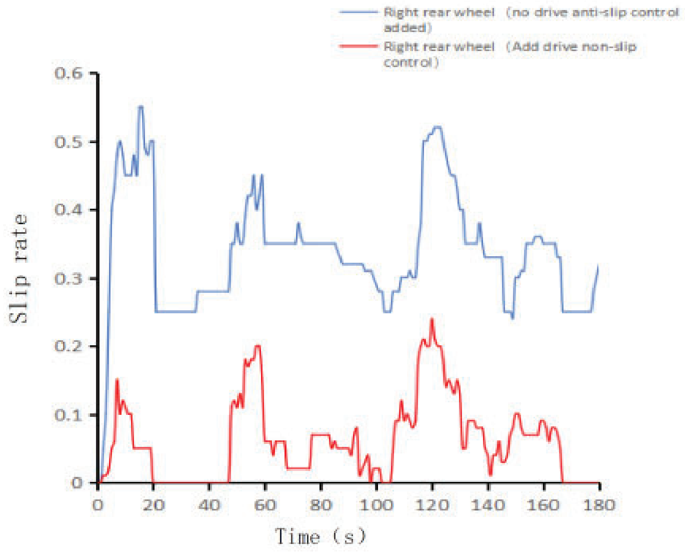

Figure 24. Comparison diagram showing the slip rate of the rear-right wheel.

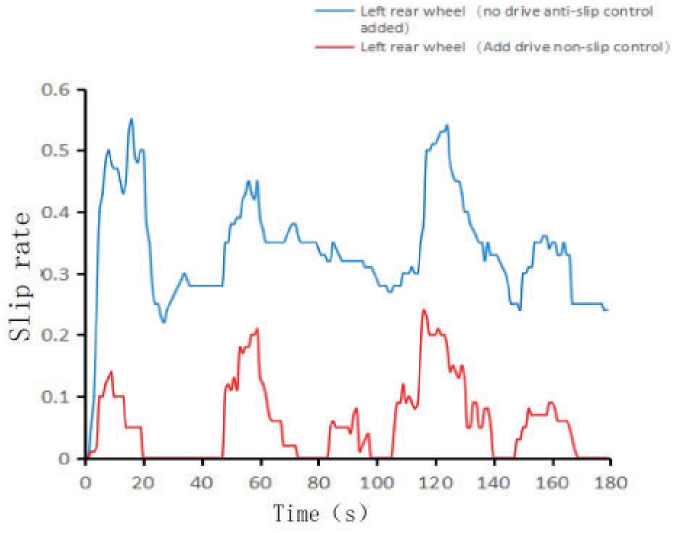

Figure 25. Comparison diagram involving the slip rate of the rear-left wheel.

During the experiment, actual path-tracking points are also collected and compared with the expected path points for data analysis purposes. The period for collecting the experimental data is approximately 180 s after the lawn mower completes a full reference path (as shown in Figure 2), with a path length of approximately 95 m. The results in Figures 26 and 27 indicate that the average absolute values of the lateral errors of the path points can be controlled within 0.05 m, and the average absolute values of the longitudinal errors can be controlled within 0.04 m.

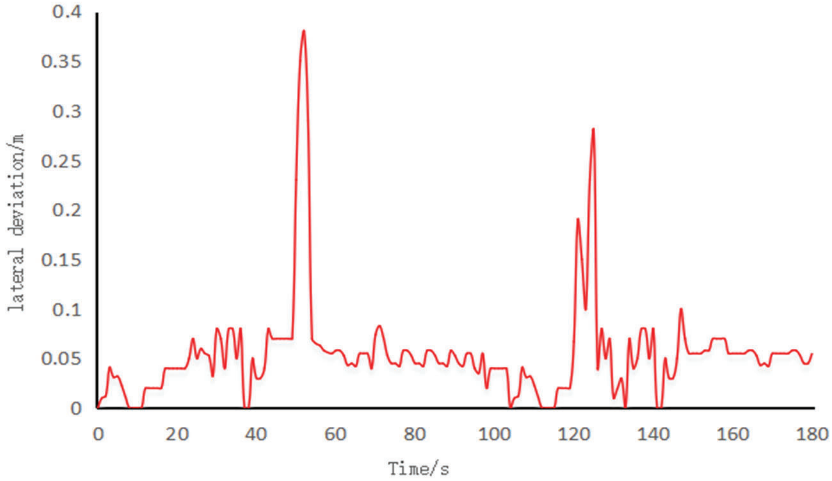

Figure 26. Lateral deviations observed in the orchard pavement test.

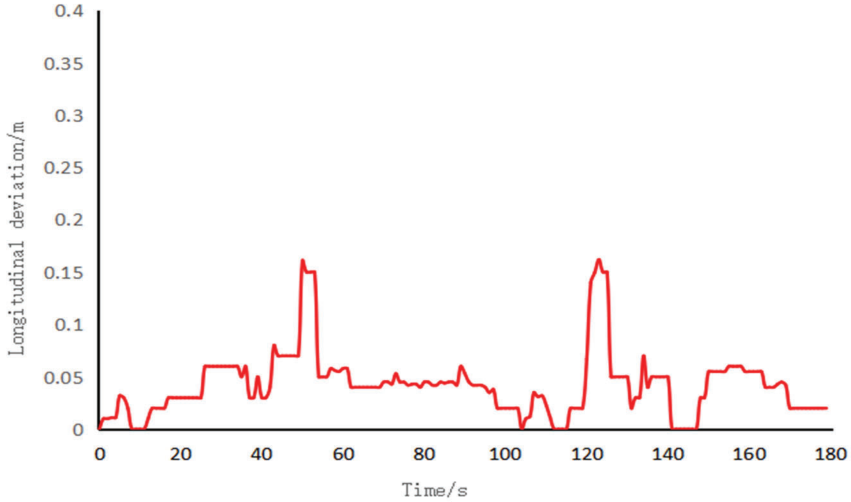

Figure 27. Longitudinal deviations observed in the orchard pavement test.

In this paper, the adaptive time domain MPC and fuzzy control algorithm are combined to establish a path-tracking controller to demonstrate the effectiveness of the path-tracking control strategy in an orchard environment, which is verified by field experiments. Considering the instability of the contact between the mowing robot and the surface of the orchard road, the next step can be used to analyze the constantly changing stress situation of the mowing robot wheel and design an advanced algorithm and a control strategy to improve the reliability of the drive anti-skid control.

5. Conclusions

This paper analyzes and establishes a kinematic model based on MPC for a four-wheel differential mowing robot. The complexity of the given orchard environment leads to excessive slippage by the driving wheel of the mower, which reduces the stability and accuracy of the path tracking of the lawn mower. A path-tracking controller is designed for the lawn mower that consists of an adaptive MPC, fuzzy control, and PID control, which can control the slip rate of the driving wheel to achieve anti-slip drive control.

1. The effectiveness of adaptive time domain MPC and traditional MPC path-tracking controller is compared in a MATLAB simulation. Compared with traditional MPC control, the adaptive time domain MPC path-tracking controller has an average lateral error absolute value that is 3.2 cm smaller and an average longitudinal error absolute value that is 1.7 cm smaller.
2. Simulation experiments are conducted on the designed path-tracking controller combined with anti-slip driving control. The results show that the path-tracking controller with anti-slip driving control added can effectively maintain the slip rate of the driving wheel within the designed target slip rate range on random road surfaces, with an amplitude close to 0.2. The path-tracking controller without an added anti-slip drive controller exhibits a significant change in the slip rate, reaching an amplitude of 0.5. At this time, the lawn mower experiences severe slipping on random road surfaces, which has a significant impact on the effectiveness of path tracking.
3. The field test results show that the lawn mower equipped with a combination of anti-slip drive control and adaptive MPC path tracking has a good effect on tracking the reference path. The average lateral error value can be controlled within approximately 5 cm, and the average longitudinal error value can be controlled within 4 cm. At the same time, the slip rate of the driving wheel can be maintained within the target slip rate range, indicating that the proposed controller can reduce the sliding of the driving wheel while ensuring high path-tracking accuracy.

Author Contributions: Conceptualization: J.L. and S.W.; methodology: J.L. and Y.C.; software: J.L. and S.W.; validation: J.L., S.W., W.Z. and H.L.; formal analysis: J.L., S.W. and H.L.; investigation: J.L.; resources: J.L. and Y.C.; data curation: S.W.; writing—original draft preparation: J.L., S.W., Y.C. and H.L.; writing—review and editing: J.L., S.W., T.W. and Y.Z.; visualization: S.W., R.J., C.M., X.Q. and K.F.; supervision: J.L and Y.C.; project administration: J.L.; funding acquisition: J.L. All authors have read and agreed to the published version of the manuscript.

Funding: This work was supported by the Guangdong Laboratory for Lingnan Modern Agriculture under grants NZ2021040 and NZ2021009, the China Agriculture Research System under grant CARS-32, the Special Project of the Rural Vitalization Strategy of the Guangdong Academy of Agricultural Sciences under grant TS-1-4, and the Guangdong Provincial Modern Agricultural Industry Technology System under grant 2021KJ123.

Data Availability Statement: The data used to support the findings of this study are included within the article.

Conflicts of Interest: The authors declare no conflict of interest.

References

1. FAO (Food and Agriculture Organization of the United Nations). *Recommendations for Improved Weed Management*; Plant Productionand Protection Division: Rome, Italy, 2006; pp. 1–56.
2. Nishimura, Y.; Yamaguchi, T. Grass Cutting Robot for Inclined Surfaces in Hilly and Mountainous Areas. *Sensors* **2023**, *23*, 528. [CrossRef] [PubMed]
3. Ding, Y.; Wang, L.; Li, Y.W.; Li, D.L. Model predictive control and its application in agriculture: A review. *Comput. Electron. Agric.* **2018**, *151*, 104–117. [CrossRef]
4. Chen, S.P.; Xiong, G.M.; Chen, H.Y.; Negrut, D. MPC-based path tracking with PID speed control for high-speed autonomous vehicles considering time-optimal travel. *J. Cent. South Univ.* **2020**, *27*, 3702–3720. [CrossRef]
5. Wang, Z.; Sun, K.; Ma, S.; Sun, L.; Gao, W.; Dong, Z. Improved Linear Quadratic Regulator Lateral Path Tracking Approach Based on a Real-Time Updated Algorithm with Fuzzy Control and Cosine Similarity for Autonomous Vehicles. *Electronics* **2022**, *11*, 3703. [CrossRef]
6. Zhang, C.; Gao, G.; Zhao, C.; Li, L.; Li, C.; Chen, X. Research on 4WS Agricultural Machine Path Tracking Algorithm Based on Fuzzy Control Pure Tracking Model. *Machines* **2022**, *10*, 597. [CrossRef]
7. Zhong, C.-Q.; Wang, L.; Xu, C.-F. Path Tracking of Permanent Magnet Synchronous Motor Using Fractional Order Fuzzy PID Controller. *Symmetry* **2021**, *13*, 1118. [CrossRef]
8. Jeong, Y.; Yim, S. Model Predictive Control-Based Integrated Path Tracking and Velocity Control for Autonomous Vehicle with Four-Wheel Independent Steering and Driving. *Electronics* **2021**, *10*, 2812. [CrossRef]

9. Fue, K.; Porter, W.; Barnes, E.; Li, C.; Rains, G. Autonomous Navigation of a Center-Articulated and Hydrostatic Transmission Rover using a Modified Pure Pursuit Algorithm in a Cotton Field. *Sensors* **2020**, *20*, 4412. [CrossRef]
10. Paramesh, S.; Suresh Rajendran, A. Unified seakeeping and manoeuvring model with a PID controller for path following of a KVLCC2 tanker in regular waves. *Appl. Ocean Res.* **2021**, *116*, 102860. [CrossRef]
11. Yang, Y.; Li, Y.K.; Wen, X.; Zhang, G.; Ma, Q.L.; Cheng, S.K.; Qi, j.; Xu, L.Y.; Chen, L.Q. An optimal goal point determination algorithm for automatic navigation of agricultural machinery: Improving the tracking accuracy of the Pure Pursuit algorithm. *Comput. Electron. Agric.* **2022**, *194*, 106760. [CrossRef]
12. Sun, C.Y.; Sun, P.; Zhou, J.; Mao, J. Travel Reduction Control of Distributed Drive Electric Agricultural Vehicles Based on Multi-Information Fusion. *Agriculture* **2022**, *12*, 70. [CrossRef]
13. Bai, G.; Meng, Y.; Liu, L.; Luo, W.; Gu, Q.; Liu, L. Review and Comparison of Path Tracking Based on Model Predictive Control. *Electronics* **2019**, *8*, 1077. [CrossRef]
14. Wu, H.; Zhang, H.; Feng, Y. MPC-Based Obstacle Avoidance Path Tracking Control for Distributed Drive Electric Vehicles. *World Electr. Veh. J.* **2022**, *13*, 221. [CrossRef]
15. Liu, G.H.; Zhang, H.; Zhang, D.; Shen, Y.; Wang, Z.J.; Xu, Y.D. High clearance four-wheel independent electric drive sprayer path tracking control based on self-correction controller. *J. Phys. Conf. Ser.* **2022**, *2383*, 012043. [CrossRef]
16. Xu, J.H.; Lai, J.; Guo, R.; Lu, X.; Xu, L. Efficiency-Oriented MPC Algorithm for Path Tracking in Autonomous Agricultural Machinery. *Agronomy* **2022**, *12*, 1662. [CrossRef]
17. Manikandan, S.; Kaliyaperumal, G.; Hakak, S.; Gadekallu, T.R. Curve-Aware Model Predictive Control (C-MPC) Trajectory Tracking for Automated Guided Vehicle (AGV) over On-Road, In-Door, and Agricultural-Land. *Sustainability* **2022**, *14*, 12021. [CrossRef]
18. He, J.; Hu, L.; Wang, P.; Liu, Y.X.; Man, Z.X.; Tu, T.P.; Yang, L.N.; Li, Y.Y.; Yi, Y.L.; Li, W.C.; et al. Path tracking control method and performance test based on agricultural machinery pose correction. *Comput. Electron. Agric.* **2022**, *200*, 107185. [CrossRef]
19. Huang, P.K.; Zhang, Z.G.; Luo, X.W.; Liu, Z.E.; Wang, H.; Yue, B.B.; Gao, W.W. Development of external acceleration identification and attitude estimation system of field working vehicle. *Trans. Chin. Soc. Agric. Eng.* **2019**, *35*, 9–15.
20. Ge, L.H.; Zhao, Y.; Ma, F.W.; Guo, K.H. Towards longitudinal and lateral coupling control of autonomous vehicles using offset free MPC. *Control Eng. Pract.* **2022**, *121*, 105074. [CrossRef]
21. Guo, J.C.; Shen, W.B.; Ning, J.S. Development of Lee's exact method for Gauss–Krüger projection. *J. Geod.* **2020**, *94*, 58. [CrossRef]
22. Liu, X.X.; Wang, W.; Li, X.L.; Liu, F.S.; He, Z.H.; Yao, Y.Z.; Ruan, H.P.; Zhang, T. MPC-based high-speed trajectory tracking for 4WIS robot. *ISA Trans.* **2022**, *123*, 413–424. [CrossRef] [PubMed]
23. Wang, W.R.; Yan, J.H.; Wang, H.; Ge, H.L.; Zhu, Z.Y.; Yang, G.J. Adaptive MPC trajectory tracking for AUV based on Laguerre function. *Ocean Eng.* **2022**, *261*, 111870. [CrossRef]
24. Goncalo, C.P.; Wahlberg, B.; Pettersson, H.; Martensson, J. Adaptive reference aware MPC for lateral control of autonomous vehicles. *Control Eng. Pract.* **2023**, *132*, 105403. [CrossRef]
25. Guan, L.; Liao, P.; Wang, A.; Shi, L.; Zhang, C.; Wu, X. Path tracking control of intelligent vehicles via a speed-adaptive MPC for a curved lane with varying curvature. *Proc. Inst. Mech. Eng. Part D J. Automob. Eng.* **2022**, 09544070221133967. [CrossRef]
26. Pacejka, H.B. *Tire and Vehicle Dynamics*; Elsevier: Oxford, UK, 2012.
27. Juan, C.; Javier, P. A Procedure for Determining Tire-Road Friction Characteristics Using a Modification of the Magic Formula Based on Experimental Results. *Sensors* **2018**, *18*, 896.
28. Bakker, G.E.; Pacejka, H.B.; Lidner, L. A New Tire Model with an Application in Vehicle Dynamics Studies. *SAE Paper* **1989**, *98*, 101–113.
29. Yang, S.; Feng, J.; Song, B. Research on Decoupled Optimal Control of Straight-Line Driving Stability of Electric Vehicles Driven by Four-Wheel Hub Motors. *Energies* **2021**, *14*, 5766. [CrossRef]
30. Stephen, B.J.; Emmanuel, G.D.; Afeez, A.; David, O.O.; Ban, M.K. Metaheuristic algorithms for PID controller parameters tuning: Review, approaches, and, open problems. *Heliyon* **2022**, *8*, e09399. [CrossRef]

frontiers | Frontiers in Plant Science

TYPE Original Research
PUBLISHED 20 November 2025
DOI 10.3389/fpls.2025.1616371

OPEN ACCESS

EDITED BY
Jefferson Souza,
Federal University of Uberlandia, Brazil

REVIEWED BY
Ivo Kljenak,
Institut Jožef Stefan (IJS), Slovenia
Pei Wang,
Southwest University, China

*CORRESPONDENCE
Yachao Cao
yccaoryan@scau.edu.cn

RECEIVED 22 April 2025
ACCEPTED 13 October 2025
PUBLISHED 20 November 2025

CITATION
Li J, He H, Fan H, Lie Y, Li Y and Cao Y (2025) Research on gas-liquid coupled flow field dynamics and atomization characteristics of multi-duct sprayers based on CFD. *Front. Plant Sci.* 16:1616371.
doi: 10.3389/fpls.2025.1616371

Research on gas-liquid coupled flow field dynamics and atomization characteristics of multi-duct sprayers based on CFD

Jun Li[1,2,3], Hongwei He[1], Hongtao Fan[1], Yilin Lie[1], Yuhao Li[1] and Yachao Cao[1]*

[1]College of Engineering, South China Agricultural University, Guangzhou, China, [2]Guangdong Laboratory for Lingnan Modern Agriculture, Guangzhou, China, [3]State Key Laboratory of Agricultural Equipment Technology, Beijing, China

This study addresses the issues of prolonged testing cycles and high costs associated with traditional sprayers. Using Computational Fluid Dynamics method, a simulation model of the gas-liquid coupling flow field for multi-duct sprayer was established, and the effects of operational parameters, the air outlet opening angle, interval, and air velocity on droplet deposition and atomization characteristics were systematically investigated. A multi-factor simulation test was conducted by constructing a CFD simulation model, performing multi-polyhedron meshing, and applying the RNG k-ε turbulence model along with the Discrete Phase Model. The results demonstrate that as the flow rate increases from 0.03 kg/s to 0.06 kg/s, the mean thickness of the liquid film and the uniformity index of its distribution both increased, from 197.3 μm and 0.7521 to 340.71 μm and 0.8465 respectively. Medium spray angles and small inner diameter nozzles optimize the uniformity of liquid film distribution, indirectly revealing the effects of each parameter on droplet deposition and its distribution uniformity. When the air outlet opening angle increases from 70° to 80° and then to 90°, the effective working height of the airflow field increases by 0.2 m and 0.1 m, respectively. However, increasing the interval leads to a decrease in the uniformity of the end velocity. The droplets undergo two atomization events within the airflow field. Following the first atomization, the particle size increases due to collisions and merging. The secondary atomization, occurring at a distance of 1.2 m from the air outlet, reduces the particle size and enhances deposition efficiency. Furthermore, as the initial air velocity decreases, the particle size of the droplets within the airflow field tends to increase. The reliability of the CFD simulation model developed in this study were validated through a droplet particle size measurement test. The test results demonstrated that the trend of the measurement values aligned with the simulation values, with the relative error ranging from 11.4% to 15.3%. This research reveals the gas-liquid coupling mechanism within the multi-duct spray flow field, providing a theoretical foundation for the further optimization and modification of this sprayer, thereby significantly reducing costs and improving efficiency.

KEYWORDS

Cfd, multi-duct sprayer, gas-liquid coupling, atomization characteristics, simulation test

1 Introduction

Pests and diseases represent a critical challenge in fruit cultivation, with their prevention and control being a key component of effective orchard management (Ma et al., 2021; Chen et al., 2023; Xue et al., 2023). Traditionally, chemical control methods have been widely employed due to their effectiveness in managing pests and diseases, as well as their ease of application. However, chemical control methods also present several significant challenges. Chemical residues may persist, leading to environmental pollution, food safety concerns, and potential risks to human health. According to data from the FAOSTAT pesticide use database, global agricultural pesticide consumption reached 3.7 million tons in 2022, marking a 4% increase from 2021 and a 13% rise over the past decade. However, a significant disparity remains in pesticide utilization rates among the world's leading pesticide-consuming countries. The air-assisted sprayer is one of the most commonly used pieces of equipment in contemporary orchard plant protection systems. Specifically, multi-duct air-assisted spraying technology allows simultaneous application through multiple air ducts. The high-speed airflow generated by the fan causes the leaves to flip, enabling droplets to penetrate the branches and canopy interior, thus enhancing spraying efficiency, uniformity, and overall pesticide application effectiveness (Gu et al., 2014; Zhai et al., 2021). However, the operational effectiveness of the sprayer is constrained by various factors in practical application scenarios (Jiang et al., 2020). Therefore, conducting research on the sprayer using simulation method is crucial (Li et al., 2021). Computational Fluid Dynamics (CFD), the product of integrating computer science and fluid mechanics, has become a vital tool in engineering design and optimization. Simultaneously, CFD has emerged as one of the primary methods for both domestic and international scholars to study the motion characteristics and distribution patterns of the external flow field in orchard air-conveying sprayers (Zhai et al., 2021).

Currently, researchers both domestically and internationally primarily employ CFD simulation method to investigate the airflow characteristics, distribution of airflow fields, and the droplet deposition patterns in orchard air-assisted sprayers (Baetens et al., 2007; Lee et al., 2013; Wei et al., 2023) (García-Ramos et al., 2015). developed several models of air-assisted sprayers utilizing CFD method. These models are capable of simulating the airflow field produced by the sprayer, incorporating critical parameters such as velocity, direction, and turbulence intensity. In order to validate the accuracy of the CFD models, they measured the airflow generated by the sprayer using a 3D acoustic anemometer and compared the results with the CFD simulation outcomes to confirm the model's reliability (Dekeyser et al., 2013). investigated the airflow characteristics and droplet deposition patterns of the tower-type air-delivered sprayer through both simulation and experimental approaches. The results revealed that droplet deposition on both sides of the tower-type sprayer exhibited asymmetry, and the distribution of the pesticide in the vertical cross-section of the canopy was strongly correlated with the sprayer's airflow field (Delele et al., 2007). developed a CFD model to simulate and validate a cross-flow air-delivered sprayer. The results indicated that the model effectively predicted droplet dispersion and deposition during the spraying process, thereby offering a robust tool for the design and optimization of the sprayer (Gu et al., 2014) performed an experimental study on the airflow dynamics of the multi-duct sprayer in orchards. The study demonstrated the attenuation of wind speed and jet airflow force as they penetrated the canopy (Endalew et al., 2010). introduced a novel integrated CFD modeling approach and validated it through numerical simulations and wind tunnel experiments for air-assisted spraying in orchards. They also conducted a comprehensive study on the effects of wind speed and direction on spraying performance (Li et al., 2023). assessed critical indicators, including spray performance, droplet size distribution, and spray coverage rate, of the multi-pipe orchard sprayer using field tests and laboratory simulations. They optimized the sprayer's structure using CFD simulation method to ensure the efficiency of spray airflow and droplet distribution. The findings indicate that the multi-pipeline orchard sprayer can substantially increase spray coverage, reduce pesticide loss, and maintain droplet size uniformity (Huang et al., 2025). used CFD method to model and analyze the airflow field of the wind-driven sprayer in citrus orchards. The study constructed a three-dimensional fluid domain model using SolidWorks, which included the intake zone, rotation zone, diversion zone, and external flow field zone. The numerical simulation was carried out using Fluent software. The gas-phase turbulence was modeled using the RNG k-ε model, and the movement of the droplets was tracked using DPM. The pressure-speed field was coupled based on the SIMPLE algorithm. The model was verified through wind speed boundary experiments. The relative error between the simulated wind speed at the center axis and the measured value was less than 21%, confirming the reliability of the CFD results.; (Duga et al., 2017) developed a 3D CFD model based on computational fluid dynamics principles to simulate the spraying process of air-assisted orchard sprayers. This model accurately predicts and simulates the trajectory of spray drift, reducing drift by at least 50%. The CFD model developed by (Hong et al., 2018) simulates the airflow distribution of the air-assisted sprayer within the tree canopy. By incorporating the sprayer's movement and the tree canopy's influence via sliding mesh method and User-Defined Functions (UDFs), the canopy is modeled as a virtual porous medium, thus simplifying the modeling process. The model verification indicates that the simulation results are generally consistent with measured data and can reliably predict airflow distribution. It can provide a reference for improving spray efficiency and predicting spray drift.

In conclusion, both domestic and international researchers have extensively studied the modeling techniques of external flow fields and the airflow distribution of various sprayer types. It has been observed that multi-duct spraying methods significantly enhance the operational performance of sprayers; however, studies addressing the gas-liquid coupling in the external flow field at the multi-duct outlet remain limited. This study aims to investigate the influence of various factors on the external multi-duct flow field of the sprayer during operation in orchard environments. A computational fluid dynamics (CFD) model is employed to establish the external fluid calculation framework for the multi-duct sprayer, with the objective of analyzing the gas-liquid coupling distribution within its external flow field. Based on these findings, the distribution patterns are derived to inform the subsequent optimization of sprayer performance and the refinement of profiling operations.

2 Materials and methods

2.1 Structure and principle

The air delivery system of the orchard's multi-duct sprayer consists of a centrifugal fan, an eight-outlet air duct distributor, flexible air ducts, and air outlets, as illustrated in Figure 1. When the system operates, the gasoline engine drives the pulley to transmit power to the transmission shaft of the centrifugal fan, which then rotates the fan and generates high-speed airflow. The airflow is directed through the eight-outlet air duct distributor, flows through the flexible air duct, and is finally expelled through the air outlet. After mixing with the atomized liquid droplets sprayed from the atomizing nozzle at the air outlet, the airflow and droplets are directed into the canopies of the fruit trees on both sides (Yang et al., 2024).

2.2 Model establishment and meshing

2.2.1 The air outlet structure design

The design of the air outlet structure aims to enhance both the wind speed and the uniformity of the airflow at the outlet. The air outlet consists of a cylindrical section, a layout section, and a fan-shaped section. As shown in Figure 2 below. The cylindrical section is designed to have a length of 100 mm, the layout section a length of 130 mm, and the fan-shaped section a length of 100 mm. Four deflector plates are incorporated within the cylindrical section. The length of the deflector plates is matched to that of the cylindrical section. This is intended to enhance the energy transfer efficiency of the airflow from the flexible air duct to the outlet and effectively mitigate the energy losses resulting from vortices. The cross-sectional area of the fluid in the layout section first contracts and

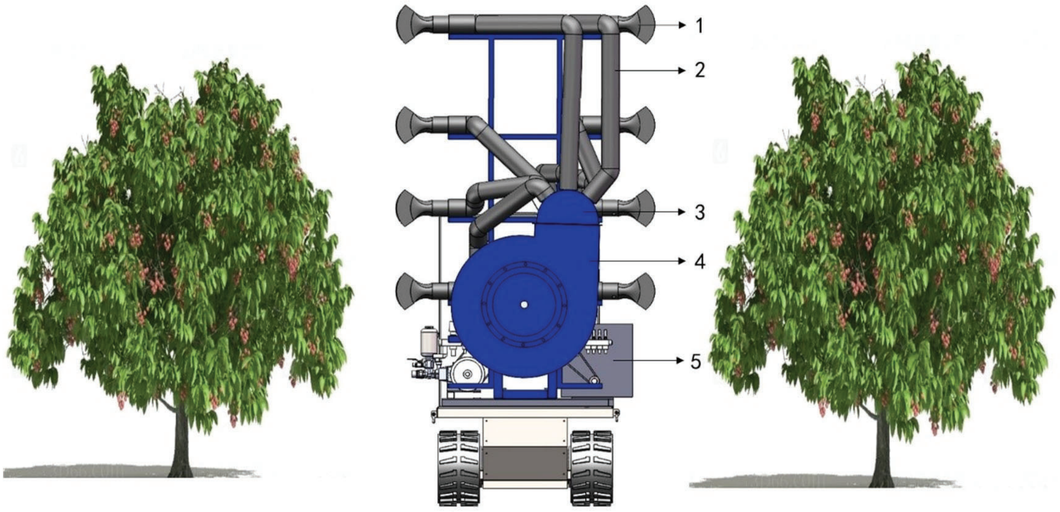

FIGURE 1
Structure and principle diagram. 1. The air outlet 2. Flexible air duct 3. Eight-outlet air duct distributor 4. Centrifugal fan 5. Gasoline engine.

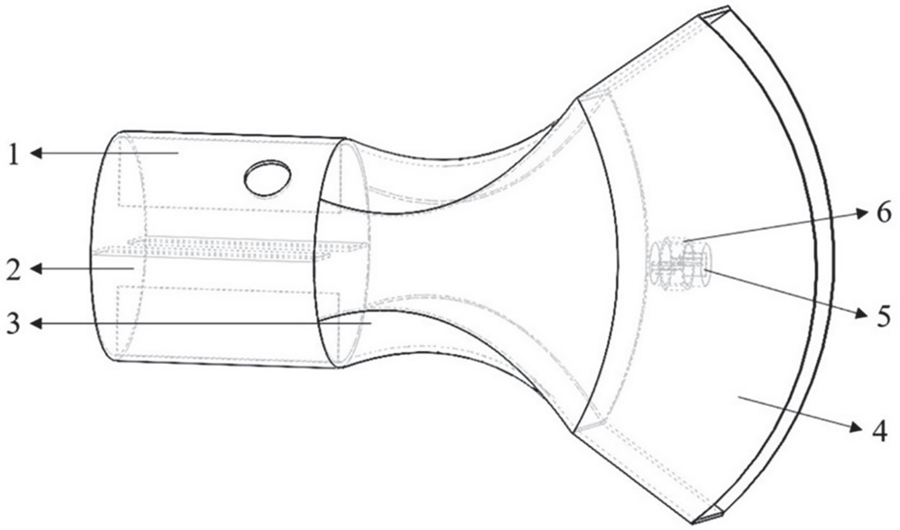

FIGURE 2
Structure diagram of the air outlet. 1. Deflector plates 2. Cylindrical section 3. A layout section 4. Fan-shaped air outlet section 5. Flat fan atomizer 6. Nozzle fixing frame.

then expands. In the contraction section, the fluid velocity increases while the pressure decreases. In the expansion section, the velocity continues to increase while the pressure decreases, contributing to the further acceleration of the gas flow. The fan-shaped section serves to augment the vertical flow amplitude while reducing the cross-sectional area of the fluid, thereby maintaining the air velocity at the outlet.

2.2.2 Establishment of multi-duct flow field model

This study aims to investigate the movement characteristics of droplets in the external flow field of a multi-duct sprayer influenced by the airflow field, with the goal of offering insights for its subsequent optimization. Based on the actual working conditions, a geometric model of the outflow field of multiple air ducts was created in SolidWorks software to enhance simulation efficiency and simplify the working area. In this model, the geometry is simplified into a rectangular domain measuring 1500 mm × 400 mm × 3500 mm, which includes four air outlets and a fluid computational domain, as illustrated in Figure 3. In the figure, the black arrow represents the entrance of the airflow into the computational domain, and the red arrow represents that the airflow can flow out from here. The area below the computational domain is regarded as the ground surface, and the airflow cannot escape from this area.

The established model is imported into SpaceClaim software, where the fluid computational domain is extracted, and boundary conditions are defined. The bottom of the model is considered as the ground surface. In practical applications, airflow in contact with the ground surface will not escape. Consequently, the bottom boundary is defined as a no-slip wall. Additionally, the wall at the end of the computational domain is defined as a solid boundary to facilitate subsequent analysis of the liquid film thickness. The remaining surfaces of the model, excluding the four air outlets, are considered as surfaces where airflow can escape, and are defined as pressure outlets. Subsequently, the outer surfaces of the four air outlets are defined as walls. Finally, the fluid computational domain is extracted, and the defined model is imported into Ansys Fluent for further processing (Zhang et al., 2022).

2.2.3 Meshing

Given that the research model in this study incorporates the multi-channel flow field of droplet movement, the entire model is partitioned into three distinct regions for meshing. The fluid computational domain at the air inlet, as well as the region adjacent to it, undergoes grid refinement, with similar grid refinement applied at the nozzle particle outlet and its vicinity. The remaining fluid domain is discretized using polyhedral grids. Polyhedral grids not only ensure computational accuracy but also reduce computational costs, while offering high grid division efficiency. This study has validated grid independence and identified that the calculation achieves maximum efficiency when the number of grids is 1149854. The grid diagram of the fluid calculation domain is shown in Figure 4.

2.3 Gas-liquid coupling numerical model

2.3.1 Turbulence model

The airflow field simulated in this study corresponds to a physical field that adheres to turbulent flow characteristics. Currently, the k-ε model within the Reynolds-averaged Navier-Stokes (RANS) framework is the most commonly employed for simulating gas turbulence. In the Fluent software, the most commonly utilized k-ε models include the Standard, Realizable, and RNG models. The Standard k-ε model is the most

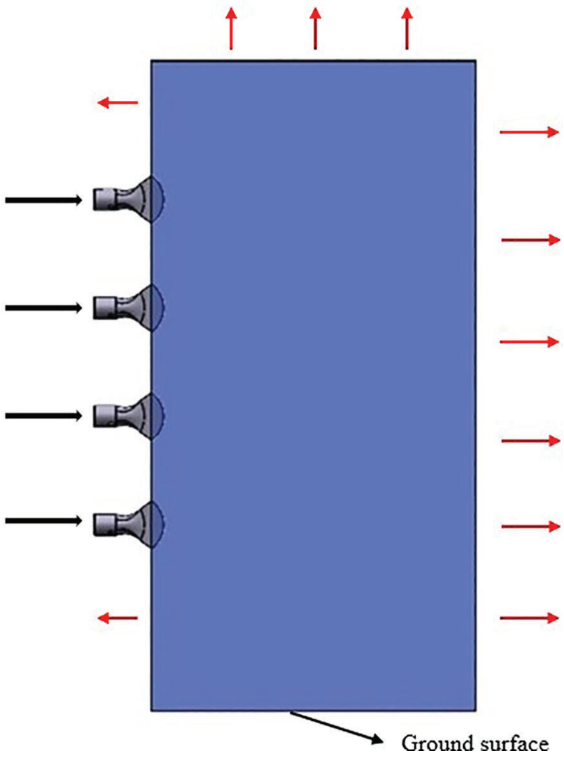

FIGURE 3
Three-dimensional model of the flow field.

straightforward and fundamental turbulence model among the two-equation models. It determines the turbulence length and timescales by solving two independent transport equations. During the derivation of this model, it is assumed that the flow is fully turbulent, and the effect of molecular viscosity is negligible. As a result, the Standard model is only applicable in fully turbulent conditions. The Realizable k-ε model is primarily employed to address scenarios involving particularly high strain rates in turbulent flow. The RNG k-ε model accounts for the influence of vortices on turbulence, building upon the Standard k-ε model, and demonstrates superior accuracy and reliability in airflow simulations. Accordingly, this study adopts the RNG k-ε model and employs its governing equations. The expressions for the transport equations are as follows:

$$\frac{\partial(\rho k)}{\partial t} + \frac{\partial(\rho k u_i)}{\partial x_i} = \frac{\partial}{\partial x_j}\left(\alpha_k \mu_{eff}\frac{\partial k}{\partial x_j}\right) + G_k + G_b - \rho\varepsilon - Y_M + S_k \tag{1}$$

$$\frac{\partial(\rho\varepsilon)}{\partial t} + \frac{\partial(\rho\varepsilon u_i)}{\partial x_i} = \frac{\partial}{\partial x_i}\left(\alpha_\varepsilon \mu_{eff}\frac{\partial \varepsilon}{\partial x_j}\right) + C_{1\varepsilon}\frac{\varepsilon}{k}(G_k + C_{3\varepsilon}G_b) - C_{2\varepsilon}\rho\frac{\varepsilon^2}{k} - R_\varepsilon + S_\varepsilon \tag{2}$$

In Equations 1, 2, x represents the spatial coordinate, u is the component of the velocity vector, k represents the turbulent kinetic energy, ε denotes the dissipation rate, α_k and α_ε are respectively the inverse turbulent Prandtl numbers of k and ε, μ_{eff} represents the effective viscosity, G_k corresponds to the turbulent kinetic energy generated by the average velocity gradient, G_b is the turbulent kinetic energy generated by buoyancy, Y_M represents the contribution of wave expansion to the total dissipation in compressible turbulence, $C_1\varepsilon$, $C_2\varepsilon$ and $C_3\varepsilon$ are constants, while S_k and $S\varepsilon$ are user-defined source terms.

2.3.2 Droplet motion model

In computational fluid dynamics (CFD) studies of spray fields, the Discrete Phase Model (DPM) serves as a crucial method for studying particle motion. It has been extensively validated in the literature and has been shown to effectively simulate particle movement within spray fields (Adeniyi et al., 2017). In DPM simulations, the airflow, representing the continuous phase, is iteratively solved using the Euler equation, while droplet particles, representing the discrete phase, are iteratively computed using the Lagrange equation. Hence, this model is referred to as the Euler-Lagrange model, and its governing transport equation is presented in Equation 3 as follows:

$$\frac{dv_p}{dt} = \frac{18\mu C_D \mathrm{Re}}{24\rho_P d_p^2}(v - v_p) + \frac{g(\rho_p - \rho)}{\rho_p} \tag{3}$$

In the formula, v represents the velocity of the continuous phase (m/s); v_p represents the discrete phase velocity (m/s); μ represents dynamic viscosity (Pa·s);C_D refers to the drag coefficient, Re indicates the relative Reynolds number, ρ_p denotes the particle density (kg/m³), ρ represents the gas density (kg/m^3), d_p represents the particle diameter (m), and g represents the gravitational acceleration (m/s²).

The drag coefficient is typically associated with the Reynolds number. In the Discrete Phase Model (DPM), particles are assumed to be spherical by default. The expression for the drag coefficient of spherical particles is provided in Equation 4 below.

$$C_d = \begin{cases} \frac{24}{R_e}(1 + 0.15R_e^{0.687}), R_e < 1000 \\ 0.44, R_e > 1000 \end{cases} \tag{4}$$

During the calculation process, since the gas flow density is approximately constant, a pressure solver is selected for the two-phase steady-state calculation. The pressure-velocity coupling adopts a simple algorithm (SIMPLE), the pressure is discretized using the second-order scheme, and the momentum and turbulence intensity are discretized using the second-order upwind scheme. Furthermore, when the particle volume fraction is below 10% - 12%, its effect on the airflow field can be neglected, and the single-phase coupling method is applied to solve the particle motion problem. By calculating the changes in momentum and mass of a single control volume in the model, the effect of airflow on the momentum and mass of the droplet particles can be determined.

2.3.3 Atomizing nozzle model

This study employs the flat fan atomizer within the Discrete Phase Model (DPM) framework to simulate the behavior of a fan atomizing nozzle. When a jet is formed through a flat fan-shaped nozzle, the resulting impact force is significant, leading to the formation of uniformly sized droplet particles. The spray range is broad and adjustable, making it widely applicable in orchard plant protection operations (Cao et al., 2020). This atomizing nozzle model is applied at the flat fan atomizer described earlier. Liquid flows out from here in the form of particles and enters the entire fluid calculation domain. Figure 5 illustrates the schematic diagram of the fan-shaped nozzle, while the key model parameters are presented in Table 1.

2.3.4 Droplet collision and breakup model

(1) Droplet collision model

The droplet collision model is applicable to collisions characterized by low Weber numbers, where the outcomes are limited to merging and rebounding (Jiang et al., 2022). Collisions among spray droplets occur exclusively within the same computational grid. When the positions of the internal spray droplets are uniformly distributed, the probability of capturing the droplets within the colliding body is:

$$P_1 = \frac{\pi(r_1 - r_2)^2 v_{rel} \Delta t}{V} \tag{5}$$

In Equation 5, r_1 and r_2 represent the radius of droplet 1 and droplet 2, v_{rel} denotes the relative velocity between droplet 1 and droplet 2, Δt is the calculation time step, and V is the volume of the grid cell.

The probability distribution for the number of droplet collisions follows a Poisson distribution, as shown in Equation 6, k represents the number of droplet collisions.

$$P(k) = \frac{\lambda^k e^{-\lambda}}{k!} \tag{6}$$

When two droplets collide, the collision result will also be determined as merging or rebounding, and the function (Sun et al., 2012) of its critical value is as shown in Equation 7.

$$b_{crit} = (r_1 + r_2)\sqrt{\min\left(1.0, \frac{2.4f}{We}\right)} \tag{7}$$

In Equation 8, f is a function of r_1/r_2, and its definition expression is:

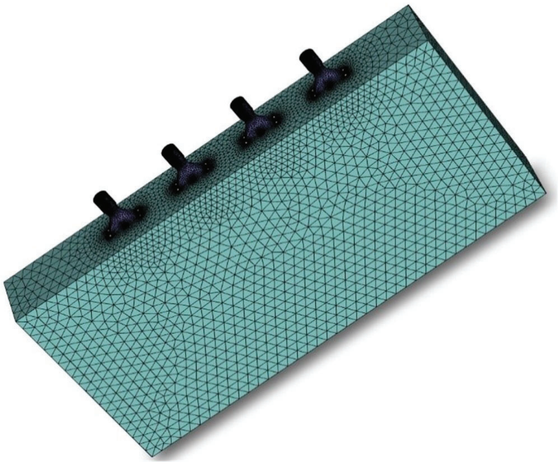

FIGURE 4
Fluid computational domain grid diagram.

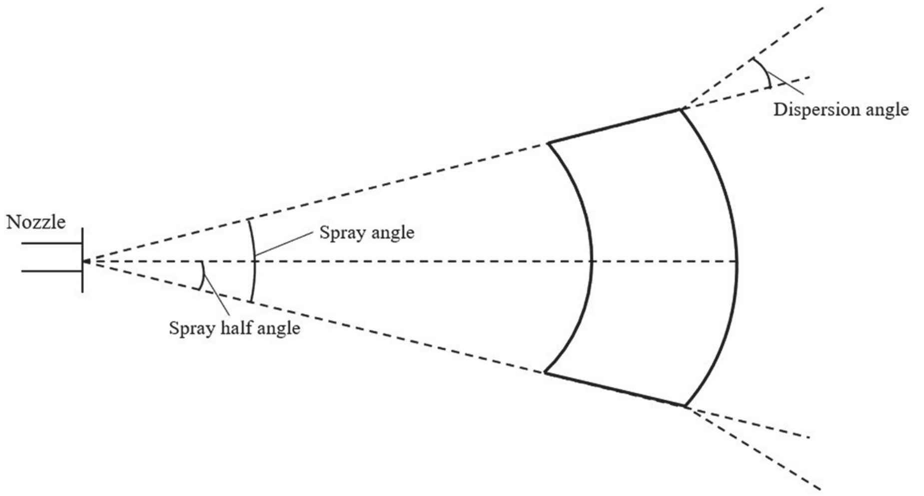

FIGURE 5
Schematic diagram of the flat fan atomizer model.

$$f\left(\frac{r_1}{r_2}\right) = \left(\frac{r_1}{r_2}\right) - 2.4\left(\frac{r_1}{r_2}\right) + 2.7\left(\frac{r_1}{r_2}\right) \tag{8}$$

The value of parameter b, obtained from the collision calculation, is $(r_1 + r_2)\sqrt{Y}$, where Y represents the average deviation. Droplet coalescence occurs when the impact parameter b is less than the value b_{crit}; otherwise, they rebound.

(2) Droplet breakup model

Droplets experience shear forces in the airflow field. The aerodynamic forces acting on them may exceed the capacity of their surface tension, causing the droplets to deform and fragment into smaller particles. This process is characterized by the We number:

$$We = \frac{\rho_{\mathrm{air}} v^2 d}{\sigma} \tag{9}$$

In Equation 9, We represents the collision Weber number, ρ_{air} represents the density of air, v represents the relative velocity, d represents the droplet diameter, and σ represents the surface tension coefficient.

Ansys Fluent software supports two droplet breakup models: the Taylor Analogy Breakup(TAB) model and the Wave Breakup model. The TAB model is primarily applied in spray processes with a low We number and is suitable for low-speed spray processes, while the wave fragmentation model is applicable when $We > 100$ and is typically used in high-speed spraying (Marek, 2013). In conclusion, since this study involves simulating the agricultural spray operation environment, which corresponds to a low-speed spray process, the TAB droplet breakage model is selected.

2.3.5 Boundary conditions

During the numerical simulation of gas-liquid coupling, both initial and boundary conditions must be defined. This section focuses on the distribution of the external flow field of multiple air ducts during sprayer operation, where the gaseous phase is modeled as air at standard temperature, and the liquid phase is represented by water liquid, with the particle type specified as droplets in the Discrete Phase Model (DPM). Based on previous selections of the centrifugal fan and simulations of the internal flow field within the air delivery system, the average velocity for each air inlet and outlet was determined. The air inlets for all the air outlets were specified as velocity inlets, with a velocity of 45 m/s. Meanwhile, set the turbulence intensity to 5% and the turbulence viscosity ratio to 10. The gas-liquid two-phase flow model incorporates the DPM model, building on the single-phase airflow field model. The boundary condition for the wall at the end of the computational domain is specified as a trap, with the liquid film wall option simultaneously activated. The remaining outlet boundaries and the ground wall are set as escape boundaries, where droplet particles are allowed to exit. The walls of the four air outlets are designated as reflective boundaries, meaning that particles will be reflected upon contact.

TABLE 1 Key parameter settings of the flat fan atomizer model.

Name of parameters	Value
X-fan normal vector	0
Y-fan normal vector	0
Z-fan normal vector	1
Flow rate(kg/s)	a
Spray angle(deg)	b
Orifice width(mm)	c
Flat fan sheet constant	3
Dispersion angle(deg)	6

In the table, a, b, and c represent the values of flow rate, spray angle, and orifice width respectively.

2.4 Simulation test on influencing factors of multi-duct spray operation

The Euler wall liquid film model presents an innovative approach for simulating the formation and evolution of wall liquid films. It allows for a more accurate calculation of the adhesion and evolution processes of liquid films on the wall, providing a more realistic representation of the formation of wall liquid films by water droplet particles. Additionally, the thickness of the liquid film serves as an indirect indicator of droplet deposition. When the spraying simulation time remains constant, a thicker liquid film correlates with a higher aggregation of droplets. This indicates that the effectiveness of droplet deposition improves as the liquid film thickness increases (Chen et al., 2015). Thus, the liquid film thickness at the end plane of the computational domain is utilized as one of the evaluation metrics for the simulation experiments, as illustrated in Figure 6. Moreover, in the post-processing of Ansys Fluent, the uniformity index is used to evaluate the uniformity of the liquid film thickness distribution on the liquid film collection surface, with values ranging from 0 to 1. A higher value indicates greater uniformity. Therefore, to indirectly assess the uniformity of droplet deposition, this study incorporates the uniformity index of the liquid film distribution as another evaluation metric for the experimental results, with the simulation outcomes being jointly evaluated using both indices. Additionally, this study reasonably selects the experimental factors and determines the range of factor levels through pre-simulation experiments.

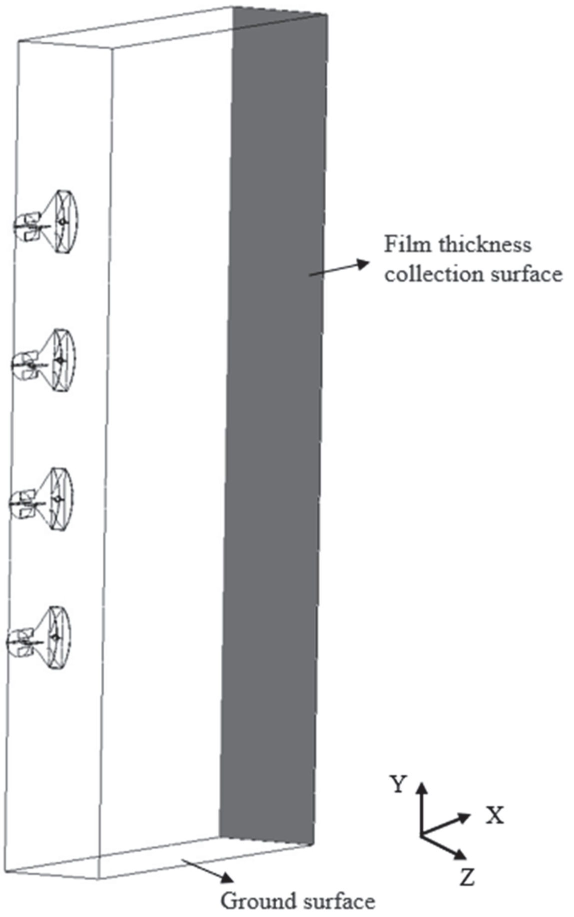

FIGURE 6
Schematic diagram of the liquid film thickness collection surface.

The liquid flow rate at the nozzle outlet quantifies the mass of liquid discharged from the nozzle per unit of time, serving as a critical parameter influencing the extent of droplet deposition. Furthermore, the flat fan atomizer employed in this study allows for modulation of the spray angle, thereby increasing or decreasing the spray amplitude at the nozzle outlet. The magnitude of the spray amplitude influences droplet interactions between sprays from multiple nozzles, ultimately affecting the final droplet deposition pattern. The nozzle orifice width directly determines the droplet particle outlet diameter. The droplet particle outlet diameter influences the extent of droplet breakage during interactions and collisions, thereby affecting the atomization efficiency. Additionally, it exerts a significant influence on the droplet deposition outcome.

In this study, the outlet flow rate, spray angle, and orifice width of the nozzle are chosen as the primary test factors. The levels for each factor are carefully selected to ensure a meaningful investigation. To optimize the simulation process and reduce the computational scale, only a subset of these levels is chosen for the simulation experiments. The corresponding test scheme, as summarized in Table 2, outlines the specific combinations of these factors for the simulations.

2.5 Simulation test on the influence of the air outlet opening degree and interval on the characteristics of multi-duct airflow field

The degree of opening of the air outlet and its interval configuration significantly influences the distribution of the multi-duct spray, as illustrated in Figure 7. In the figure, α denotes the degree of opening of the air outlet, and W represents the interval between the air outlets. This study investigates the effect of varying test levels of air outlet opening degrees and interval on the effective working height of the airflow field, using CFD simulations.

TABLE 2 Simulation test scheme table.

Test groups	Flow rate (kg/s)	Spray angle (deg)	Orifice width (mm)
A	0.03	60	0.6
B	0.04	60	0.6
C	0.05	60	0.6
D	0.06	60	0.6
E	0.03	50	0.6
F	0.03	60	0.6
G	0.03	70	0.6
H	0.03	80	0.6
I	0.03	70	0.4
J	0.03	70	0.6
K	0.03	70	0.8
L	0.03	70	1.0

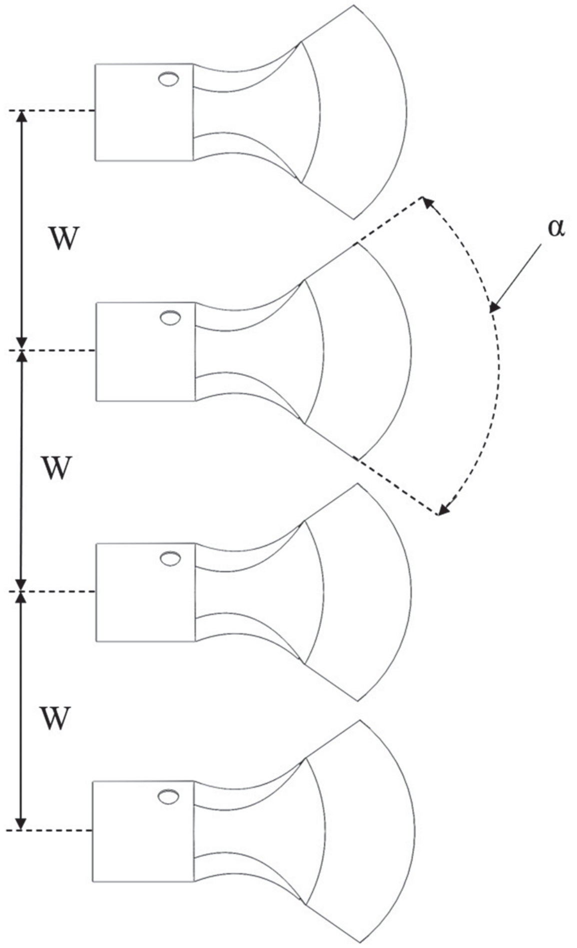

FIGURE 7
Schematic diagram of the opening degree and interval of the air outlet.

However, the simulation content related to the spray was not covered, so the DPM simulation model was not included in the simulation process of this section. Furthermore, monitoring was implemented at the boundary of the computational domain to assess the uniformity of the velocity distribution within the airflow field and to investigate how the air outlet opening degree and interval affect this uniformity. This test provides valuable data and insights that can support the future optimization of the multi-duct sprayer for profiling spray operations.

If the opening of the air outlet is excessively large, it may result in the loss of its air-guiding function. Additionally, the spacing between the air outlets influences the interaction among them. Accordingly, the levels of the test factors are carefully selected in this study. The design of the simulation test scheme is outlined in Table 3.

2.6 Simulation test of atomization characteristics of multi-duct flow field under the action of airflow field

When spray droplets traverse the external flow field generated by multiple air ducts, phenomena such as droplet breakage, collision, and coalescence occur due to the influence of the airflow field. This study aims to investigate the variation of droplet size under the influence of the airflow field generated by multiple air ducts, providing simulation data as a reference for the rational selection of the optimal distance between the multi-air duct sprayer and the fruit tree canopy to achieve precision spraying. Previous studies have simulated the internal flow field of the multi-duct sprayer air distribution system. Based on previous research data, it can be concluded that when the centrifugal fan operates at rated speed, the average inlet velocity at the air outlet is approximately 45 m/s. In this test, three air velocity levels were chosen for simulation, with 35 m/s, 40 m/s, and 45 m/s corresponding to schemes A, B, and C, respectively. Meanwhile, while maintaining other parameters constant, the air outlet opening degree is set at 70°, the interval is 500 mm, the outlet flow rate of the flat fan atomizer is 0.03 kg/s, the spray angle is 70°, and the orifice width is 0.6 mm.

TABLE 3 Simulation test scheme table.

Test groups	The air outlet opening degree α(deg)	The air outlet interval W(mm)
I	70	500
II	80	500
III	90	500
IV	70	600
V	80	600
VI	90	600
VII	70	700
VIII	80	700
IX	90	700

Monitoring planes were set at distances of 0.3 m, 0.6 m, 0.9 m, 1.2 m, and 1.5 m from the nozzle location, denoted as Y1, Y2, Y3, Y4, and Y5, respectively, as illustrated in Figure 8. Subsequently, the temporal variations in droplet size on the monitoring surfaces are analyzed to derive the governing principles of droplet size distribution within the airflow field, followed by the atomization behavior. Finally, within the DPM model, the droplet collision, breakup, and merging models are activated, and the species transport equation is concurrently enabled for computational resolution.

2.7 Droplet particle size measurement test

To verify the CFD simulation model established in this study and enhance its credibility in practical applications, this section presents a droplet particle size measurement test conducted in the agricultural engineering building of South China Agricultural University.

The test was conducted using the HNB-PW1000 laser particle size analyzer. The measurement range of the HNB-PW1000 laser particle size analyzer spans from 1 μm to 1000 μm. Both the measurement accuracy error and the repeatability error are less than 1%. Its working principle involves determining the particle size distribution by measuring the angle and intensity of the scattered light produced by the interaction of the particles with the laser. Additionally, due to the excellent monochromaticity and strong

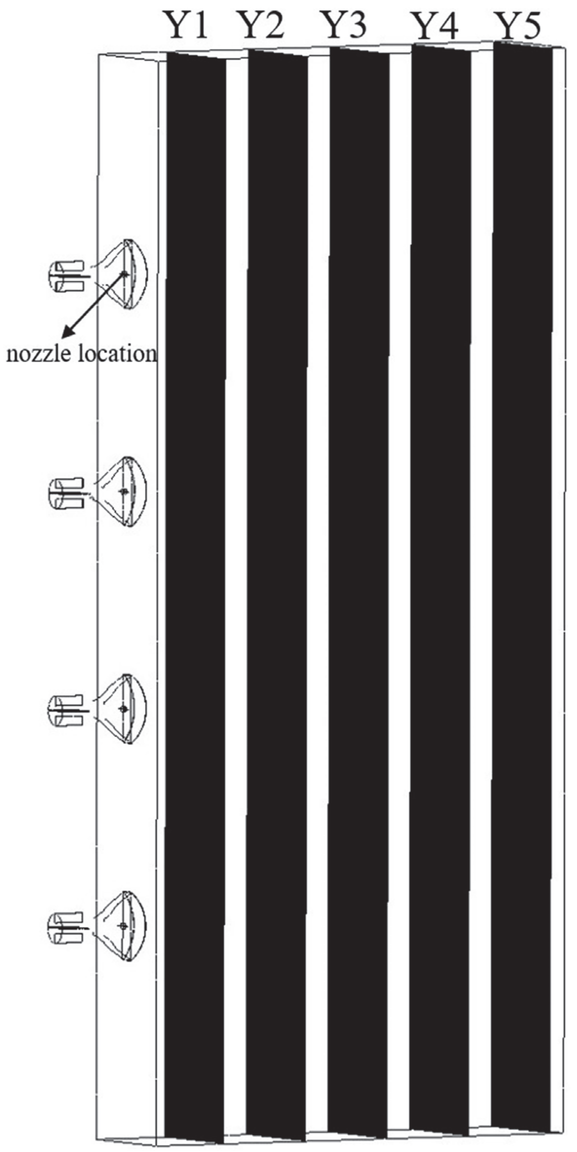

FIGURE 8
Schematic diagram of the monitoring planes for particle diameter distribution.

directionality of the laser, the analyzer achieves high precision and accuracy in particle measurement.

Due to the substantial dimensions of the multi-duct sprayer developed in this study, it is not feasible to assess the entire spray system. Consequently, this test was limited to testing a single duct of the multi-duct sprayer. A flat fan atomizer with a 70° spray angle and a 0.6 mm orifice width was selected for this test. The flow rate was set to 0.03 kg/s. Simultaneously, an air outlet with a 70° opening angle was selected. The rotational speed of the centrifugal fan was calibrated to 961.7 r/min, the rated speed of the fan, corresponding to an inlet air velocity of 45 m/s at the air outlet. Throughout the test, the laser particle size analyzer was positioned at a distance *d* from the outlet, with *d* taking values of 0.3 m, 0.6 m, 0.9 m, 1.2 m, and 1.5 m for five test groups. Each test group was repeated three times to record the measured droplet particle sizes. The particle size is calculated using the volume mean diameter (VMD) of the measurement values. The average of the droplet particle size measurements was then calculated as the test value. The droplet particle size measurement test schematic diagram is shown in Figure 9.

3 Results and discussion

3.1 Simulation test results and analysis of influencing factors in multi-duct spray operations

The simulation results are summarized in Table 4, Additionally, the simulation results for each group are depicted in Figures 10A–L. The figure indicates that the regions of highest concentration of liquid film thickness are primarily located in the middle and lower sections of the collection surface. This outcome is attributed to the consideration of gravitational effects on droplet movement in the simulation process described in this study (Chen et al., 2020). From the overall analysis of Table 4 and Figures 10A–L, it is evident that the flow rate has the most substantial effect on the mean liquid film thickness, whereas the spray angle and nozzle orifice width show no significant impact on the liquid film thickness but notably influence the uniformity index of the liquid film distribution.

(1) The influence of flow rate on the thickness and uniformity of the liquid film

As shown in Table 4 and Figures 10A–10D, an increase in flow rate leads to a significant rise in the mean liquid film thickness, from 197.31 μm to 340.71 μm, suggesting that flow velocity is the primary factor driving this increase. Concurrently, the uniformity index increased from 0.7521 to 0.8465, indicating that a higher flow rate promotes a more uniform distribution of the liquid film. This can be attributed to the fact that an increased flow rate reduces droplet aggregation.

(2) The influence of spray angle on the thickness and uniformity of the liquid film

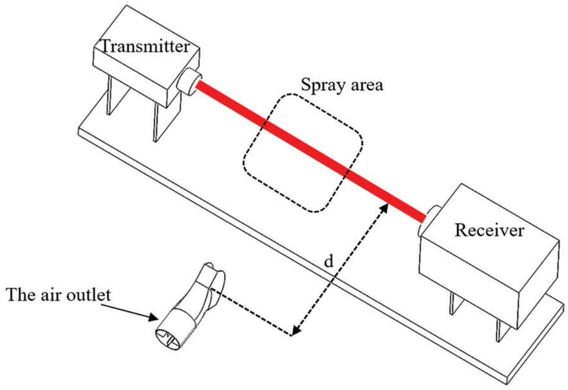

FIGURE 9
Schematic diagram of droplet particle size measurement test.

TABLE 4 Simulation results at different test levels.

Test groups	Mean value of liquid film thickness(μm)	Uniformity index
A	197.31	0.7521
B	252.81	0.8032
C	301.17	0.8325
D	340.71	0.8465
E	196.67	0.7466
F	197.31	0.7521
G	197.28	0.7550
H	196.37	0.7068
I	197.42	0.7663
J	197.28	0.7550
K	196.83	0.7073
L	196.72	0.7090

As shown in Table 4 and Figures 10E–10H, the change in spray angle has a minimal effect on the liquid film thickness, with an average fluctuation of less than 1 μm, suggesting that the spray angle has little sensitivity to the film thickness. However, the uniformity index initially increases and then decreases as the spray angle increases. For group H, which uses a large spray angle, the uniformity index is the lowest at 0.7068, indicating that an excessively large spray angle may result in uneven droplet dispersion.

(3) The influence of orifice width on the thickness and uniformity of the liquid film

The analysis of Table 4 and Figures 10I–10L reveals that the nozzle orifice width has a relatively minor impact on the thickness of the liquid film, with the fluctuation of the mean value remaining below 1μm. This suggests that the orifice width does not significantly affect the liquid film thickness. The uniformity index achieves its highest value of 0.7663 when the inner diameter is at its minimum (Group I). Conversely, when the inner diameter is 0.8 mm (Group K), the uniformity index decreases markedly. This suggests that a smaller orifice width enhances the uniformity of the liquid film. This is attributed to the fact that a smaller orifice width produces finer droplets, resulting in a more uniform distribution.

Based on the above analysis, Table 5 is summarized as follows:

As illustrated in Table 5, when selecting operational parameters, priority should be given to the flow rate, as it has an effective impact on enhancing the droplet deposition efficiency. Simultaneously, a moderate spray angle of approximately 70 degrees should be selected to prevent a large angle, which would result in a continuous decline in uniformity. Furthermore, nozzles with smaller orifice width should be employed to optimize the uniformity index.

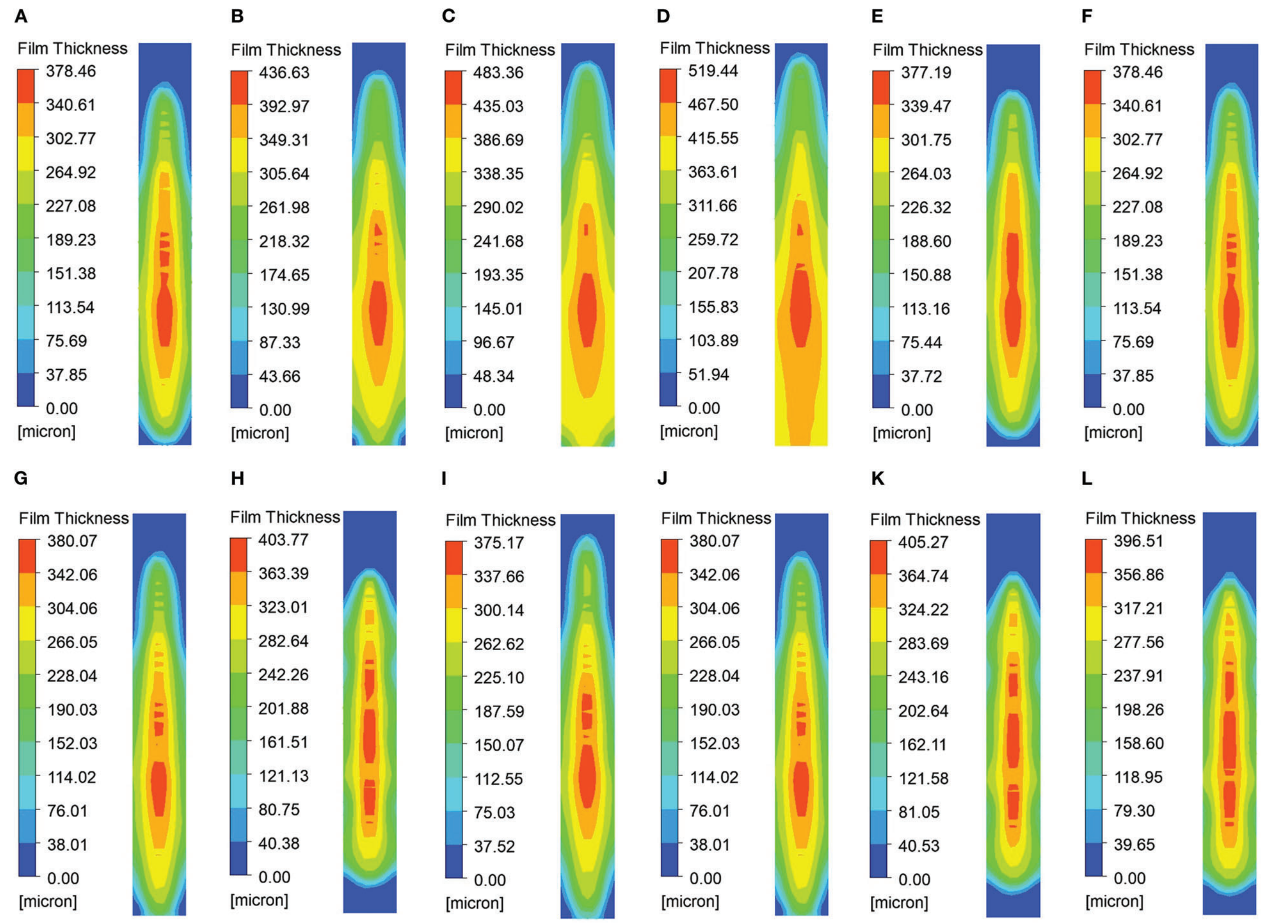

FIGURE 10
Contours of liquid film thickness for the considered cases: **(A)** 0.03,60,0.6; **(B)** 0.04,60,0.6; **(C)** 0.05,60,0.6; **(D)** 0.06,60,0.6; **(E)** 0.03,50,0.6; **(F)** 0.03,60,0.6; **(G)** 0.03,70,0.6; **(H)** 0.03,80,0.6; **(I)** 0.03,70,0.4; **(J)** 0.03,70,0.6; **(K)** 0.03,70,0.8; **(L)** 0.03,70,1.0.

TABLE 5 Comprehensive analysis and optimization suggestions.

Test factors	The influence of liquid film thickness	Influence on uniformity	Suggestion on optimization
Flow rate (0.03-0.06 kg/s)	Progressively increase	Progressively increase	The flow rate can be appropriately increased
Spray angle (50–80 deg)	Basically unchanged	First increase and then decrease	Choose a medium spray angle
Orifice width (0.4-1.0 mm)	Basically unchanged	Continuously decrease	Choose a smaller orifice width

3.2 Simulation test results and analysis of the influence of the air outlet opening degree and interval on the characteristics of multi-duct airflow field

The simulation results are summarized in Table 6, while the results for each test level are presented in Figures 11A–I. A separate analysis of groups “A, B, C”, “D, E, F”, and “G, H, I” shows that when the air outlet opening increases from 70° to 80°, the effective working height of the airflow field increases by 0.2 m. However, when the air outlet opening increases from 80° to 90°, the effective working height of the airflow field increases by 0.1 m. Separate analysis of groups “A, D, G”, “B, E, H”, and “C, F, I” shows that when the air outlet interval increases by 100mm, the effective operating height of the airflow field increases by 0.3 m. Additionally, as illustrated in Table 6, when the outlet opening degree and interval are increased, the uniformity index of the airflow velocity distribution at the domain’s end exhibits a downward trend. This occurs because as the air outlet opening and interval increase, the interaction strength at each air outlet weakens, and the areas of high-speed airflow where local interactions occur decrease. However, it is important to note that when the interval between the air outlets is 700 mm, the airflow field prevents the airflow from each air outlet from converging, which may influence the transport and deposition of the droplets.

3.3 Simulation test results and analysis of atomization characteristics of multi-duct flow field under the action of airflow field

Figures 12A–C illustrates the contours of the droplet size distribution as influenced by the airflow field at three different air velocity. Additionally, Figures 12A–C summarizes the average droplet size for each monitoring surface.

TABLE 6 Simulation results at different test levels.

Test groups	Effective working height (m)	Uniformity index
A B C	3.6 3.8 3.9	0.5955 0.5489 0.5221
D E F	3.9 4.1 4.2	0.6461 0.6013 0.5854
G H I	4.2 4.4 4.5	0.6929 0.6741 0.6693

As shown in Figures 12A–C, 13, when the liquid is ejected from the nozzle, the initial atomization occurs as a result of the interaction between jet instability (Mu et al., 2020) and the airflow field, leading to a significant reduction in droplet size. Subsequently, the smaller droplets collide and coalesce in the airflow field due to their instability, continuing until they reach approximately 1.2 meters from the air outlet. Once the droplet size reaches a certain threshold and growth ceases, although the wind speed has attenuated to some extent, it still exerts sufficient shear force to induce a second atomization, resulting in a further reduction in droplet size, which enhances droplet deposition.

As illustrated in Figure 13, the particle size of the droplets during the first atomization increases as the initial wind speed decreases, specifically at air velocity of 45 m/s, 40 m/s, and 35 m/s. This phenomenon occurs because a reduction in wind speed leads to a corresponding decrease in the shear force exerted on the droplets, thereby diminishing the degree of atomization. Furthermore, as the wind speed in the field decays with increasing lateral distance, a larger initial wind speed results in a smaller maximum critical particle size achievable through droplet merging. Additionally, as the droplets travel approximately 1.2 meters from the air outlet and undergo the second atomization, their particle size also decreases.

As demonstrated in the previous discussion, the atomization characteristics of spray droplets are notably influenced by the airflow field as they travel through the multi-channel wind environment. The findings of this study offer valuable insights for the subsequent selection of an optimal operational distance between the sprayer rows. By appropriately selecting the operational distance, an optimal droplet size can be achieved to suit the operational requirements of various orchards.

3.4 Results and analysis of droplet particle size measurement test

The results of the tests are summarized in Table 7. Analysis of Table 7 reveals that the test values of droplet particle size initially increase and then decrease as the d value increases, a trend that aligns with the simulation values shown in Figure 13. Concurrently, the average of the three measurement values in each test group was computed, and the relative error between these values and the

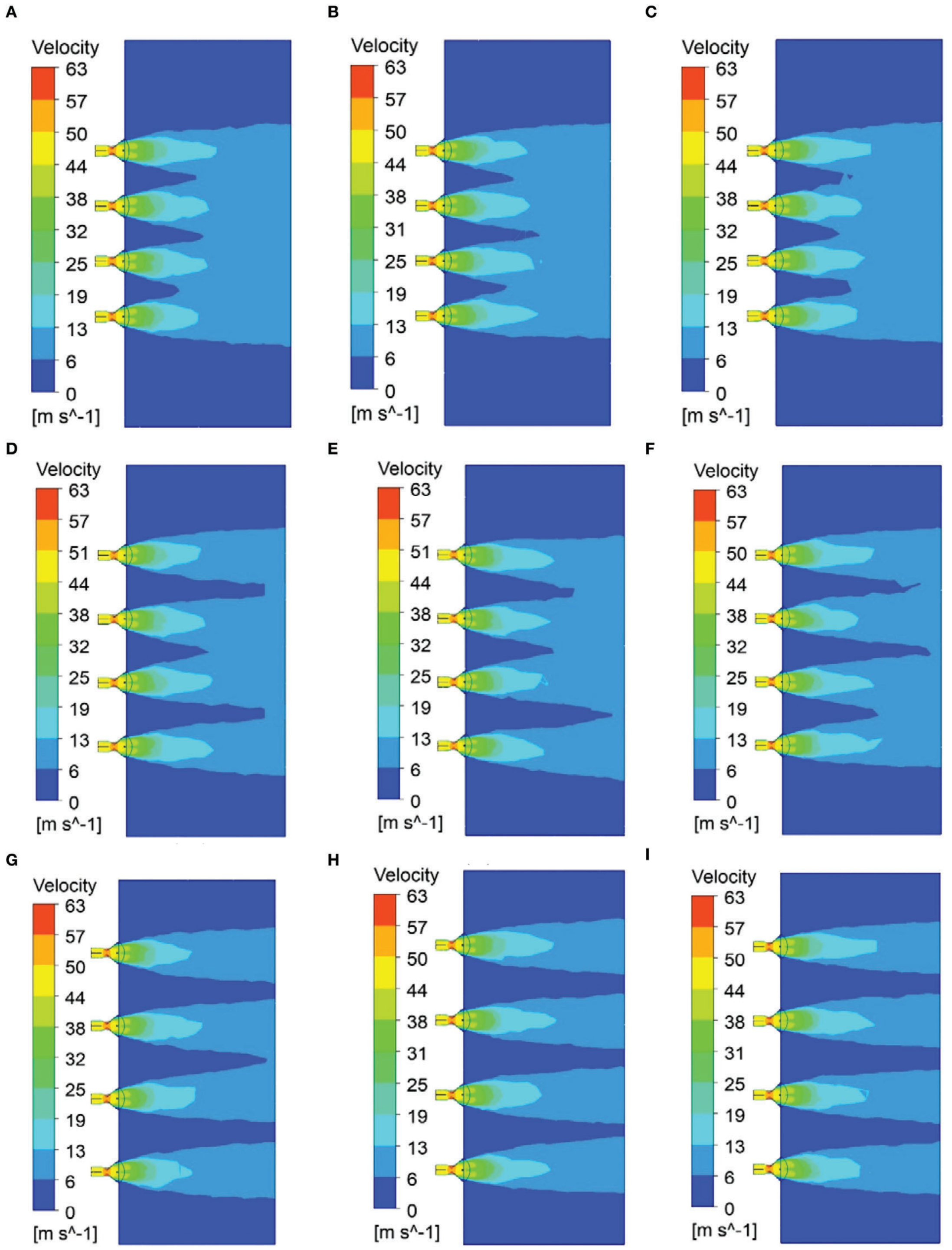

FIGURE 11
Simulation results at each test level: **(A)** 70,500; **(B)** 80,500; **(C)** 90,500; **(D)** 70,600; (E) 80,600; **(F)** 90,600; **(G)** 70,700; **(H)** 80,700; **(I)** 90,700.

simulation values was calculated. The relative errors between the test values and the simulation values across the five test groups ranged from 11.4% to 15.3%, all of which were below 16%, thereby confirming the reliability and applicability of the CFD simulation model established in this study.

4 Conclusions

The traditional prototype testing method is time-consuming and incurs high costs. Utilizing CFD method, this study developed a fluid simulation model for the multi-duct sprayer and conducted a

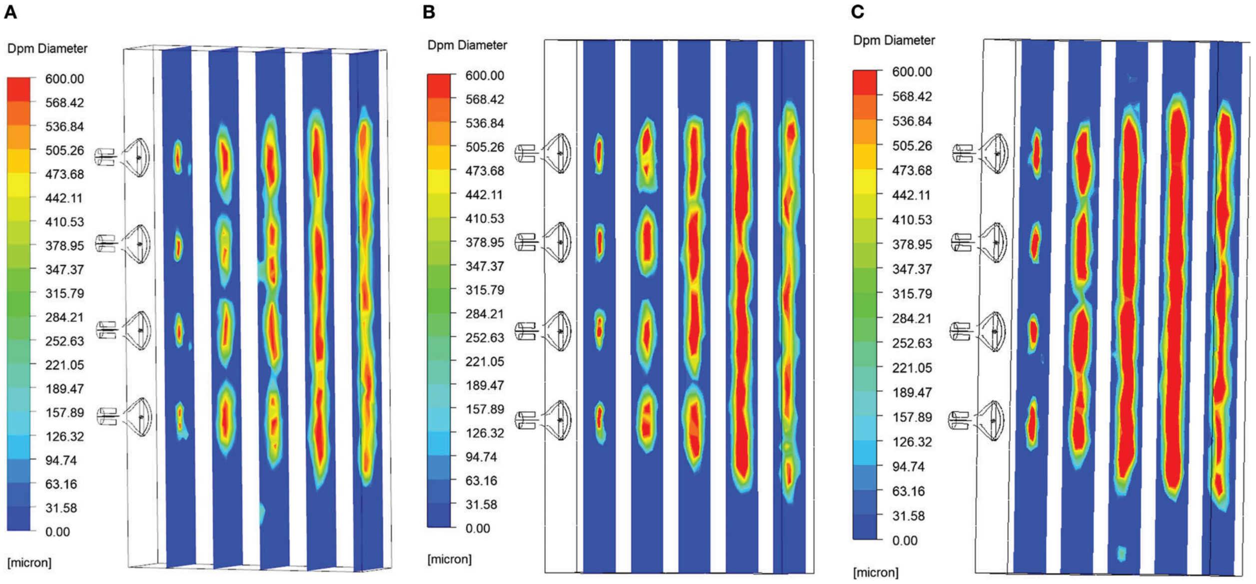

FIGURE 12
Contours of particle size distribution of droplets under the influence of airflow field for three considered values of air velocity: **(A)** air velocity 45 m/s; **(B)** air velocity 40 m/s; **(C)** air velocity 35 m/s.

series of simultaneous gas-liquid coupling simulations to investigate the effects of various factors on the multi-duct spray flow field. The primary conclusions drawn from this study are as follows:

(1) The impact of spray flow rate, spray angle, and nozzle orifice width on droplet deposition rate and its uniformity was investigated through a simulation test examining the factors influencing multi-air duct air-delivery spray operations. During the simulation experiment, the thickness of the liquid film and its distribution uniformity were assessed indirectly. The simulation results demonstrate that as the nozzle flow rate increases from 0.03 kg/s to 0.06 kg/s, the average thickness of the liquid film rises from 197.31 μm to 340.71 μm, and the uniformity index increases from 0.7521 to 0.8465. This suggests that higher flow rates effectively enhance droplet deposition and improve distribution uniformity. A medium spray angle (70°) yields the highest uniformity index for the liquid film. In contrast, an excessively large angle results in a significant reduction in uniformity. The nozzle with a smaller orifice width increases the uniformity index to 0.7663 by generating finer droplets, outperforming the nozzle with a larger orifice width. However, it is important to note that excessively small droplet sizes increase the risk of droplet drift. The influence of this operational factor provides valuable insights for the further

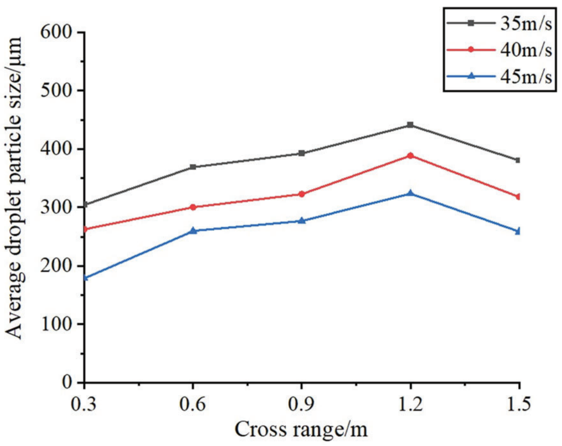

FIGURE 13
Particle size distribution curves of each detection surface for three considered values of air velocity.

TABLE 7 The results of droplet particle size measurement test.

d(m)	Measurement values of droplet particle size (μm)	Test values (μm)	The relative error compared to the simulation values
0.3	205.96 197.28 202.58	201.94	13.1%
0.6	291.12 319.16 287.35	299.21	15.3%
0.9	309.41 315.58 312.97	312.32	13.3%
1.2	362.32 355.74 363.44	360.50	11.5%
1.5	288.63 296.52 290.19	291.78	11.4%

optimization of operational parameters for the multi-duct sprayer in orchard applications.

(2) This study conducted simulation tests to investigate the effects of the opening degree and interval of the air outlets on spray operation in multi-ducts. The results revealed the impact of these factors on both the effective working height and the uniformity of the velocity distribution at the end of computational domain of the airflow field. As the outlet opening degree increases from 70° to 80°, the effective operational height of the airflow field increases by 0.2 m, and a further increase from 80° to 90° results in an additional increase of 0.1 m. Moreover, for every 100 mm increase in the outlet spacing, the effective working height of the airflow field rises by 0.3 m. Furthermore, the results also show that as both the outlet opening degree and spacing increase, the uniformity of the velocity distribution at the end of computational domain of the airflow field decreases to varying extents. These findings may serve as a reference for optimizing the profiling spray operations of multi-duct sprayers.

(3) Simulation tests were conducted to examine the atomization characteristics of droplets in the multi-channel flow field influenced by the airflow field. Upon ejection from the nozzle, the droplets undergo initial atomization. Subsequently, due to a rapid reduction in particle size, the smaller droplets continue to travel through the airflow field, where they collide and merge with larger droplets, increasing their size. Upon reaching approximately 1.2 meters from the air outlet, the droplets undergo secondary atomization due to the sheer force of the airflow field, resulting in a further reduction in droplet size, which facilitates deposition within the fruit tree canopy. This phenomenon provides valuable insights for the subsequent optimization of row spacing in orchard operations using multi-duct sprayers.

(4) The reliability of the CFD simulation model presented in this study was validated by conducting droplet particle size measurement test. When all other conditions were maintained consistent with the simulation parameters, and the initial air velocity at the air outlet was 45 m/s, the trends of the test and simulation values were similar, with the relative error ranging from 11.4% to 15.3%, which falls within an acceptable range. This confirms the reliability of the CFD simulation model presented in this study and its credibility for practical applications.

The conclusions of this study can serve as a reference for further optimization and enhancement of the operational efficiency of the multi-duct sprayer in orchards. Additionally, it can provide data support for the subsequent transformation of conventional pesticide application practices associated with this sprayer.

Data availability statement

The raw data supporting the conclusions of this article will be made available by the authors, without undue reservation.

Ethics statement

The manuscript presents research on animals that do not require ethical approval for their study.

Author contributions

JL: Conceptualization, Funding acquisition, Writing – original draft. HH: Project administration, Formal Analysis, Methodology, Writing – original draft. HF: Data curation, Validation, Writing – review & editing. YiL: Writing – review & editing, Supervision, Data curation. YuL: Data curation, Validation, Writing – review & editing. YC: Writing – review & editing, Funding acquisition, Supervision.

Funding

The author(s) declare financial support was received for the research and/or publication of this article. This research was supported by the earmarked fund for the Guangdong Laboratory for Lingnan Modern Agriculture (Grant No. NZ2021040 NT2021009), the Guangdong Province Rural Revitalization Strategy Special Project (Grant No. 2023-440000-60010000-9818), the 2022 Provincial Science and Technology Project of Agricultural High-Tech Industry Demonstration in Jinggangshan (Grant No. 20222-051256), the Special Project of Rural Vitalization Strategy of Guangdong Academy of Agricultural Sciences (Grant No. TS-1-4), the China Agriculture Research System (Grant No. CARS-32), and the Specific University Discipline Construction Project of South China Agricultural University in 2023 (Grant 2023B10564002).

Conflict of interest

The authors declare that the research was conducted in the absence of any commercial or financial relationships that could be construed as a potential conflict of interest.

Generative AI statement

The author(s) declare that no Generative AI was used in the creation of this manuscript.

Any alternative text (alt text) provided alongside figures in this article has been generated by Frontiers with the support of artificial intelligence and reasonable efforts have been made to ensure accuracy, including review by the authors wherever possible. If you identify any issues, please contact us.

Publisher's note

References

Adeniyi, A. A., Morvan, H. P., and Simmons, K. A. (2017). A coupled euler-lagrange cfd modelling of droplets-to-film. *Aeronautical J.* 121, 1897–1918. doi: 10.1017/aer.2017.107

Baetens, K., Nuyttens, D., Verboven, P., De Schampheleire, M., Nicolaï, B., and Ramon, H. (2007). Predicting drift from field spraying by means of a 3d computational fluid dynamics model. *Comput. Electron. Agric.* 56, 161–173. doi: 10.1016/j.compag.2007.01.009

Cao, S., Ou, M., and Jia, W. (2020). Data analysis of influence of flight rate of uav spray flow field. *J. Agric. Mechanization Res.* 42, 24–29. doi: 10.3969/j.issn.1003-188X.2020.07.004

Chen, S., Lan, Y., Zhou, Z., Ouyang, F., Wang, G., Huang, X., et al. (2020). Effect of droplet size parameters on droplet deposition and drift of aerial spraying by using plant protection uav. *Agronomy* 10, 195. doi: 10.3390/agronomy10020195

Chen, J., Shi, P., Wen, L., Yan, S., Cao, Z., and Jin, Y. (2015). Cfd prediction of phase change behavior and liquid film evolution on specimens based on the eulerian wall film model of two-phase flow. *Chin. J. Eng.*, 37, 721–730. doi: 10.13374/j.issn2095-9389.2015.06.007

Chen, C., Xue, X., Zhou, Q., Gu, W., Zhang, S., and Wu, C. (2023). Fixed spraying systems application in citrus orchards: nozzle type and nozzle position effects on droplet deposition and pest control. *Agronomy* 13, 2828. doi: 10.3390/agronomy13112828

Dekeyser, D., Duga, A. T., Verboven, P., Endalew, A. M., Hendrickx, N., and Nuyttens, D. (2013). Assessment of orchard sprayers using laboratory experiments and computational fluid dynamics modelling. *Biosyst. Eng.* 114, 157–169. doi: 10.1016/j.biosystemseng.2012.11.013

Delele, M. A., Jaeken, P., Debaer, C., Baetens, K., Endalew, A. M., Ramon, H., et al. (2007). Cfd prototyping of an air-assisted orchard sprayer aimed at drift reduction. *Comput. Electron. Agric.* 55, 16–27. doi: 10.1016/j.compag.2006.11.002

Duga, A. T., Delele, M. A., Ruysen, K., Dekeyser, D., Nuyttens, D., Bylemans, D., et al. (2017). Development and validation of a 3d cfd model of drift and its application to air-assisted orchard sprayers. *Biosyst. Eng.* 154, 62–75. doi: 10.1016/j.biosystemseng.2016.10.010

Endalew, A. M., Debaer, C., Rutten, N., Vercammen, J., Delele, M. A., Ramon, H., et al. (2010). A new integrated cfd modelling approach towards air-assisted orchard spraying. Part i. Model development and effect of wind speed and direction on sprayer airflow. *Comput. Electron. Agric.* 71, 128–136. doi: 10.1016/j.compag.2009.11.005

García-Ramos, F., Malón, H., Aguirre, A., Boné, A., Puyuelo, J., and Vidal, M. (2015). Validation of a cfd model by using 3d sonic anemometers to analyse the air velocity generated by an air-assisted sprayer equipped with two axial fans. *Sensors* 15, 2399–2418. doi: 10.3390/s150202399

Gu, J., Zhu, H., Ding, W., and Wang, X. (2014). Characterization of air profiles impeded by plant canopies for a variable-rate air-assisted sprayer. *Trans. Asabe* 57, 1307–1315. doi: 10.13031/trans.57.10646

Hong, S., Zhao, L., and Zhu, H. (2018). Cfd simulation of airflow inside tree canopies discharged from air-assisted sprayers. *Comput. Electron. Agric.* 149, 121–132. doi: 10.1016/j.compag.2017.07.011

Huang, X., Li, Y., Chen, L., and Wang, K. (2025). CFD-based flow field characteristics of air-assisted sprayer in citrus orchards. *Agriculture* 15, 1103. doi: 10.3390/agriculture15101103

Jiang, H., Niu, C., Liu, L., Wang, D., Wang, J., and Mao, W. (2020). Design and experiment of air volume control system of orchard multi-pipe air sprayer. *Trans. Chin. Soc. Agric. Machinery* 51, 298–307. doi: 10.6041/j.issn.1000-1298.2020.S2.035

Jiang, X., Wang, S., Chen, J., Ji, J., Zhu, C., and Zhu, X. (2022). Analysis of influencing factors on atomization characteristics of fan-shaped nozzle. *J. Drainage Irrigation Machinery Eng.* 40, 1065–1071. doi: 10.3969/j.issn.1674-8530.21.0065

Lee, I., Bitog, J. P. P., Hong, S., Seo, I., Kwon, K., Bartzanas, T., et al. (2013). The past, present and future of cfd for agro-environmental applications. *Comput. Electron. Agric.* 93, 168–183. doi: 10.1016/j.compag.2012.09.006

Li, J., Bian, Y., Huo, P., Wang, P., Xue, C., and Yang, X. (2021). Design and experimental optimization of spray device for air-fed annular nozzle of sprayer. *Trans. Chin. Soc. Agric. Machinery* 52, 79–88. doi: 10.6041/j.issn.1000-1298.2021.09.009

Li, Z., Wang, X., Li, C., Lan, H., He, Y., and Tang, Z. (2023). Performance analysis and testing of a multi-duct orchard sprayer. *Agronomy* 13, 1815. doi: 10.3390/agronomy13071815

Ma, C., Li, G., and Peng, Q. (2021). Design and test of a jet remote control spraying machine for orchards. *Agriengineering* 3, 797–814. doi: 10.3390/agriengineering3040050

Marek, M. (2013). The double-mass model of drop deformation and secondary breakup. *Appl. Math. Model.* 37, 7919–7939. doi: 10.1016/j.apm.2013.03.025

Mu, K., Li, G., and Si, T. (2020). Instability and interface coupling of coaxial liquid jets in a driving stream. *Phys. Fluids* 32, 92107. doi: 10.1063/5.0018279

Sun, G., Wang, X., Ding, W., and Zhang, Y. (2012). Simulation analysis on characteristics of droplet deposition base on CFD discrete phase model. *Trans. Chin. Soc. Agric. Machinery* 28, 13–19. doi: 10.3969/j.issn.1002-6819.2012.06.003

Wei, Z., Li, R., Xue, X., Sun, Y., Zhang, S., Li, Q., et al. (2023). Research status, methods and prospects of air-assisted spray technology. *Agronomy* 13, 1407. doi: 10.3390/agronomy13051407

Xue, X., Zeng, K., Li, N., Luo, Q., Ji, Y., Li, Z., et al. (2023). Parameters optimization and performance evaluation model of air-assisted electrostatic sprayer for citrus orchards. *Agriculture-Basel* 13, 1498. doi: 10.3390/agriculture13081498

Yang, X., Liu, Y., Wang, J., Chen, C., and Lyu, L. (2024). Flow field simulation and test of air delivery system for orchard multi-duct sprayer. *J. Jilin University(Engineering Technol. Edition)* 54, 2723–2732. doi: 10.13229/j.cnki.jdxbgxb.20221431

Zhai, C., Zhang, Y., Dou, H., Wang, X., and Chen, L. (2021). Cfd modeling and experiment of airflow at the air outlet of orchard air-assisted sprayer. *Smart Agric.* 3, 70–81. doi: 10.12133/j.smartag.2021.3.3.202106-SA007

Zhang, X., Wen, Z., Wang, Q., Li, H., Zhang, Z., Liu, J., et al. (2022). Research on characteristics of airway pressure loss in seeding-wheel-type pneumatic seeder. *Agriculture-Basel* 12, 2021. doi: 10.3390/agriculture12122021

四、科研成果

证书号第8513966号

专利公告信息

发明专利证书

发明名称：具有准零刚度特性的三自由度并联隔振平台

专利权人：华南农业大学

地址：510642 广东省广州市天河区五山路483号

发明人：曹亚超;江惠芳;何政龙;冯隽堂;陈梅;陈广川

专利号：ZL 2024 1 1712931.4　　授权公告号：CN 119467602 B

专利申请日：2024年11月27日　　授权公告日：2025年11月25日

申请日时申请人：华南农业大学

申请日时发明人：曹亚超;江惠芳;何政龙;冯隽堂;陈梅;陈广川

国家知识产权局依照中华人民共和国专利法进行审查，决定授予专利权，并予以公告。

专利权自授权公告之日起生效。专利权有效性及专利权人变更等法律信息以专利登记簿记载为准。

局长

申长雨

申长雨

2025年11月25日

证书号第8512651号

专利公告信息

发明专利证书

发 明 名 称：具有三维零刚度特性的并联隔振平台

专 利 权 人：华南农业大学

地　　　址：510642 广东省广州市天河区五山路483号

发　明　人：曹亚超;何政龙;江惠芳;冯隽堂;陈梅;陈广川

专　利　号：ZL 2024 1 1713714.7　　　授权公告号：CN 119532382 B

专利申请日：2024年11月27日　　　授权公告日：2025年11月25日

申请日时申请人：华南农业大学

申请日时发明人：曹亚超;何政龙;江惠芳;冯隽堂;陈梅;陈广川

国家知识产权局依照中华人民共和国专利法进行审查，决定授予专利权，并予以公告。

专利权自授权公告之日起生效。专利权有效性及专利权人变更等法律信息以专利登记簿记载为准。

局长
申长雨

申长雨

2025年11月25日

五、其他业绩

华南农业大学2023年度大学生创新创业训练计划立项项目一览表

编号	所属学院	项目编号	项目名称	项目类型	项目级别	项目负责人		项目其它成员	指导教师	
						姓名	学号		姓名	所属学院
128	工程学院	S202310564030	拖拉机自动泊车系统	创新训练项目	省级	孙培泽		谢绍安(202121510125)、刘均浩(202234410313)、甘文灵(202234210203)、苏睿(202221310119)	张智刚	工程学院
129	工程学院	2023105641048	丘陵山地甘蔗小型联合收获机器人的设计研发	创新训练项目	校级	温锴源		严子臻(202133110122)、陈梅(202221510404)、刘铭俊(202221510116)	徐凤英	工程学院
130	工程学院	2023105641198	全自动荔枝采摘机	创新训练项目	校级	谭深文		谢润涛(202225810123)、廖泽虹(202121510215)、吴咏霖(202125910218)	郭嘉明	工程学院
131	工程学院	2023105641123	基于GaN器件的农用无人机配电系统轻量化研究	创新训练项目	校级	郑锦标		陈鑫畅(202119110702)、梁本锌(202121310415)、周其骏(202134610329)、丘焕珂(202234310215)	胡仁俊	工程学院
132	工程学院	2023105641049	智能多场景垃圾清理机	创新训练项目	校级	林子新		刘世聪(202121510117)、潘伟兴(202121510119)、刘国楠(202121510114)、邓竣文(202219110505)	卿艳梅	工程学院
133	工程学院	2023105641137	基于多传感器信息融合的菠萝采摘器测控系统设计	创新训练项目	校级	潘雄		邓柏裕(202119210105)、陈昊贤(202113110301)、黄圳煜(202221810108)、赵怡帆(202026710127)	陈瑜、马瑞峻	工程学院、工程学院
134	工程学院	2023105641079	自主导航避障的果园智能除草机	创新训练项目	校级	梁焯轩		伍剑洪(202121810227)、梁景辉(202221510414)、周玮隽(202221510429)、陈广川(202221510402)	曹亚超	工程学院
135	工程学院	2023105641095	苹果振动收获果实分离模拟装置设计	创新训练项目	校级	王耿林		康泽凡(202121210205)、刘梓锋(202019110815)、杨徐军(202225910127)	付函	工程学院
136	工程学院	2023105641218	广东省特种野生珍稀动物无人机大范围追踪与快速定位技术	创新训练项目	校级	曾昊喆		崔杰朗(202134510303)、吴泓佳(202121110120)、郭嘉城(202221110103)、乔振(202221120113)、卢俊宇(202228110112)	李继宇、陆永超	工程学院、党委学生工作部（学生工作处）
137	工程学院	2023105641190	草莓裸根苗移栽机构的设计与应用研究	创新训练项目	校级	肖源邦		刘函丁(202121510115)、周晓伟(202121510130)、沈飞扬(202214120118)	黄培奎、羊海军	工程学院、基础实验与实践训练中心
138	工程学院	2023105641217	云梦一家——基于homeassistant的定制化和自动化智能家居系统	创新训练项目	校级	罗佳龙		张洪鸣(202221210128)、王锴霖(202221510120)、林佳楠(202221210214)	莫嘉嗣	工程学院
139	工程学院	2023105641107	基于气动发射的多模式智能发球机	创新训练项目	校级	赖展鹏		黄桂洋(202021510610)、郑彦丞(202234310330)、曾祥豪(202221110126)	张永博	工程学院
140	工程学院	2023105641004	基于PLC的自动树木落叶化肥机设计	创新训练项目	校级	徐壬涛		郑贤泉(202021710329)、卢广栋(202021710318)、黄乃金(202221810208)、刘梓阳(202221810121)	杨秀丽、邢航	工程学院、工程学院
141	工程学院	2023105641210	基于智能安防巡检AGV的四舵轮独立悬挂底盘的设计研究	创新训练项目	校级	贡安聚		耿永谦(202234410105)、黄品沛(202125220709)、钟雍泰(202221210229)	胡仁俊	工程学院
142	工程学院	2023105641201	道地药材巴戟天去木心设计	创新训练项目	校级	廖芷柔		罗嘉炜(202121310112)、宁浩(202121310113)、黄尧嘉(202021510406)、陈永模(202221510204)、杨力红(202021510424)	孙振刚	工程学院
143	工程学院	2023105641206	基于SLAM的柑橘果园植保无人机集群系统	创新训练项目	校级	刘锦晖		李梓平(202021510517)、丘博研(202221110115)、张浩楠(202034410227)	漆海霞	工程学院
144	工程学院	2023105641041	基于车辆运动状态识别的车手信息辅助装置	创新训练项目	校级	张珺玮		林俊杰(202021210414)、区圣儒(202021210417)、韦富天(202121210117)、林玟(202121210409)	郭嘉明	工程学院
145	工程学院	2023105641151	基于ACP的FSAE大学生方程式赛车翼片的轻量化设计	创新训练项目	校级	黄相茗		温石境(202221210121)、林勋(202121210210)、陈嘉鑫(202221210101)	李庆	工程学院
146	工程学院	2023105641187	智能安保头盔	创新训练项目	校级	林宏宇		何昊燊(202221310406)、翁永霖(202121210421)、林怀茵(202234310210)、陈家雄(202234310403)	毛彩云	工程学院
147	公共管理学院	202310564088X	乡去户外——打造"户外+"乡村振兴新商业模式，实现互惠共赢	创业训练项目	国家级	何亮		谢蕙妃(202023120324)、陈锦霞(202223220204)、胡杰(202025220212)、温俊仁(202121410222)、张瀚(201816060229)	朱汉平	公共管理学院
148	公共管理学院	202310564022	"需求导向"下数字赋能社区-居家养老——以广东省智慧养老社区为例	创新训练项目	国家级	梁启熙		杨恺文(202222410123)、曾昆慧(202226410326)、王润涛(202223510125)、叶俊枫(202126410327)、陈虹萤(202226410302)	李颖奕、张沁洁	公共管理学院、公共管理学院
149	公共管理学院	202310564021	韧性小农：演进韧性视角下农户灾害风险管理机制研究	创新训练项目	国家级	李曼莹		潘晓璠(202126910818)、潘惠琳(202026911011)、乔楚然(202026911422)、高楚芸(202226910104)	方敏	公共管理学院
150	公共管理学院	202310564020	农村残障儿童康复现状及需求调研	创新训练项目	国家级	朱碧瑶		张艺垚(202126410124)、赵宁(202126410125)、蔡文悦(202126410102)、关淇文(202226410104)、欧阳慧霖(202226410417)	马林芳	公共管理学院
151	公共管理学院	202310564019	新发展格局下地方财政收入质量的影响因素与政策优化研究——基于稳健性和均衡性双维度视角	创新训练项目	国家级	陈凯文		何幸琳(202126911111)、林丽扬(202126911013)、李好(202026910312)、赵伟诚(202229110123)	史传林、周毅	公共管理学院、公共管理学院
152	公共管理学院	202310564018	资本存量、抗逆力对农村青少年的网络风险的影响机制与干预研究	创新训练项目	国家级	罗嘉乐		宁选琳(202226410219)、潘楚敏(202226410220)、黄晶晶(202226410308)、廖梓莹(202026410209)	林诚彦、卓彩琴	公共管理学院、公共管理学院
153	公共管理学院	S202310564048	"互联网＋"赋能社区老人积极老化策略研究	创新训练项目	省级	张露诗		张秦碧(202126410123)、郭泳彤(202123120206)、林骄阳(202226911217)、蔡砚希(202226410202)	李颖奕	公共管理学院

类别	项目名称	团队成员姓名	指导老师	获奖情况
A5	在荔枝果园下基于三角网格地图的三维导航机器人	张鑫德，李佳祥，陈静宁，尹学明，朱晨	程碧懿	一等奖
A5	面向复杂地形的全自动智能烟草采收装备	陈弘凯，张健帆，林斯铄，陈雪欣，张涛	李杰浩	一等奖
A2	小粒 / 异形蔬菜育苗播种生产线的智能补种装置	黄凯文，纪浩楠，陈土佳，钟广泽	陈学深	一等奖
D 类	新型横列式多旋翼多机组合体植保无人机	叶健言，张铭乐、徐壬涛、卢广栋、卞锦泉	申遂愿，李继宇	一等奖
A8	智能茶青分级装置	陈迅，乔佳航，戴浩然，吴定河，孟晶蕊	郭嘉明	二等奖
A5	优茶智采 — 基于混联机械臂的茶芽精准识别与优径采摘	李浩欣，高炳业，崔坤，韦超传，郑镇杰	吴伟斌，罗远强	二等奖
A7	基于光谱传感与边缘智能的水质检测仪	余意，郑欣，梁海雯，黄君盈	熊俊涛	二等奖
A8	奶爸卫士 —— 哺乳期母仔一体化智能养殖系统	邓强宗，肖锋华，刘穗鸿，莫美雪，彭梓冰	曾志雄，吕恩利	二等奖
A8	鸽笼自主式换料机器人	柳嘉桐，李佳宝，张荣斌，廖一飞，杨振邦	张烨	二等奖
A5	椒韵 —— 中国辣椒采摘开拓者	罗康雅，梁晓瑜，蔡佳芸，包宇翔，黄铭轩	张亚莉	二等奖
A5	基于触觉感知和柔性变径刀具的自动化香蕉落梳机	屈明宇、黄佳涛，朱思杰，钟尚志，夏展飞	金莫辉	三等奖
D 类	基于多参数传感器阵列的智能水产精准投喂系统	程美娟，胡琳，林宇健，陈长鑫，杨斯烨	曾志雄	二等奖
A8	无人农机多传感器融合作业环境感算一体系统	管宪鲁，郑依桐、王欣瑞，包宇翔，官滢媛	周志艳，姜锐	三等奖
A3	基于尖端放电技术的多旋翼植保无人机智能静电喷雾系统	卢洁莹，朱德军，邱子钊，吴小钰，陈毅泓	贾瑞昌	三等奖
A3	水田环境下基于 Fields2cover 库的双螺旋驱动式机器人路径规划系统	莫健钊，吴昱汛，宁锦泰，吴塔铿，詹仕成	徐志豪	三等奖
A5	柔性多杆连续体并联机构荔枝振动采收设备	潘锦涛，梁誉，陈颖聪，陈新宏，郭庆宇	曹亚超	三等奖
A7	基于智能传感器的植保无人机	卢奕铭，陈佳洲，林峻锋，潘载轩，张舒宝	李继宇，申遂愿	三等奖
A5	荔枝串果振动采收装置	陈新宏，郭庆宇，潘锦涛，梁誉，陈颖聪	王慰祖	三等奖
A7	多源融合感知的丘陵果园农业机器人三维自主导航系统	黄于轩，王幸懿，梁晓瑜，陈炜佳，吴俊贤	汪博文，梅宏玉，邱亚龙	三等奖
A2	基于无人机的高陡边坡复绿装置的研究	蔡国奥，黄立煊	臧英	三等奖
A5	基于升降台系统的六轴机械臂樱桃番茄串收系统	李雅萱，谢浩海，郑依桐，吴凤鸣，李佳培	杨丹彤	三等奖
A3	果园智能植保新方案：自主导航与精准对靶喷雾机器人	吴潇，刘杰，殷珍，陈顺良，梁健豪	张智刚	三等奖
A3	果园智能除草机器人	黄庆荣，林岳欣，彭国康，黄文毫，朱劲炜	张闻宇	三等奖

获奖证书

CERTIFICATE OF AWARD

“海格电气杯”第十一届国际大学生智能农业装备大赛校内选拔赛中，荣获

三等奖

特发此证，以资鼓励。

获奖学生：潘锦涛　梁誉　陈颖聪　陈新宏　郭庆宇

项目名称：柔性多杆连续体并联机构荔枝振动采收设备

华南农业大学工程学院

二零二五年十一月

华南农业大学2024年大学生创新训练计划项目信息表

编号	所属学院	项目编号	项目名称	项目类型	项目级别	项目负责人（第一主持人）		项目其它成员	指导教师			
						姓名	学号		姓名	工号	职称	所属学院
111	动物科学学院	2024105641049	山羊肠道高产酸乳酸菌的分离培养与鉴定	创新训练项目	校级	谢钰顾	202219110227	杨思莹(202219130122)，奉之韵(202319110205)，符航宁(202119110506)，李云骐(202119110211)	孙宝丽	[redacted]	教授	动物科学学院
112	动物科学学院	2024105641060	母仔猪一体化：母猪肠道乳酸杆菌对于母猪泌乳和仔猪健康的深入探索	创新训练项目	校级	吕庆功	[redacted]	李楷峰(202119110709)，孙铭微(202119110715)，林淑君(202319110310)	张世海	[redacted]	副教授	动物科学学院
113	动物科学学院	2024105641070	饲粮添加不同锌源对生长后期肉鸭皮肤质量的影响	创新训练项目	校级	张振一	[redacted]	朱小龙(202119110729)，范德誉(202319120104)，黎展锋(202319120112)	朱勇文，杨殷一	[redacted]	副教授，助教	动物科学学院，动物科学学院
114	动物科学学院	2024105641084	清远麻鸡特征风味代谢物的鉴定及其遗传机制研究	创新训练项目	校级	张瑞彤	[redacted]	刘雨希(202319110414)，叶雨轩(202319110425)，黄子柔(202319110408)，王昕怡(202319110419)，王欣怡(202319110418)	蔡柏林	[redacted]	助理研究员（自然）	动物科学学院
115	动物科学学院	2024105641088	Hsp70响应温度调控家蚕抗菌肽表达的分子机制	创新训练项目	校级	李易庆格	[redacted]	谭莹(202223910627)，周思含(202219110233)，黄雪瑶(202239010215)，柯德浩(202323320108)	杨婉莹	[redacted]	教授	动物科学学院
116	动物科学学院	2024105641105	乳酸菌胞外多糖提取、纯化和调控乳房炎的效果研究	创新训练项目	校级	袁呈玥	[redacted]	尹佳佳(202219110333)，梁冉婷(202219110315)，赖怡涛(202219110310)，李雅丽(202319310111)	柳广斌	[redacted]	讲师	动物科学学院
117	动物科学学院	2024105641117	迷走神经TGR5受体在热应激导致猪厌食中的作用及微生物-肠-脑轴机制	创新训练项目	校级	张焓墨	[redacted]	姚佳宁(202219110131)，莫锦龙(202219110114)，陶开旋(202219110118)，陈钟慰(202219110103)，郑直(202319110327)	朱灿俊	[redacted]	副教授	动物科学学院
118	动物科学学院	2024105641128	灵陈菌质下调黄羽肉鸡中TVB-N的代谢机制研究	创新训练项目	校级	钱爱玲	[redacted]	邓诗睿(202222110205)，郭孟泽(202219120107)，岳鋆铭(202319110226)	左建军	[redacted]	教授	动物科学学院
119	工程学院	202410564007	汽车避震器振动能量回收装置	创新训练项目	国家级	徐森斯	[redacted]	温畅(202316110216)，许松选(202121310323)，廖敏涵(202318710110)	孙振刚，孔莲芳	[redacted]	副教授，讲师	工程学院，工程学院
120	工程学院	202410564026	一种基于移振两用Delta机构的荔枝振动采收平台	创新训练项目	国家级	陈家弘	[redacted]	陈奕铮(202221310304)，劳乐雅(202221510213)，彭常识(202334310417)，刘伟杰(202225310318)，陈诗景(202234210103)	王慰祖，曹亚超	[redacted]	副教授，讲师	工程学院，工程学院
121	工程学院	202410564045	基于ROS的田间智能辣椒采摘机	创新训练项目	国家级	高源	[redacted]	周桢宝(202221510430)，夏锐(202221110119)，杨轩(202321110127)，姜昊文(202321110108)，李佳宝(202321110109)	张亚莉，王红军	[redacted]	副教授，教授	工程学院，工程学院
122	工程学院	202410564067	“纤”载奇遇——开拓NiFeAl-LDH插层纤维素复合载氧体的CL-SMR应用	创新训练项目	国家级	麦浩婷	[redacted]	胡钦腾(202233410207)，陈健(202233410201)，陈业开(202133410203)，陈一夫(202133410204)，朱远虎(202333410131)	胡志锋	[redacted]	副教授	工程学院
123	工程学院	202410564074	基于机器学习的油茶果振动采收激励参数优化研究	创新训练项目	国家级	杨薇仙	[redacted]	伍家东(202221510323)，钟哲宇(202221310129)，徐嘉怡(202325910224)	付函	[redacted]	副教授	工程学院
124	工程学院	202410564078	芒果挂果及其成熟度智能识别与自动无损采摘系统设计	创新训练项目	国家级	涂镇	[redacted]	杨健(202229220225)，刘泽为(202321120114)，林祥烨(202221810119)	卢家欢，李杰浩	[redacted]	，	工程学院，工程学院
125	工程学院	S202410564017	呼吸有道——可穿戴式牛呼吸监测装备	创新训练项目	省级	梁信玮	[redacted]	郑建胜(202221120128)，伍津乐(202321140122)，张淡然(202321510226)，熊敏饴(202321210325)	李继宇，吕佳	[redacted]	教授，讲师	工程学院，工程学院
126	工程学院	S202410564069	基于电动汽车三电系统的能量回收控制策略	创新训练项目	省级	谭燕	[redacted]	谢赋明(202321210324)，王一格(202333510119)，黄曦(202321210310)，陈志机(202121140107)，胡永佳(202121310208)	孙振刚	[redacted]	副教授	工程学院
127	工程学院	S202410564082	基于高熵载氧体的生物质化学链原位甲烷化反应机制研究	创新训练项目	省级	曾雯慧	[redacted]	彭湘琳(202333410218)，庞咏欣(202233410115)，胡强(202216110313)	孙焱	[redacted]	助理研究员（自然）	工程学院
128	工程学院	S202410564097	基于地-空光谱技术的茶叶估产研究	创新训练项目	省级	李子豪	[redacted]	谢俊杰(202321140123)，谢铖涛(202321210220)，吴贤楠(202121210323)，卢新霞(202321510412)	吴伟斌，罗霞	[redacted]	教授，高级实验师	工程学院，电子工程学院（人工智能学院）
129	工程学院	S202410564111	淬火-燃烧法促进Ni-CaO双功能材料高效CO2捕获与原位甲烷干重整	创新训练项目	省级	陈倚云	[redacted]	庄静文(202133410233)，唐瞻甜(202333410220)，聂葭琦(202333410217)	胡志锋	[redacted]	副教授	工程学院
130	工程学院	S202410564122	基于机器视觉与深度学习的草莓自动采摘机器人	创新训练项目	省级	林泽宏	[redacted]	何泽基(202221810105)，黄龙生(202221810106)，莫艺峰(202321810220)	周锡恩，陈瑜	[redacted]	实验师，讲师	工程学院，工程学院
131	工程学院	S202410564138	面向非结构环境视觉伺服的名优茶芽叶精确采摘系统	创新训练项目	省级	钱喆	[redacted]	杜炯璇(202321140103)，黄庆蕾(202121120109)，梁志祥(202221810215)，杨清盈(202121120126)，胡英铨(202221510308)	马锐军，胡仁俊	[redacted]	实验师，讲师	工程学院，工程学院
132	工程学院	S202410564142	基于FSEC的整车数据采集系统的设计	创新训练项目	省级	唐磊	[redacted]	林志森(202321210312)，罗康雅(202321510116)，陈均华(202321210303)，张秋玲(202221310427)	李庆	[redacted]	副教授	工程学院
133	工程学院	S202410564149	基于能量内循环的粮食闭式热泵干燥系统设计	创新训练项目	省级	陈雄坤	[redacted]	薛明治(202221120122)，陈俊泽(202321110103)，郭子洋(202121120105)，温鑫(202314510223)，刘雪华(202321110114)	张烨	[redacted]	高级工程师	工程学院
134	工程学院	S202410564157	微型作物表型监测机器人研究	创新训练项目	省级	林鹏	[redacted]	陈淑微(202221310205)，何浩文(202321210306)，张嘉威(202321210227)	杨文武	[redacted]	高级实验师	工程学院
135	工程学院	S202410564159	基于迁移学习融合长短期记忆网络的粮食深床干燥瞬态信息感知系统设计	创新训练项目	省级	李韵怡	[redacted]	黄建朝(202121120107)，李悦(202321110110)，项鹏程(202221120120)，柳嘉桐(202321110113)，苏健彬(202321110118)	李成杰，张烨	[redacted]	，高级工程师	工程学院，工程学院
136	工程学院	S202410564163	基于双供体低共熔溶剂协同鲁米诺接枝预处理实现玉米秸秆全组分利用	创新训练项目	省级	陈琳	202333410201	郑佳雯(202333410229)，谭子峰(202233410120)，王若凡(202233410121)，孟玉芳(202133410217)	孙焱	[redacted]	助理研究员（自然）	工程学院

中国大学生机械工程
创 新 创 意 大 赛

2025年中国大学生机械工程创新创意大赛
机械产品数字化设计赛（区域赛）

三等奖

作品名称：环索医生——智能桥梁拉索检修机器人

参赛组别：本科生　　参赛学生：杜文榜　伍家东　朱　晨

参赛学校：华南农业大学　　指导教师：王红军　曹亚超

中国大学生机械工程创新创意大赛
机械产品数字化设计赛执委会

武汉理工大学
机电工程学院

2025 年 7 月 15 日

证书编号：MEICC14PIC2025-ZN-SJQB3-102

获 奖 证 书

证书编号
FETIC2024030110

参赛学校：华南农业大学

参赛作品：大白菜种植收获一体机

指导老师：王红军 曹亚超

参赛学生：张锦辉 周晓伟 文言辞 刘自成 许峻威

在2024年第十一届全国大学生机械创新设计大赛慧鱼组竞赛暨慧鱼工程技术创新大赛中荣获

二等奖

特发此证，以资鼓励！

主办单位：
全国大学生机械创新设计大赛组委会

承办单位：
北京中教仪人工智能科技有限公司
杭州电子科技大学

荣誉证书

曹亚超 同志：

被评为华南农业大学工程学院“优秀共产党员”，特发此证，以资鼓励。

中共华南农业大学工程学院委员会
二〇二五年六月